Protein and VLP Adsorption on Perfusion Chromatography Media and Monoliths

A Dissertation

Presented to

the faculty of the School of Engineering and Applied Science

University of Virginia

in partial fulfillment

of the requirements for the degree

Doctor of Philosophy

by

Yige Wu

December

2014

APPROVAL SHEET

The dissertation

is submitted in partial fulfillment of the requirements

for the degree of

Doctor of Philosophy

AUTHOR

The dissertation has been read and approved by the examining committee:

Giorgio Carta

Advisor

Kyle Lampe

Geoffrey Geise

Michael King

Ammasi Periasamy

Accepted for the School of Engineering and Applied Science:

Dean, School of Engineering and Applied Science

December

2014

Print Form

Abstract

This work studies the adsorptive and chromatographic behavior of proteins and human papillomavirus (HPV) virus-like particles (VLPs) on perfusion chromatography media and tube monolith column. The perfusion resins have a bimodal distribution of pore sizes including large through-pores and smaller diffusive pores. The effect of perfusion under non-binding conditions was obtained from HETP measurements for various proteins and VLPs and the results show that the dominant mechanism of intraparticle mass transfer gradually shifts from diffusion to perfusion as the reduced velocity increases. For strong binding conditions, confocal laser scanning microscopy (CLSM) images show that the intraparticle concentration profiles at higher reduced velocity become skewed in the direction of flow, deviating from the symmetrical profiles that are characteristic of diffusional transport. The perfusive enhancement intraparticle mass transfer can be predicted based on the structural properties of the resin particles using a perfusion model. In the case of VLPs, however, the advantage of perfusion under strong binding conditions vanishes as, in this case, the adsorption is restricted to a thin layer on the adsorbent particle surface with little penetration, which is due to the blockage of the pores by bound VLPs.

The effects of particle size on the separation performance of perfusion media is examined by comparing the adsorption behavior of proteins and VLPs on differently sized particles with similar internal structure. For a smaller particle, the fraction of intraparticle flow rate increases and the shift of diffusion to perfusion occurs at lower reduced velocity.

Monoliths are also studied as another type of convective stationary phase. The internal structure of the monoliths studied comprises large flow channels where convective transport takes place. For both non-binding and strong binding conditions, the effects of flow rate on performance are negligible. However, due to the smaller binding surface area when compared with perfusion particles, the monoliths studied showed lower binding capacities. The load-wash-elute of VLPs experiments on monoliths column show low VLP recovery in the elution step, with a strong dependence on the flow directions indicating that physical trapping of VLPs may have occurred on a dense "skin" layer observed by scanning electron microscopy on the side wall of the monolith.

Acknowledgements

I would like to express my deepest gratitude to my advisor, Dr. Giorgio Carta, for his guidance, patience and support during the past several years. I would never be able to prepare myself with strong background and experiences for my future career without your encouragement and instruction.

I would also like to thank my advisory committee members: Dr. Kyle Lampe, Dr. Geoffrey Geise, Dr. Michael King and Dr. Ammasi Periasamy for their valuable inputs and inspiring discussions.

I would also like to thank Dr. Dicky Abraham from Merck & Co., for providing the financial support for my research and industrial insights relevant to this study.

I would like to thank all the current and previous members of Carta lab, especially Yinying, Nianyun, Ernie, Tarl, Mimi, Shaojie, Arch, Jason and Jing, for their help and companion. It was a great pleasure to work with you all and you made my graduate life so much fun.

I also appreciate the help from Vickie, Teresa and Ricky, for every detail including scheduling, purchasing and building experimental apparatus.

Finally I would like to thank my family and friends for their continuous love and support. To my parents, thank you for always encouraging and trusting me. To Xiaozhi, thank you for always being there all these years through my good times and bad. To Bruce, thank you for making my last several months in UVa such exciting and unforgettable.

Table of Contents

List of Figures

List of Tables

Chapter 1
Motivation and Background

1.1 Motivations

Human papillomaviruses (HPVs) are small, non-enveloped icosahedral DNA viruses associated with a wide range of infections in humans, including common skin warts, genital warts and cervical cancer [1]. Over 100 types of HPVs have been identified and approximated one-third types of HPVs have been detected in genital diseases. HPV types 6 and 11 having been implicated in over 90% of genital warts, while HPV types 16 and 18 being responsible for 70% of cervical cancer [2, 3], which is second only to breast cancer among the causes of cancer-related death in women. Meanwhile, a considerable percentage of penile cancer is caused by HPV type 16 and 18. As a result, instead of being considered commonly that only exists in female, HPV disease is a significant treat to both genders.

The expression of HPV major capsid protein L1 as a recombinant protein has been reported by several study groups [4-7]. A recombinant quadrivalent HPV vaccine, composed of virus-like particles (VLPs) of HPV type 6, 11, 16 and 18 was developed to attain the greatest impact on HPV-related diseases [8]. HPV VLPs are obtained from recombinant capsid proteins expressed in yeast cells, which self-assemble into a capsid structure resembling the actual viral particles. A process for the purification of HPV VLPs has been described by Cook et al. [9] including cell disruption, nuclease treatment and microfiltration, followed by two chromatographic steps: a capture step and a

polishing step. The purified products are then further processed through disassembly and reassembly steps to form HPV VLPs with uniform diameter, approximately 60 nm according to Mach et al. [10].

In conventional chromatographic media, solute molecules reach the outer surface of adsorbent particles rapidly by convection; however, the kinetics of binding onto the particle interior surfaces is controlled by molecular diffusion, which is slow especially for adsorbates like large proteins and VLPs. Thus, significant band broadening occurs, resulting in poor resolution and lower dynamic binding capacity [11].

Perfusion chromatography media provide a potential solution to overcome slow intraparticle mass transfer by including a network of large interconnected convective through-pores (usually 600-800 nm in diameter), which crosses the particles from side to side and allows part of the mobile phase to flow or "perfuse" through the particle interior, as well as smaller pores (typically 80-150 nm in diameter), which provide the bulk of the surface area for binding [12]. Although the diffusive pores are accessed by diffusion alone, the shorter diffusion paths in these pores results in little overall resistance. By reducing the distance for the solute molecules to diffuse to the interior binding sites, this bimodal porous structure effectively eliminates the main cause of band broadening [13].

The capture step used in the process for the purification of VLPs described by Cook et al. of recombinant HPV Type 11 major capsid protein L1 uses POROS HS 50 (Life Technologies, NY, USA) as the chromatographic matrix [9]. POROS HS 50 is a strong cation exchanger, which has been characterized as "perfusion media". This rigid, poly (styrene-divinylbenzene) based material is surface-coated with a polyhydroxylated polymer gel layer functionalized with sulfopropyl groups. The internal structure of

POROS HS 50 has been reported to contain a bimodal distribution of pore sizes, with convective pores in the 600 to 800 nm range and the diffusive ores in the 50 to 150 nm range [14]. In this process, the VLPs are loaded onto a POROS HS 50 chromatography column and eluted with a salt gradient, following a wash step. It has been postulated that in the capture step, the convective pores are accessible to the VLPs so that binding may occur throughout the beads. Lee et al. reported, however, in the actual process, significant lot-to-lot variations in the elution behavior have been noted for different POROS HS 50 samples [15]. While similar purification levels could be achieved, loss of product occurs when the process was operated with a fixed product collection window due to the considerably shifting in the position of elution peak. The correlation between process performance and resin characteristic parameters remains unclear.

Perfusion chromatography matrices have been used in a number of analytical and process applications for proteins [13-21], plasmids [22], and VLPs [9]. Carta et al. [23] developed a theoretical model for perfusion chromatography in spherical particles using an effective medium, free surface model to describe intraparticle convection. Several models have been advanced later based on different assumptions, including a model accounting for the kinetics of binding [24], a model assuming a bidisperse pore structure to take into account transport in the diffusive pores [25-28], pore network models to describe the effects of pore connectivity and surface heterogeneity [29-30], and simplified linear driving force models [31-32]. However, the direct connection between theoretical models and experimental results has, so far, remained somewhat elusive.

Monoliths are another potential option to improve mass transfer of large biomolecules. Monoliths can be imagined as a converse structure of a packed bed, in

which the extraparticle void volume of the packed bed is replaced by a solid porous backbone similar to the interior structure of a chromatography media particle, while the space taken by the chromatography media becomes accessible to the mobile phase in the column and the contact points of particles becomes open flow channels with remarkable sizes [33]. In another words, monoliths are continuous porous matrices with 2-5 μm flow channels [34] and sealed against the wall of a tube. Compared to chromatography columns packed with particles, monoliths provide a much larger porosity available for flow, which dramatically decreases the hydraulic resistance in the column. Pores not accessible by flow can also exist inside the solid backbone. The efficiency of monoliths column is controlled by the size and fraction of both the flow channels and internal pore structure. One of the potential advantages of monolith column is the possibility to control the column efficiency by controlling the sizes of flow channels and the internal pores separately, as well as the size of the pores within the solid structure [33].

Due to the typical lower binding capacities caused by their smaller surface area, monoliths are generally thought to be not competitive with porous particles for the purification of smaller proteins since the diffusional transport of such proteins in porous media is not severely hindered [35]. However, transport of large proteins and VLPs in conventional porous media or even in perfusion chromatography matrices can be slow. Monoliths, on the other hand, do not present significant diffusional transport resistances and their performance is generally independent of molecular size [36]. Etzel presented a theoretical study that the molecule can access the entire area of the channels [37]. As a result, although the binding capacities are much lower for small proteins due to smaller

surface areas, monoliths may present very significant advantages for VLPs and large biomolecules because of the absence of mass transfer limitations.

According to their base materials, monoliths can be essentially classified into silica based [38] and polymer based monoliths [39]. The morphology and structure properties of monoliths columns are significantly affected by the properties of their base materials. Silica monoliths are typically composed of porous rod-shape silica skeleton with size of 0.3-5 μm, which form a bimodal porous structure with large through-pores of 0.5-8 μm between the rods and smaller mesopores of 2-30 nm inside the rods [40]. The resulting pore structure is very similar to packed beds with porous adsorbent particles. In terms of application, silica based monoliths are preferred for separation of low molecular weight molecules, such as polypeptides and aromatic compounds [33]. Polymer based monoliths, however, unlike silica based monoliths that are prepared in multiple steps to control the macropores size and skeleton thickness independently [38], are usually prepared in a single-step molding process involving polymerization reactions [41]. Although control of global porosity is achievable by careful formulation in the preparation, the globular porous polymeric skeleton of polymer based monoliths actually consists of soft matter formed of cross-linked polymer, which renders a much more heterogeneous structure with pore size distribution spanning over several orders of magnitude [42].

Polymer based monoliths have been used in many applications involving all kinds of biomolecules, including proteins [43-48], plasmid DNA [35, 49-51] and virus and VLPs [52-56]. However, there is no previous report of monoliths application on the capture step of HPV VLPs and the actual binding sites inside for HPV VLPs inside the

monoliths matrix is unknown. A potential disadvantage is that product recovery can be low as the adsorbate molecules can be become trapped in the flow channels. For example, Rupar et al. [57] reported that the recovery in the purification of Potato virus Y using monoliths column was only around 50%. It still remains unknown whether the heterogeneous porous structure of polymer based monoliths affects the adsorption and recovery of VLPs.

The overall objective of this project is to understand the adsorption and elution behavior of proteins and VLPs in large-pore perfusion chromatography media and in monoliths with emphasis on elucidating the relationship between adsorbent structure, molecular size, and adsorption properties. Chapter 2 describes the characterization of the critical structural properties of POROS HS 50 and the effects of perfusion on the intraparticle mass transfer of proteins and VLPs under both non-binding and strong binding conditions. Chapter 3 compares the results from POROS HS 20, an adsorbent structurally similar to POROS HS 50 but with only half of the particle diameter, to demonstrate the effects of particle size to the performance of perfusion chromatography media. Chapter 4 extends the study to a "Convective Interaction Media" (CIM®) SO3-1 "Tube" monolith column to investigate the performance of monoliths matrices on the adsorption and elution of proteins and VLPs.

1.2 Theoretical Background

In conventional chromatography media, the kinetics of biomolecular adsorption in porous particles is normally controlled by diffusion. The effective diffusivity of protein

molecules and bioparticles inside the resin particles is given by the following equation [58]:

$$D_e = \frac{\varepsilon_p D_0}{\tau_p} \psi_p \tag{1.1}$$

where ε_p is the intraparticle porosity (usually on the order of 0.5 for large pore matrices), τ_p is the tortuosity factor (on the order of 2 for practical porous stationary phases), D_0 is the free solution diffusivity, and ψ_p is the hindrance factor, which is described by Carta and Jungbauer [59] as a sharply decreasing function of the ratio of molecular radius, r_s, and pore radius, r_{pore}, as shown in Fig. 1.1. A characteristic diffusion time for particles of radius r_p can be estimated from the following equation:

$$\tau_D = \frac{r_p^2}{D_e} \tag{1.2}$$

which determines the minimum residence time that will allow effective binding in particle interior. For small molecules in non-viscous solvents, D_0 is generally on the order of 1×10^{-5} cm^2/s and ψ_p is around 1, since the ratio of molecule and pore size is small. However, as molecular size increases, both D_0 and ψ_p decrease resulting in very low D_e-values. For example, for a 150 kDa protein, $D_0 \sim 5\times10^{-7}$ cm^2/s and $r_s \sim 5$ nm. Accordingly, in 500 nm radius pores, $\psi_p \sim 0.95$ and $D_e \sim 1.2\times10^{-7}$ cm^2/s. For 100 μm particles (r_p = 50 μm), τ_D becomes on the order of 50 sec, which is quite high. Even higher values would be expected for VLPs due to their much lower D_0 (~7.3×10^{-8} cm^2/s) and much higher r_s of 30-50 nm. As a result, the time required for VLPs diffusing into 50 μm particles is about 12 min, more than one order of magnitude larger than for IgG diffusion in the same

particles, which would result in low productivity, large column volumes and high equipment and operating costs.

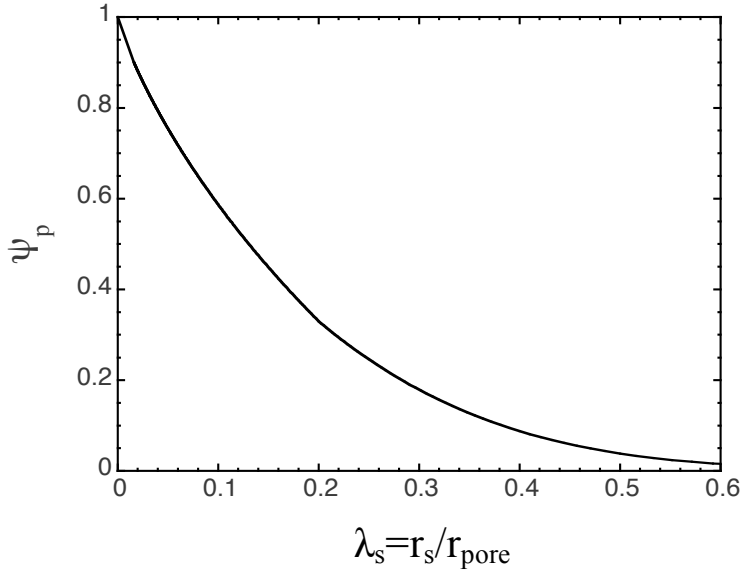

Figure 1.1. Relationship between hindrance factor, ψ_p, and molecular size, r_s, in pores of radius r_{pore} [59].

1.2.1 Intraparticle Convection

According to the above estimation, the binding capacity inside the particles is unlikely to be fully utilized by VLPs during adsorption by diffusion only. In perfusion chromatography media, the intraparticle transport is enhanced by the convective flow that occurs within the particle pores. In a packed bed, the driving force of such intraparticle flow is provided by the pressure drop across the particle; therefore, intuitively, the ratio of pore and particle size is critical to the intraparticle flow rate, with larger pores and smaller particles leading to greater intraparticle flow. For certain conditions, such intraparticle convective flow can enhance transport of the adsorbate giving overall rates that are higher

than for diffusion alone. A theoretical model was developed by Carta et al. [23, 25, 27] describing the convection-enhanced transport through an enhanced effective diffusivity $\widetilde{D}_e$ given by the following equation which is plotted in Fig. 1.2:

$$\frac{\widetilde{D}_e}{D_e} = \frac{Pe_{intra}}{3}\left[\frac{1}{\tanh\left(Pe_{intra}\right)} - \frac{1}{Pe_{intra}}\right]^{-1} \tag{1.3}$$

The ratio $\widetilde{D}_e / D_e$ represents the enhancement of intraparticle transport due to convection. $Pe_{intra} = ur_p F / 3D_e$ is an intraparticle Peclet number describing the relative importance of convective and diffusive transport. As seen in Fig. 1.2, in order to obtain significant effects of perfusion, a Pe_{intra} value larger than about 10 is required, while a Pe_{intra} value approaching 200 is needed to provide the 10-fold increased transport rates that would reduce diffusion times to typical ranges encountered in protein processing. *F* is the ratio of intraparticle and extraparticle flow velocities, and *u* the extraparticle flow velocities, which is related to the ratio of intraparticle and extraparticle hydraulic permeabilities [59]. Accordingly, *F* is proportional to $\left(r_{pore}/r_p\right)^2$, indicating that smaller particles with larger pore sized can provide larger Pe_{intra} and, thus, more enhancement by intraparticle convective flow.

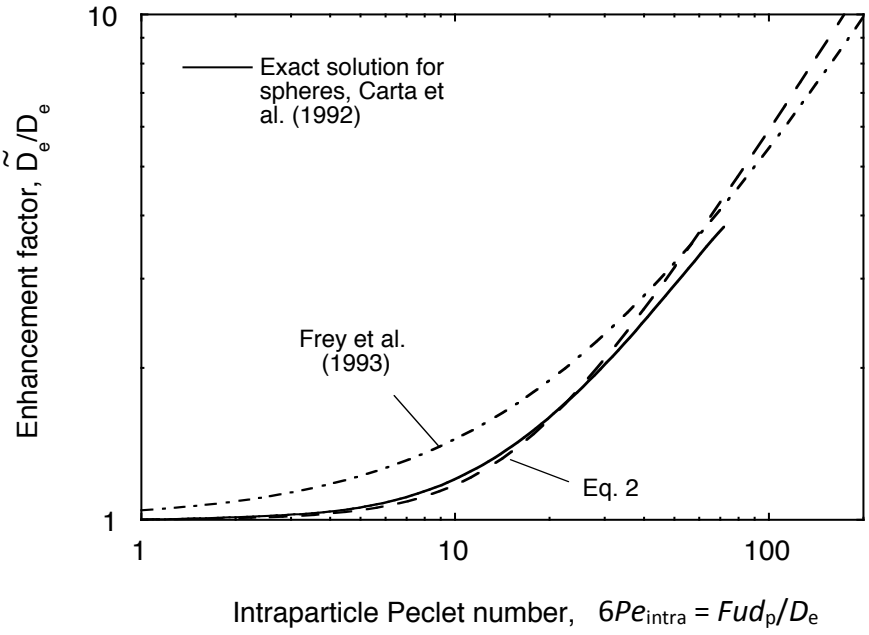

Figure 1.2. Relationship between convective enhancement factor of intraparticle transport and intraparticle Peclet number [23, 27]. *F* is the ratio of intraparticle and extraparticle flow rates.

1.2.2 Effect of Intraparticle Convection on Chromatographic Performance

Dynamic binding capacity (DBC), and the height equivalent to the theoretical plate (HETP) are two critical factors used to evaluate chromatographic performance. DBC describes the actual achievable binding capacity in a process operated at a given residence time, which is directly applicable to capture processes. DBC is fraction of the equilibrium binding capacity (EBC). Larger DBC-values generally result in greater productivity [59].

The HETP defines the number of separation plates, which is directly applicable to chromatographic resolution under linear or gradient elution conditions. A smaller HETP value indicates a higher number of plates in a column of certain length, giving better

separation performance. With reference to Fig. 1.3, the HETP for non-binding conditions in a bidisperse particle, consisting of spherical microparticles of radius r_m defining a network of perfusive macropores and diffusive micropores within the microparticles, is given by the following equation [25]:

$$h = a + \frac{1}{30}\frac{\varepsilon}{1-\varepsilon}\left(\frac{k'}{1+k'}\right)^2 \frac{\tau_M}{\varepsilon_M K_{D,M}}\left[\frac{D_e}{\widetilde{D}_e} + \frac{b-1}{b^2}\frac{\tau_m}{\tau_M}\left(\frac{r_m}{r_p}\right)^2\right]v' \qquad (1.4)$$

where $h = HETP/d_p$ and $b = 1 + (1-\varepsilon_M)\frac{\varepsilon_m K_{D,m}}{\varepsilon_M K_{D,M}}$. ε is the extraparticle porosity, ε_M and ε_m are the macroporosity and microporosity, respectively. The term

$$k' = \frac{1-\varepsilon}{\varepsilon}\left[\varepsilon_M K_{D,M} + (1-\varepsilon_M)\varepsilon_m K_{D,m}\right] \qquad (1.4a)$$

is the retention factor, $K_{D,M}$ and $K_{D,m}$ are partition coefficients in the macro and micropores, respectively. Based on a cylindrical pore model, $K_{D,M}$ and $K_{D,m}$ are related to molecular and pore size by the following equations:

$$K_{D,M} = (1 - r_s/r_{pore,M})^2 \qquad (1.4b)$$

$$K_{D,m} = (1 - r_s/r_{pore,m})^2 \qquad (1.4c)$$

r_m is the microsphere radius, and $v' = vd_p/D_0$ is the reduced velocity. In addition to the parameters already defined, eq. 1.4 also contains a, which describes hydrodynamic dispersion and is expected to be independent of flow rate, and τ_M the tortuosity factor in the macroparticle pores. Without intraparticle convection (F = 0), Pe_{intra} = 0 and $\widetilde{D}_e / D_e = 1$. Accordingly, h increases linearly with v'. Conversely, when F is large, a plot of h vs. v' levels off at high v', indicating that perfusion becomes dominant. For these conditions, chromatographic performance becomes independent of flow rate [25].

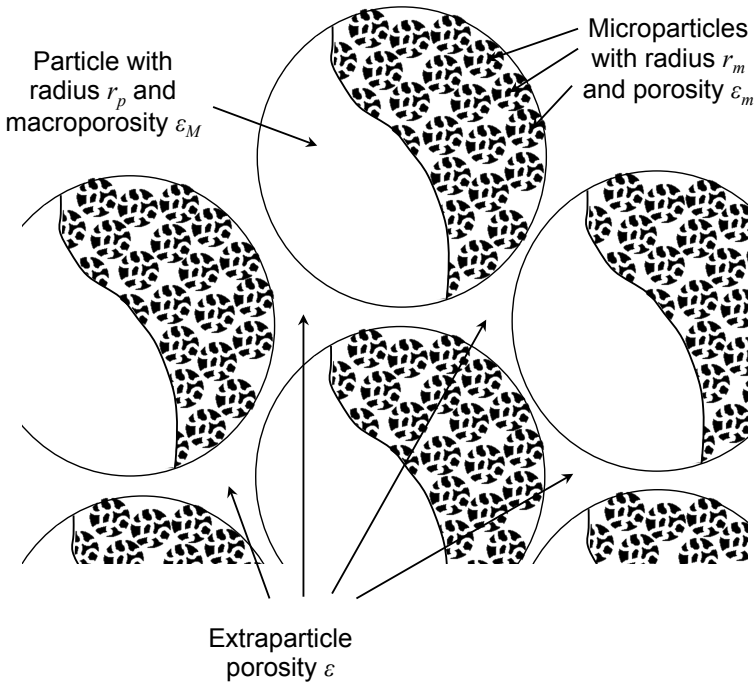

Figure 1.3. Sketch of particles with a bi-modal pore size distribution defining extraparticle porosity, ε, intraparticle macroporosity, ε_{M}, and intraparticle microporosity, ε_{m}.

The potential advantages of perfusion can be seen from eq. 1.4. For given particle properties, F is expected to be a constant for different solutes and flow velocities. In this case, whether perfusion is significant or not depends on the values of D_{e} and u. For a small protein, D_{e} is relatively large. Thus, even at large values of u, Pe_{intra} is small and $\widetilde{D}_{\mathrm{e}} / D_{\mathrm{e}} \sim 1$. For a large protein or bioparticles like VLPs, D_{e} is very small. Thus, even at relatively low u, Pe_{intra} can be large and $\widetilde{D}_{\mathrm{e}} / D_{\mathrm{e}} >> 1$, leading to lower HETP than for diffusion alone. The consequences of lower HETP's are greater resolution in chromatographic separation and greater dynamic binding capacity in capture applications [59].

1.2.3 Mass Transfer in Monolithic Columns

The performance of monoliths columns has been evaluated by numerous studies, especially with regards to hydraulic permeability and chromatographic efficiency. For both silica and polymer-based monoliths, the pressure drop over the column can be related to the column permeability, B_0, by Darcy's law [60-61]:

$$\frac{\Delta P}{L} = \frac{\eta u}{B_0} \tag{1.5}$$

where $\Delta P/L$ is the pressure drop per unit length of column, η the viscosity of the mobile phase and u the mobile phase superficial velocity. The permeabilities of typical silica monoliths are on the order of 10^{-14} m^2 [33], which is several-fold higher than those for columns packed with particles that provide the same column efficiency. A broad range of permeabilities has been reported for polymeric monoliths between [42, 62-63].

Several studies have shown that the HETP for small molecules in silica monoliths is essentially independent of flow [64-66], indicating the band broadening is mainly caused by axial dispersion and/or flow non-uniformity [67]. However, sloping HETP curves are observed for large molecules, which is likely due to the diffusional resistance in smaller pores [66]. A simplified model was presented for silica monoliths columns, which assumed that the monoliths consists of a random assembly of anastomosed cylindrical rods of porous backbone material (radius R_{ss}) which provides an internal porosity ε_i , surrounded by annular through-pores which occupy a volume fraction ε_e. Based on this assumed physical structure, Miyabe et al. [67] developed the following model:

$$HETP = \frac{D_L}{u} + 2u\frac{\delta_f}{\delta_0^2} + 2u\frac{\delta_d}{\delta_0^2} \tag{1.6}$$

where D_L is the axial dispersion coefficient and u is the superficial velocity of the mobile phase. The parameters δ_f, δ_d and δ_0 are defined as following:

$$\delta_f = (1-\varepsilon_e)\frac{R_{ss}}{2k_f}\left[\varepsilon_i + (1-\varepsilon_i)K_a\right]^2 \quad (1.6.\text{ a})$$

$$\delta_d = (1-\varepsilon_e)\frac{R_{ss}}{2D_e}\left[\varepsilon_i + (1-\varepsilon_i)K_a\right]^2 \quad (1.6.\text{ b})$$

$$\delta_0 = \varepsilon_e + (1-\varepsilon_e)\left[\varepsilon_i + (1-\varepsilon_i)K_a\right] \quad (1.6.\text{ c})$$

where k_f is the external mass transfer coefficient, D_e the effective diffusivity, and K_a the adsorption equilibrium constant. HETP values obtained from the first and second moments of pulse response experiments data, together with physical properties obtained from other methods such as iSEC and TEM, can be used to determine the D_e value by comparison with eq. 1.6.

For polymer monoliths column, the HETP values that have been reported are virtually independent of mobile phase velocity even for large molecules, suggesting that diffusional resistances are completely absent and that hydrodynamic dispersion and extra-column effects dominate band broadening phenomenon [34, 67-68]. Trilisky and Lenhoff [69] measured the HETPs of different monolithic columns with adsorbates of different molecular sizes (NaCl, uridine monophosphate, ovalbumin and BSA) to fit with the model. By comparing their data to eq. 1.6, these authors concluded that the first term is generally dominant.

1.3 List of Symbol

ε extraparticle porosity

ε_e	porosity of through pores in the geometric model of monolithic column
ε_i	internal porosity of the cylindrical rods in the geometric model of monolithic columns
ε_M	macropore porosity
ε_m	micropore porosity
ε_p	intraparticle porosity
η	mobile phase viscosity (Pa·s)
τ_D	characteristic diffusion time (s)
τ_M	tortuosity factor in macroparticle pores
τ_m	tortuosity factor in microparticle pores
τ_p	tortuosity factor
ψ_p	hindrance factor
a	hydrodynamic dispersion factor
B_0	hydraulic permeability, m^2
D_0	free solution diffusivity (cm^2/s)
D_e	effective diffusivity (cm^2/s)
$\tilde{D}_e$	convection enhanced effective diffusivity (cm^2/s)
d_p	particle diameter (cm)
F	ratio of intraparticle and extraparticle flow velocities
$HETP$	height equivalent to the theoretical plate (cm)

h	reduced HETP
K_{a}	adsorption equilibrium constant (L/g)
$K_{\mathrm{D,M}}$	size exclusion in the macroparticle pores
$K_{\mathrm{D,m}}$	size exclusion in the microparticle pores
k'	retention factor
k_{f}	external mass transfer coefficient (cm/s)
L	Column length, m
ΔP	Column pressure drop, Pa
Pe_{intra}	intraparticle Peclet number
R_{ss}	radius of the cylindrical rods in the geometric model of monolithic columns (nm)
r_{m}	microsphere radius (nm)
r_{p}	particle radius (μm)
$r_{\mathrm{pore,M}}$	macropore radius (nm)
$r_{\mathrm{pore,m}}$	micropore radius (nm)
r_{s}	molecular radium (nm)
t	time (s)
u	superficial velocity (cm/s)
v	fluid velocity (cm/s)
v'	reduced velocity ($=vd_{\mathrm{p}}/D_0$)

1.4 References

[1] Shi, L., Sanyal, G., Ni, A., Luo, Z., Doshna, S., Wang, B., Graham, T. L., et al. (2005). Stabilization of human papillomavirus virus-like particles by non-ionic surfactants. *J. Pharm. Sci.*, *94*(7), 1538-51.

[2] Chen, X. S., Garcea, R. L., Goldberg, I., Casini, G., Harrison, S. C. (2000). Structure of small virus-like particles assembled from the L1 protein of human papillomavirus 16. *Mol. cell*, *5*(3), 557-67.

[3] Bryan, J. T. (2007). Developing an HPV vaccine to prevent cervical cancer and genital warts. *Vaccine*, *25*(16), 3001-6.

[4] Zhou, J., Sun, X. Y., Stenzel, D. J., Frazer, I. H. (1991). Expression of vaccinia recombinant HPV 16 L1 and L2 ORF proteins in epithelial cells is sufficient for assembly of HPV virion-like particles. *Virology*, *185*(1), 251-7.

[5] Kirnbauer, R., Booy, F., Cheng, N. (1992). Papillomavirus L1 major capsid protein self-assembles into virus-like particles that are highly immunogenic. *Proc. Natl. Acad. Sci. 89*(24), 12180-4.

[6] Rose, R.C., Bonnez, W., Reichman, R.C., Garcea, R.L. (1993). Expression of human papillomavirus type 11 L1 protein in insect cells: in vivo and in vitro assembly of viruslike particles. *J. Virol. 67*(4), 1936-44.

[7] Hagensee, M. E., Yaegashi, N., Galloway, D. A. (1993). Self-Assembly of Human Papillomavirus Type 1 Capsids by Expression of the Li Protein Alone or by Coexpression of the Li and L2 Capsid Proteins. *J. Virol. 67*(1), 315-322.

[8] Shi, L., Sings, H. L., Bryan, J. T., Wang, B., Wang, Y., Mach, H., Kosinski, M., et al. (2007). GARDASIL: prophylactic human papillomavirus vaccine development--from bench top to bed-side. *Clin. Pharmacol. Ther.*, *81*(2), 259-64.

[9] Cook, J. C., Joyce, J. G., George, H. a, Schultz, L. D., Hurni, W. M., Jansen, K. U., Hepler, R. W., et al. (1999). Purification of virus-like particles of recombinant human papillomavirus type 11 major capsid protein L1 from Saccharomyces cerevisiae. *Protein Express. Purif.*, *17*(3), 477-84.

[10] Mach, H., Volkin, D. B., Troutman, R. D., Wang, B., Luo, Z., Jansen, K. U., Shi, L. (2006). Disassembly and reassembly of yeast-derived recombinant human papillomavirus virus-like particles (HPV VLPs). *J. Pharm. Sci.*, *95*(10), 2195–2206.

[11] Whitney, D., McCoy, M., Gordon, N., Afeyan, N. (1998). Characterization of large-pore polymeric supports for use in perfusion biochromatography. *J. Chromatogr. A, 807*(2), 165-84.

[12] Garcıa, M.C., Marina, M.L., Torre, M. (2000). Perfusion chromatography: an emergent technique for the analysis of food proteins. J.Chromatogr. A, 880, 169–187.

[13] Rodrigues, A. E. (1997). Permeable packings and perfusion chromatography in protein separation. *J. Chromatogr. B, 699*(1-2), 47-61.

[14] Afeyan, N. B., Gordon, N. F., Mazsaroff, I., Varady, L., Fulton, S. P., Yang, Y. B., & Regnier, F. E. (1990). Flow-through particles for the high-performance liquid chromatographic separation of biomolecules: perfusion chromatography. *J. Chromatogr., 519*(1), 1-29.

[15] Lee, L., Suchechi, J., Apgar, K., Hue, C., Gentzler, M., Abraham, D. (2007). Process-Specific Range Finding of Chromatography Resin Lots Used in the Purification Process of a Recombinant Product. 234th ACS National Meeting, Aug, 2007,Boston, MA

[16] Wajcman, H., Ducrocq, R., Rious, J., Mathis, M., Godart, C., Prehu, C., Galacteros, F. (1996). Perfusion chromatography on reversed-phase column allows fast analysis of human globin chains. *Anal. Biochem., 237*(1), 80-87.

[17] McCarthy, E., Vella, G., Mhatre, R., Lim, Y.P. (1996). Rapid purification and monitoring of immunoglobulin M from ascites by perfusion ion-exchange chromatography. *J. Chromatogr. A, 743*(1), 163-170.

[18] Fahrner, R.L., Whitney, D.H., Vanderlaan, M., Blank, G.S. (1999). Performance comparison of Protein A affinity-chromatography sorbents for purifying recombinant monoclonal antibodies. *Biotechnol. Appl. Biochem., 30* (2), 121-128.

[19] Savary, B.J. (2001). Perfusion chromatography separation of the tomato fruit-specific pectin methylesterase from a semipurified commercial enzyme preparation. *Prep. Biochem. Biotechnol., 31* (3), 241-258.

[20] Losso, J.N., Bansode, R.R., Bawadi, H.A. (2003). Perfusion Chromatography Purification of a 15 kDa Rice Prolamin. *J. Agric. Food Chem., 51*(24), 7122-7126.

[21] Heras, J.M., Marina, M.L., García, M.C. (2007). Development of a perfusion ion-exchange chromatography method for the separation of soybean proteins and its application to cultivar characterization. *J. Chromatogr. A, 1153*(1-2), 97-103.

[22] Limonta, M., Márquez, G., Rey, I.a, Pupo, M., Ruiz, O., Amador-Cañizares, Y., Dueñas-Carrera, S. (2008). Plasmid DNA recovery using size-exclusion and perfusion chromatography. *Biopharm. Int., 21*(9), 38-48.

[23] Carta, G., Gregory, M.E., Kirwan, D.J., Massaldi, H.A. (1992). Chromatography with permeable supports: Theory and comparison with experiments. *Sep. Technol., 2*(2), 62-72.

[24] Liapis, A.I., McCoy, M.A. (1992). Theory of perfusion chromatography. *J. Chromatogr., 599*(1-2), 87-104.

[25] Carta, G., Rodrigues, A.E. (1993). Diffusion and convection in chromatographic processes using permeable supports with a bidisperse pore structure. *Chem. Eng. Sci., 48*(23), 3927-3935.

[26] Rodrigues, A.E., Lu, Z.P., Loureiro, J.M., Carta, G. (1993). Peak resolution in linear chromatography. Effects of intraparticle convection. *J. Chromatogr. A, 653*(2), 189-198.

[27] Frey, D.D., Schweinheim, E., Horváth, C. (1993). Effect of intraparticle convection on the chromatography of biomacromolecules. *Biotechnol. Prog., 9*(3), 273-284.

[28] Liapis, A.I., Xu, Y., Crosser, O.K., Tongta, A. (1995). "Perfusion chromatography". The effects of intra-particle convective velocity and microsphere size on column performance. *J. Chromatogr. A, 702*(1-2), 45-57.

[29] Meyers, J.J., Crosser, O.K., Liapis, A.I. (2001). Pore network modelling: Determination of the dynamic profiles of the pore diffusivity and its effect on

column performance as the loading of the solute in the adsorbed phase varies with time. *J. Chromatogr. A, 908*(1-2), 35-47.

[30] Geng, A., Loh, K.C. (2004). Effects of adsorption kinetics and surface heterogeneity on band spreading in perfusion chromatography - A network model analysis. *Chem. Eng. Sci., 59*(12), 2447-2456.

[31] Carta, G. (1995). Linear driving force approximation for intraparticle diffusion and convection in permeable supports. *Chem. Eng. Sci., 50*(5), 887-889.

[32] Rodrigues, A.E., Chenou, C., De La Rendueles Vega, M. (1996). Protein separation by liquid chromatography using permeable POROS Q/M particles. *Chem. Eng. J., 61*(3), 191-201.

[33] Guiochon, G. (2007). Monolithic columns in high-performance liquid chromatography. *J. Chromatogr. A, 1168*, 101-168.

[34] Jungbauer, A., Hahn, R. (2008). Polymethacrylate monoliths for preparative and industrial separation of biomolecular assemblies. *J. Chromatogr. A, 1184*(1-2), 62-79.

[35] Urthaler, J., Schlegl, R., Podgornik, A., Strancar, A., Jungbauer, A., Necina, R. (2005). Application of monoliths for plasmid DNA purificationDevelopment and transfer to production. *J. Chromatogr. A, 1065*(1), 93-106.

[36] Wang, P.G. (2010) Monolithic Chromatography and Its Modern Applications. ILM Publications, Hertfordshire, UK.

[37] Etzel, M. R. Layered stacks, In Monolithic Materials; Preparation, Properties, and Allications, Svec, F., Tennikova, T. B., Deyl, Z., Eds.; Journal of Chromatography Library; Elsevier: Boston, 2003; pp 213 -234.

[38] Ishizuka, N., Minakuchi, H., Nakanishi, K., Soga, N., Tanaka, N. (1998). Designing monolithic double-pore silica for high-speed liquid chromatography. *J. Chromatogr. A, 797*(1-2), 133-137.

[39] Tennikova, T.B., Bleha, M., Švec, F., Almazova, T.V., Belenkii, B.G. (1991). High-performance membrane chromatography of proteins, a novel method of protein separation. *J. Chromatogr. A, 555*(1-2), 97-107.

[40] Nakanishi, K., Soga, N. (1991). Phase Separation in Gelling Silica–Organic Polymer Solution: Systems Containing Poly(sodium styrenesulfonate). *J. Am. Ceram. Soc., 74*(10), 2518–2530.

[41] Švec, F., Tennikova, T.B., Deyl, Z. (2003) Monolithic Materials: Preparation, Properties, and Applications. Elsevier, Amsterdam.

[42] Trilisky, E.I., Koku, H., Czymmek, K.J., Lenhoff, A.M. (2009). Relation of structure to performance characteristics of monolithic and perfusive stationary phases. *J. Chromatogr. A, 1216*(36), 6365-6376.

[43] Brne, P., Podgornik, A., Benčina, K., Gabor, B., Štrancar, A., Peterka, M. (2007). Fast and efficient separation of immunoglobulin M from immunoglobulin G using short monolithic columns. *J. Chromatogr. A, 1144*(1), 120-125.

[44] Ostryanina, N.D., Vlasov, G.P., Tennikova, T.B. (2002). Multifunctional fractionation of polyclonal antibodies by immunoaffinity high-performance monolithic disk chromatography. *J. Chromatogr. A, 949*(1-2), 163-171.

[45] Freitag, R., Vogt, S. (2000). Comparison of particulate and continuous-bed columns for protein displacement chromatography. *J. Biotechnol., 78*(1), 69-82.

[46] Podgornik, H.a, Podgornik, A. (2004). Separation of manganese peroxidase isoenzymes on strong anion-exchange monolithic column using pH-salt gradient. *J. Chromatogr. B, 799*(2), 343-347.

[47] Josic, D., Lim, Y.-P., Strancar, A., Reutter, W. (1994). Application of high-performance membrane chromatography for separation of annexins from the plasma membranes of liver and isolation of monospecific polyclonal antibodies. *J. Chromatogr. B, 662*(2), 217-226.

[48] Isobe, K., Kawakami, Y. (2007). Preparation of convection interaction media isobutyl disc monolithic column and its application to purification of secondary alcohol dehydrogenase and alcohol oxidase. *J. Chromatogr. A, 1144*(1), 85-89.

[49] Danquah, M.K., Forde, G.M. (2007). The suitability of DEAE-Cl active groups on customized poly(GMA-co-EDMA) continuous stationary phase for fast enzyme-free isolation of plasmid DNA. *J. Chromatogr. B, 853*(1-2), 38-42.

[50] Benčina, M., Podgornik, A., Štrancar, A. (2004). Characterization of methacrylate monoliths for purification of DNA molecules. *J. Sep. Sci., 27*(10-11), 801-810.

[51] Zoechling, A., Hahn, R., Ahrer, K., Urthaler, J., Jungbauer, A. (2004). Mass transfer characteristics of plasmids in monoliths. *J. Sep. Sci., 27*(10-11), p. 819-827.

[52] Kramberger, P., Peterka, M., Boben, J., Ravnikar, M., Štrancar, A. (2007). Short monolithic columns-A breakthrough in purification and fast quantification of tomato mosaic virus. *J. Chromatogr. A, 1144*(1), 143-149.

[53] Kramberger, P., Petrovic, N., Strancar, A., Ravnikar, M. (2004). Concentraion of plant viruses using monolithic chromatographic supports. *J. Virol. Methods, 120*(1), 55-57.

[54] Wickramasinghe, S.R., Carlson, J.O., Teske, C., Hubbuch, J., Ulbricht, M. (2006). Characterizing solute binding to macroporous ion exchange membrane adsorbers using confocal laser scanning microscopy. *J. Membr. Sci., 281*(1-2), 609-618.

[55] Williams, S.L., Eccleston, M.E., Slater, N.K.H. (2005). Affinity capture of a biotinylated retrovirus on macroporous monolithic adsorbents: Towards a rapid single-step purification process. *Biotechnol. Bioeng., 89*(7), 783-787.

[56] Gerster, P., Kopecky, E.M., Hammerschmidt, N., Klausberger, M., Krammer, F., Grabherr, R., Mersich, C., Urbas, L., Kramberger, P., Paril, T., Schreiner, M., Nöbauer, K., Razzazi-Fazeli, E., Jungbauer, A. (2013). Purification of infective baculoviruses by monoliths. *J. Chromatogr. A, 1290*, 36-45.

[57] Rupar, M., Ravnikar, M., Tusek-Znidaric, M., Kramberger, P., Glais, L., Gutierrez-Aguirre, I. (2013). Fast purification of the filamentous Potato virus Y using monolithic chromatographic supports. *J. Chromatogr. A, 1272*, 33-40.

[58] LeVan, M.D., Carta, G., Yon, C.M. (1997) Adsorption and Ion Exchange Perry's Chemical Engineers Handbook. (7th Edition), Sect. 16, McGraw-Hill, Columbus.

[59] Carta, G., Jungbauer, A. (2010) Protein Chromatography: Process Development and Scale-Up, Wiley-VCH, Weinheim, Germany.

[60] Darcy, H. (1856). Les Fontaines Publiques de la Ville de Dijon, Dalmont, Paris.

[61] Guiochon, G., Felinger, A., Katti, A.M., Shirazi, D. (2006) Fundamentals of Preparative and Nonlinear Chromatography, Elsevier, Amsterdam, The Netherlands.

[62] Mihelic, I., Nemec, D., Podgornik, A., Koloini, T. (2005). Pressure drop in CIM disk monolithic columns. *J Chromatogr A., 1065*(1), 59-67.

[63] Leinweber, F.C., Tallarek, U. (2003). Chromatographic performance of monolithic and particulate stationary phases. Hydrodynamics and adsorption capacity. *J Chromatogr A., 1006*(1-2), 207-228.

[64] van Deemter, J.J., Zuiderweg, F.J., Klinkenberg, A. (1956). Longitudinal diffusion and resistance to mass transfer as causes of nonideality in chromatography. *Chem. Eng. Sci. 5*(6), 271-289.

[65] Minakuchi H, Nakanishi K, Soga N, Ishizuka N, Tanaka N. (1997). Effect of skeleton size on the performance of octadecylsilylated continuous porous silica columns in reversed-phase liquid chromatography. *J Chromatogr A., 762*(1-2), 135-146.

[66] Minakuchi H, Nakanishi K, Soga N, Ishizuka N, Tanaka N. (1998). Designing monolithic double-pore silica for high-speed liquid chromatography. *J Chromatogr A., 797*(1-2), 133-137.

[67] Miyabe, K., Cavazzini, A., Gritti, F., Kele, M., Guiochon, G. (2003). Moment Analysis of Mass-Transfer Kinetics in C18-Silica Monolithic Columns. *Anal. Chem., 75*(24), 6975-6986.

[68] Jungbauer, A. (2005) Chromatographic media for bioseparation. *J Chromatogr A., 1065*(1), 3-12.

[69] Trilisky, E., Lenhoff, A. (2010). Effect of bioparticle size on dispersion and retention in monolithic and perfusive beds. *J Chromatogr A. 1217*(47), 7372-7384.

Chapter 2
Proteins and Virus-like Particle Adsorption on POROS HS 50

2.1 Introduction

Perfusion chromatography was introduced commercially in the early 90's, primarily based on so called POROS chromatography beads. Afeyan et al. [1] described POROS as a perfusion material composing convective pores in 600 to 800 nm range while and diffusive pores in 50 to 150 nm range. The use of POROS HS 50 for the purification of VLPs of recombinant HPV Type 11 major capsid protein L1 was reported by Cook et al. [2]. These authors postulated that the convective pores inside POROS HS 50 are accessible by VLPs so that the binding of VLPs occurs throughout the entire particles. Despite this claim, to date there is no direct empirical evidence that VLPs actually get into these pores nor is known at what rate this takes places. In the process described by Cook et al., the VLP protein load on the POROS 50 HS column was only 3.4 mg/ml, with a recovery of only 12% [2]. At such low loads, the possibility that VLP binding is limited to the external surface of the beads exists. Regardless of the mechanism and location of binding, it is clear that particle size and pore morphology and flow rate are likely to affect VLP transport and chromatographic performance in a significant way.

Uncertainties also exist with regard to the actual size of these VLPs. For example, Chen et al. and Mach et al. [3,4] reported a VLPs size of 60 nm in diameter obtained from TEM images. However, a larger diameter of 120-160 nm was reported by Shi et al. [5] based on dynamic light scattering (DLS) analysis. Various models of perfusion

chromatography have been developed in multiple studies as discussed in Chapter 1 and some indirect experimental evidence has been offered to demonstrate the connection between theoretical models and experimental results. In general, the evidence stems mainly form the trend of HETP and/or DBC as a function of flow rate. For small particles (20 μm or less) with large pores, trends of constant HETP and DBC at high flow rates have been confirmed [6-9]. For larger particles (eg. 50 μm diameter), McCoy et al. [6] reported flow-rate independent HETP for Lyo for non-binding conditions at velocities as low 1000 cm/h, indicating a strong perfusion effect, while conflicting results have been reported by Weaver and Carta [10], that the DBC for the same protein continued to decrease nearly linearly at velocities as high as 4000 cm/h and in a manner quantitatively consistent with diffusion alone. The conflicting results may be partially due to the difficulties inherent in a precise determination of HETP from peaks eluted at high mobile phase velocities. Another possibility is that the bound protein molecules hinder intraparticle convection giving different results for non-binding and for binding conditions. Pferffer et al. [11] reported direct measurements of the hydraulic permeability of larger particles and obtained permeabilities that were 4–17 times larger than previous estimates, leading to the hypothesis that the particles contain a highly inhomogeneous distribution of pores, with a few very large through pores carrying most of the intraparticle flow surrounded by much smaller pores where little flow occurs. In this case, much larger resistances to transport in the diffusive pores that would negate many of the benefits of high intraparticle flow could be predicted.

Liapis et al. [12] presented a mathematical model to describe the intraparticle concentration profile of the adsorbate inside spherical perfusive adsorbent particles. For

strong binding conditions, this model predicts spherically asymmetrical intraparticle profiles that are increasingly skewed in the direction of flow at high Pe_{intra}. Since the shape of intraparticle concentration profiles is generally very sensitive to the exact nature of the dominant transport mechanism, a quantitative determination of these profiles is expected to provide significant insight for conditions similar to those used in many practical applications. This observation suggests an alternative way of elucidating under what conditions perfusion takes place by determining the intraparticle progress of the adsorption front of a strongly bound adsorbate during a transient adsorption experiment. To our knowledge, however, such data are not currently available. The objective of this part of the dissertation is thus threefold: (1) to determine the structural characteristics of POROS HS 50 resin and its HETP for non-binding conditions; (2) to develop a method based on confocal laser scanning microscopy (CLSM) to determine intraparticle adsorbed concentration profiles for proteins and VLPs, as well as for fluorescent labeled latex nanoparticles with similar size to the VLPs; and (3) to obtain intraparticle profiles under both no flow and high flow conditions and compare the results to available perfusion theories.

2.2 Materials and Methods

2.2.1 Materials

The resin used in this work, POROS HS 50, was obtained from Applied Biosystems (Life Technologies Corporation, Grand Island, NY). According to the supplier, POROS HS 50 is based on a rigid poly(styrene-divinylbenzene) backbone functionalized with strong cation exchange groups and containing 50-1000 nm pores. The average particle diameter, d_p, of the sample is reported by the supplier of about 50 μm. Six lots of POROS HS 50 were obtained and preliminary resin structure tests were conducted on all six lots. All the other experiments were conducted using Lot 250-406, if not stated specifically.

The proteins used in this work include chicken egg white lysozyme (Lyo) and bovine thyroglobulin (Tg), obtained from Sigma Chemical Co. (St. Louis, MO), and a monoclonal antibody (IgG) with pI 8.6 available in our laboratory [13]. The molecular mass of the mAb is about 150 kDa, determined by non-reducing SDS-PAGE. The protein sample was characterized by size-exclusion chromatography (SEC) using a Superdex 200 size-exclusion column (10 × 200 mm) obtained from GE Healthcare and the purity of the sample was determined as >99% monomer. Purified virus-like particles (VLPs) of recombinant human papillomavirus (HPV) Type 11 capsid protein L1 were obtained from Merck & Co., Inc. (West Point, NJ). Two batches of VLP samples were received (Lot 0311223-0001b and c) and both samples showed similar hydrodynamic radius measurements, r_s, and initial VLP concentration in the stock solution. The VLPs were purified from *S. Cerevisiae* as described by Cook et al. [2]. The samples were thawed out

by immersing the containers in room temperature water. After adding 0.01-0.015% PS-80, the samples were divided in smaller portions and stored at -80°C.

The hydrodynamic radius, r_s, of the test solutes used were determined by dynamic light scattering (DLS), using a Dynapro Nanostar unit (Wyatt Technology Corporation, CA), which gave values of 5.5 ± 0.5, 8.5 ± 1.0, and 50 ± 10 nm, for IgG, Tg, and VLP samples, respectively. The corresponding solution diffusivities, D_0, at 25 °C are 4.0×10^{-7}, 2.6×10^{-7}, and 3.5×10^{-8} cm^2/s. The IgG and Tg radii are consistent with molecular masses of 150 and 700 kDa, respectively. The VLP radius is consistent with previous measurements by Shi et al. [5]. The hydrodynamic radius of Lyo was not measured, but it is estimated to be 2.0 nm, based on its known D_0-value of 1.1×10^{-6} cm^2 /s [14].

HPV VLPs purified from yeast are unstable and tend to aggregate in low ionic strength solutions without stabilizers. Shi et al. reported an increase of VLPs diameter from 105 nm to 160 nm after one day storage at room temperature [5]. HPV VLPs also adsorb on the container surfaces, especially glass surfaces, during storage and analysis. Following Shi et al., polysorbate 80 was used to stabilize HPV VLPs in low ionic strength solutions and prevent adsorption to container [5]. Polysorbate 80 is a non-ionic surfactant with the following structure:

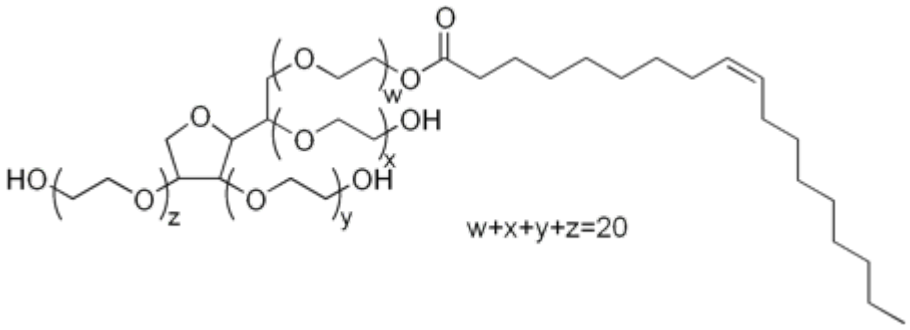

Figure 2.1. Molecular structure of polysorbate 80.

In this work, 0.015% of PS-80, obtained from Amresco LLC (Solon, OH) was added to all the HPV VLP samples and buffers. These solutions remained stable for several days at 4 °C and for at least one day at room temperature.

2.2.2 Methods

The particle size distribution of POROS 50HS resin was obtained from microphotographs taken with a CCD camera (model VCC-3972, Sanyon, Gardena, CA) attached to a white light microscope (model Eclipse E200, Nikon, Melville, NY) at 100X magnification. The resin was suspended in aqueous solution prior to the test. The photographs were analyzed by Image J. The volume-average particle diameter and standard deviation of the particle size distribution were then calculated from the following equations:

$$\bar{d}_{\mathrm{p}} = \sum_{\mathrm{j}=1}^{\mathrm{M}} f_{\mathrm{j}} d_{\mathrm{p,j}} \tag{2.1}$$

$$\sigma_{\mathrm{p}} = \sqrt{\sum_{\mathrm{j}=1}^{\mathrm{M}} f_{\mathrm{j}} \left(d_{\mathrm{p,j}} - \bar{d}_{\mathrm{p}} \right)^2} \tag{2.2}$$

where f_{j} is the volume fraction of particles of diameter $d_{\mathrm{p,j}}$.

Transmission electron microscopy (TEM) was used to determine the internal structure of POROS 50 HS. For this purpose, the particles were first dehydrated by washing them with water-ethanol mixtures increasing from 0 to 100% ethanol. The dehydrated particles where then embedded in LRWhite resin (London Resin Company, London, UK), by first saturating them with a 50:50 (v/v) mixture of ethanol and LRWhite and then with 100% LRWhite. After curing overnight at 45 °C, the embedded samples

were sectioned with an ultramicrotome to produce 80 nm slices, which were then imaged with a Jeol 100 CX transmission electron microscope.

Inverse size exclusion chromatography (iSEC) was used to determine the accessible intraparticle volume and the apparent pore size using glucose and dextran samples with molecular mass between 4 and 2000 kDa, obtained from Spectrum Chemical Manufacturing Co. (Gardena, CA). For this purpose, the resin was flow packed in 0.5 cm × 5 cm columns operated at a flow rate of 0.5 mL/min (150 cm/h) with a mobile phase containing 1 M NaCl in 10 mM Na_2HPO_4 at pH 7.0. 10–20 μL injections of each probe were made with a Waters HPLC system. The first moment of each peak, μ, was obtained by calculating the apparent first moment and subtracting from it the first moment obtained without the resin using the columns with inlet and outlet plungers pushed together. The extraparticle porosity, ε = 0.326, used to determine the distribution coefficient $K_D = \left(CV - \varepsilon\right)/\left(1 - \varepsilon\right)$, where $CV = \mu/V_{\text{column}}$ is the mean retention volume, μ, divided by the column volume, V_{column}, was obtained from the column pressure drop as a function of flow rate using the Carman–Kozeny equation [15]:

$$\Delta P = 150\frac{\left(1-\varepsilon\right)^2}{\varepsilon^3}\frac{\eta u L}{\bar{d}_{\text{p}}^2} \tag{2.3}$$

where η is the viscosity, u the superficial velocity, L the column length, and $\bar{d}_{\text{p}}$ the particle average diameter.

The iSEC probes used in this work include dextran standards shown in Table 4.3 along with their hydrodynamic radii as well the three proteins: Lyo, IgG and Tg, and VLPs. The hydrodynamic radius of the dextran probes were calculated by the following equation [16]:

$$r_s = 0.0271 \times MW^{0.498} \quad (2.4)$$

For these conditions, there is no binding but only steric exclusion for both dextran and protein probes. Thus, elution volume of these probes marks the accessible particle volume.

Table 2.1. Probes used for iSEC

Dextran	MW (kDa)	r_s (nm)
D2000	2000000	37.1
D500	500000	18.6
D250	250000	13.2
D150	150000	10.2
D70	70000	7.0
D40	40000	5.3
D10	10000	2.7
D4	4000	1.7
Glucose	18	0.36

Protein	MW (kDa)	r_s (nm)
Lyo	14.5	2.3
IgG	150	5.5
Tg	660	8.5
VLP	~20,000	50

Isocratic pulse response experiments were conducted to determine pore accessibility by proteins and VLPs under non-binding conditions and to determine the HETP as a function of mobile phase velocity. These measurements were made with a 0.5 × 5 cm columns at flow rates of 0.2 to 4 mL/min (60–1200 cm/h) using an AKTA Explorer 10 unit (GE Healthcare, Piscataway, NJ). Experiments were conducted with 20 μL injections in phosphate buffer of 20 mM Na_2HPO_4 at pH 7.0 with 1 M NaCl for Lyo, IgG and Tg and in 1.5 M NaCl and 0.015% PS-80 for the VLPs with detection at 280nm. Pulse injections without the resin and the two column plungers joined together were also

done to determine the extra column volumes. The ensuing peaks were analyzed by the moment method as discussed by Carta and Jungbauer [15].

The adsorption capacity was determined by adding a known mass of hydrated resin, centrifuged at 5000 rpm for 20 min in a microfiltration tube to remove extraparticle water, to vials containing 1.5 ml of solutions with different initial protein concentration. The vials were then sealed and rotated end-over-end at a low rpm for 24 h. The protein concentration in the supernatant was then analyzed with a Nanovue spectrophotometer (GE Healthcare, Piscataway, NJ) at 280 nm and the adsorbed protein concentration was calculated by material balance. The density of the hydrated particles, determined with a picnometer to be 1.064 g/ml, was used to convert the amount of protein adsorbed from a mass basis to units of mg per ml of hydrated particle volume.

Confocal laser scanning microscopy (CLSM) was used to determine the intraparticle concentration profiles of adsorbed IgG, Tg, and VLPs. Rhodamine Red™-X dye obtained from Invitrogen Corporation (Carlsbad, CA) was used to fluorescently label each sample following the supplier instructions. IgG and Tg were incubated in a pH 8.5 sodium bicarbonate buffer with a dye-to-protein molar ratio of 3:1 for 1 h at room temperature in the dark. After reaction, unreacted dye was separated by size exclusion chromatography using an Econo-Pac 10 DG desalting column from Bio-Rad Laboratories (Hercules, CA). Average labeling ratios of 0.21 and 0.59 were obtained for IgG and Tg respectively. Linear gradient elution chromatography on a 1 mL POROS HS 50 column at pH 5.0 showed virtually the same retention for labeled and unlabeled protein for both IgG and Tg, indicating that labeling did not significantly affect interactions with the resin. A similar procedure was used to label the VLPs. In this case, a 1:1 dye to protein ratio was

used based on the L1 protein content of the VLP sample, determined from its UV absorbance. Labeling was allowed to proceed for 1 hour in the dark at either room temperature or 4 °C. Ethanolamine was then added to quench the reaction. The mixture was then buffer-exchanged into the binding buffer consisting of 200 mM MOPS and 250 mM citrate at pH 7.0. Since a 10 kDa MWCO ultrafiltration membrane was used, any free dye (MW 768) was removed in this step. The final VLP concentration was between 0.2 and 0.3 mg/mL, expressed as L1 protein. The degree of labeling obtained at 4 °C was 0.13 mol dye/mol of L1 protein. Based on DLS analyses, there was no significant change in the VLPs sample during labeling and buffer exchange.

CLSM was performed with a Zeiss LSM 510 microscope with a Plan-Apochromat 63×/1.4NA oil objective (Carl Zeiss MicroImaging, LLC, Thornwood, New York, NY). Since the POROS 50HS particles are opaque in aqueous solution, the emitted fluorescence can hardly be observed. This problem was overcome by allowing adsorption to take place for a period of time and then immediately immersing the particles in benzyl alcohol, whose refractive index, n = 1.54 [17], appears to match, approximately, the refractive index of the backbone of the POROS HS 50 particles.

Actual CLSM measurements were made both batch-wise and under flow condition. Batch CLSM experiments were done by placing POROS HS 50 particles in vials containing 15 mL of each labeled protein diluted with sufficient unlabeled protein to yield a final dye-to-protein ratio of 1:40, and rotated end-over-end on a rotator. At periodic time intervals, small samples were removed from the vials and rapidly centrifuged at 13,000 rpm for 30 s to separate the particles from the supernatant. The particles were then immersed in benzyl alcohol and observed by CLSM.

CLSM experiments under flow conditions were conducted in a flow cell similar to the one described by Tao et al. [18] and shown in Fig. 2.2. The cell was constructed using a quartz capillary (obtained from Polymicro Technologies, Phoenix, AZ) with a 75 μm inner square section, thinned out slightly at one end to retain the POROS HS 50 particle in the lumen. Two syringe pumps (Model 11 Plus, Harvard Apparatus (Holliston, MA) and a 4-way valve (Valco Instruments Co. Inc., Houston, TX) were used to supply alternating flows of protein solution and benzyl alcohol. A single, particle loaded capillary could be used for IgG as exposure to benzyl alcohol did not appear to affect the protein adsorbed. However, in the case of Tg and the VLPs, some aggregates were formed when flow was switched from the protein solution to benzyl alcohol, thereby blocking the flow cell. As a result, multiple capillaries were used; each exposed to benzyl alcohol after protein adsorption only once and discarded after imaging.

Because of the different binding capacities of IgG, Tg, and the VLPs, the laser intensity was adjusted for each experiment to optimize CLSM performance and avoid saturating the photomultiplier tube detector. Optical sections were collected in 2 μm z-increments and analyzed using LSM Image Examiner software (Carl Zeiss MicroImaging, LLC, Thornwood, New York, NY).

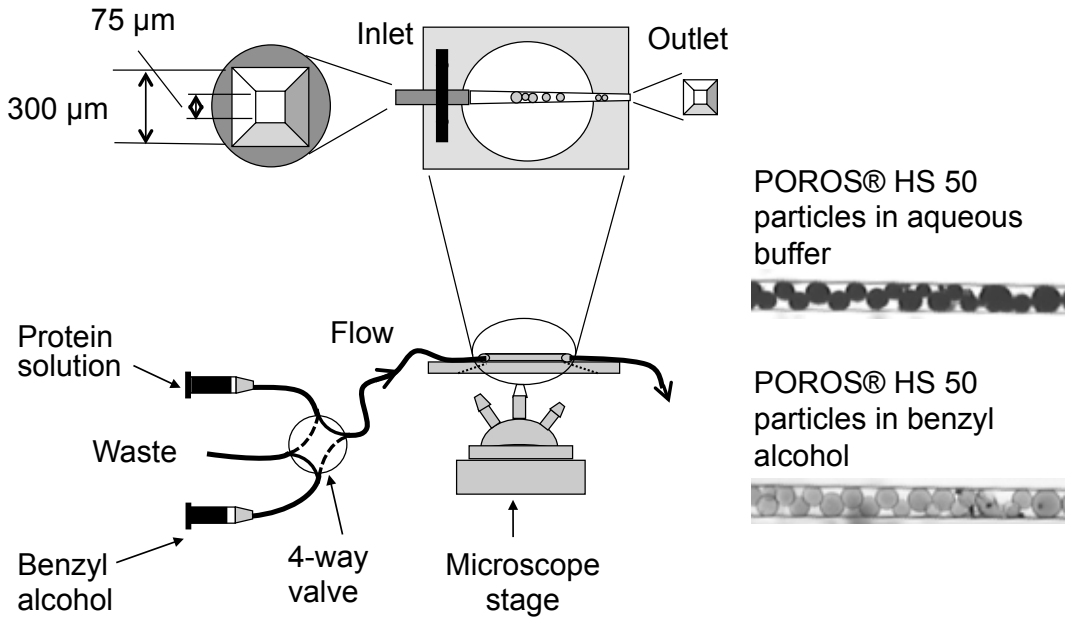

Figure 2.2. Flow cell used to obtain CLSM images of protein and VLPs adsorbed under flow conditions.

Fluorescently-labeled latex particles were used to determine if the results obtained for the VLPs can be generalized to other nanoparticles with similar size. For this purpose, amine-modified polystyrene latex particles with nominal mean diameter of 50 nm were obtained from Sigma-Aldrich (Catalog No. L0780, St. Louis, MO). These latex particles were pre-labeled with a blue fluorescent dye with maximum excitation and emission wavelengths at 360 nm and 420 nm, respectively. Because of the amine groups, they are positively charged and are expected to bind strongly to POROS HS 50. The nanoparticles were used both as received and after further labeling them with Rhodamine-red, in order to enhance their fluorescence.

Dynamic light scattering (DLS) was used to determine if aggregation of the nanoparticles occurred during fluorescent labeling and during the adsorption process. A

summary of z-average radii is given in Table 2.2. The results indicate there is no significant change in nanoparticle size and, thus, no aggregation.

Table 2.2. Summary of size measurement of latex nanoparticles

Sample	z-average radius, r_s, nm
Before fluorescent labeling	50.3 ± 1.3
After labeling, before mixing with POROS 50HS	51.4 ± 0.6
After mixing with POROS 50HS overnight	49.2 ± 0.9

To exclude the possibility that labeling affected VLP adsorption, a post-labeling method was also used. CLSM images were obtained by first mixing the POROS HS 50 particles with the VLPs solution, followed by the labeling process of the adsorbed VLPs with Dylight 488 using a Lightning-Link® Rapid kit obtained from Innova Biosciences (Babraham, Cambridge, UK). This reactive dye has maximum excitation and emission wavelengths at 493 nm and 518 nm, respectively and is coupled at pH 7 for the same conditions under which the VLPs are adsorbed. After mixing the resin particles with VLPs solution for a certain time, the resin sample was filter centrifuged to remove excess supernatant and the resin particles were resuspend in binding buffer. A "pH modifier" was added into the resin particle slurry to adjust pH and the mixture was pipetted into the vial containing the lyophilized dye powder followed by incubating for 30 sec. A "quencher" from the kit was then added to stop the reaction. The mixture was washed with the binding buffer by filter centrifugation and immersed in benzyl alcohol to match the refractive index of POROS HS 50 particles before observed using CLSM.

2.3 Results and Discussion

2.3.1 POROS HS 50 Resin Structures

Representative microphotographs and particle size distribution of POROS HS 50 sample for Lot 250-406 are shown in Fig. 2.3a and b, respectively. The average particle diameter was determined to be 52 μm with a range of sizes from 35 to 75 μm based on microphotographs of the hydrated beads. The average particle size and standard deviation for all six lots is summarized in Table 2.3. The results show that the lot-to-lot variations in average size are relatively large, going from a minimum of 40 μm to a maximum of 52 μm. However, the breadth of the particle size distribution is similar for the different lots as demonstrated by fairly consistent values of $\sigma_p / \bar{d}_p$.

Table 2.3. Average particle size and standard deviation for POROS HS 50 samples.

Lot No.	384	389	401	406	411	416
$\bar{d}_p$ (μm)	43	42	42	52	48	40
σ_p (μm)	9	8	8	12	12	7
$\sigma_p / \bar{d}_p$	0.21	0.19	0.19	0.23	0.25	0.18

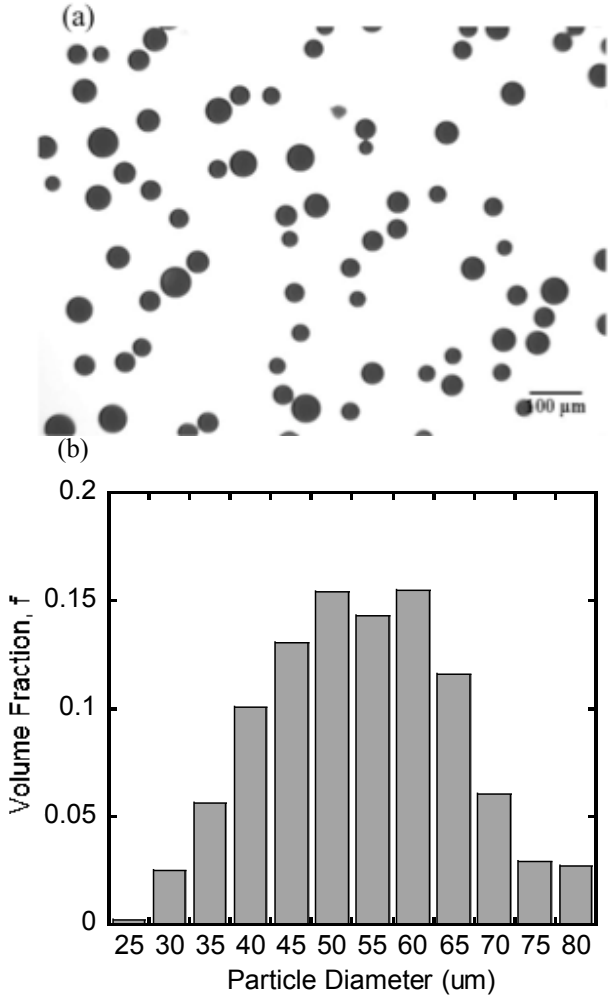

Figure 2.3. (a) Representative microphotographs of POROS HS 50 sample at 100 X magnification; (b) Particle size distributions for POROS HS 50 sample.

Figure 2.4 shows representative TEMs. Lighter, homogeneously gray areas are the embedding LRWhite resin while darker areas are the POROS matrix. Some white areas are also visible and are artifacts caused by the sectioning process and/or incomplete infiltration of the embedding resin. At low magnification (Fig. 2.4a), the image shows a distribution of pore sizes with larger pores uniformly distributed across the particle radius along with many small pores. The edge of the particle appears to present pores open to the surroundings. At higher magnification (Fig. 2.4b), a heterogeneous structure is evident,

consisting of microgranules, 100-200 nm in diameter, agglomerated to form microparticle aggregates about 500 nm in diameter. These microparticle aggregates define large pores that span length scales between 100 and 500 nm. Obviously, the larger pores can readily accommodate proteins, but only a fraction of the larger ones appears to be able accommodate VLPs that are 100 nm in size, especially considering that bound VLPs can further constrict access.

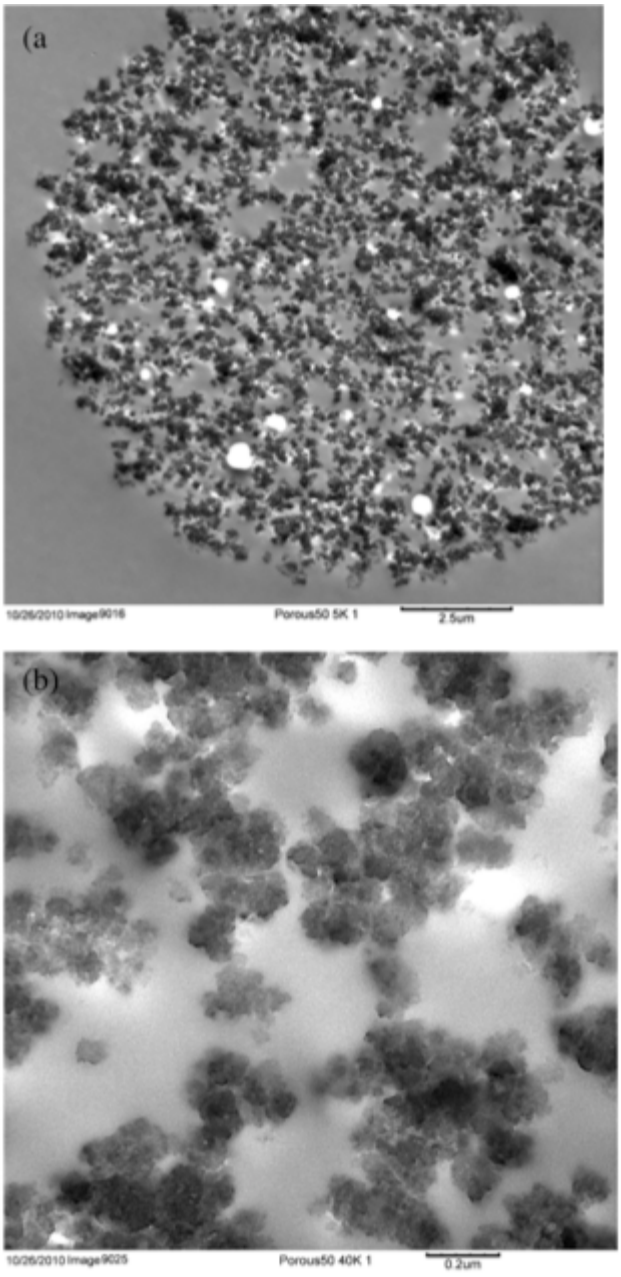

Figure 2.4. TEM images of sections of POROS HS 50 particles at (a) 5 K and (b) 40 K magnification. Scale bars are shown for reference in each image.

Inverse size exclusion chromatography (iSEC) was carried out to determine the accessible intraparticle volume and the apparent pore sizes using unbound probe molecules including glucose, dextran standards and probe proteins (Lyo, IgG, Tg and VLPs). Fig. 2.5 shows the representative elution peaks for dextrans and unretained proteins and VLPs. Vertical dashed lines correspond to the extraparticle void fraction obtained from a pressure-flow curve. As seen in Fig. 2.4a, glucose gains access to a large fraction of the particle volume, eluting at CV ~ 0.7. As the molecular mass increases, the dextran probes elute earlier and become more skewed since both steric exclusion and diffusional resistance increase. Similar results are seen in Fig. 2.4b for the proteins and the VLPs. Fig. 2.6 shows the distribution coefficient, K_D, calculated from the data in Fig. 2.5 as a function of each solute hydrodynamic radius, r_s. As seen in this figure, both dextran and protein data follow the same trends although somewhat higher K_D values are obtained for the dextran probes. In both cases, however, K_D decreases rapidly as r_s increases for low r_s-values, but then declines much more gradually for $r_s > 10$ nm. An approximate description of this trend is obtained by assuming a bimodal distribution of pore sizes with macropores and micropores of radius $r_{pore,M}$ and $r_{pore,m}$, respectively [16, 19]. Accordingly, the distribution coefficient is given by:

$$K_D = \varepsilon_M K_{D,M} + (1 - \varepsilon_M)\varepsilon_m K_{D,m} \tag{2.5}$$

where ε_M and ε_m are the macropore and micropore porosities, respectively, and

$$K_{D,M} = \left(1 - \frac{r_s}{r_{pore,M}}\right)^2 \tag{2.6}$$

$$K_{D,m} = \left(1 - \frac{r_s}{r_{pore,m}}\right)^2 \tag{2.7}$$

are the distribution coefficients for partitioning in the macropores and microprores, respectively. Values of $r_{pore,M}$ = 470 ± 10 nm, $r_{pore,m}$ =11 ± 4 nm, ε_M =0.32 ± 0.01 and ε_m =0.41 ± 0.01 were determined by fitting eqs. 2.5-2.7 to the dextran data, subject to the constraint that the total intraparticle porosity, $\varepsilon_p = \varepsilon_M + (1 - \varepsilon_M)\varepsilon_m$, equals the value determined for glucose of 0.60 ± 0.1. Despite the significant regression uncertainty, the fitted parameters appear to be consistent with the resin's structure seen by TEM (Fig. 2.4). According to these results, Lyo and IgG, whose hydrodynamic radii r_s are 2.3 and 5.5 nm, respectively, should easily gain access to both macropores and micropores, Tg, whose r_s is 8.5 nm, should be nearly completely excluded from the micropores, and the VLPs, whose r_s is around 50 nm should be completely excluded from the micropores.

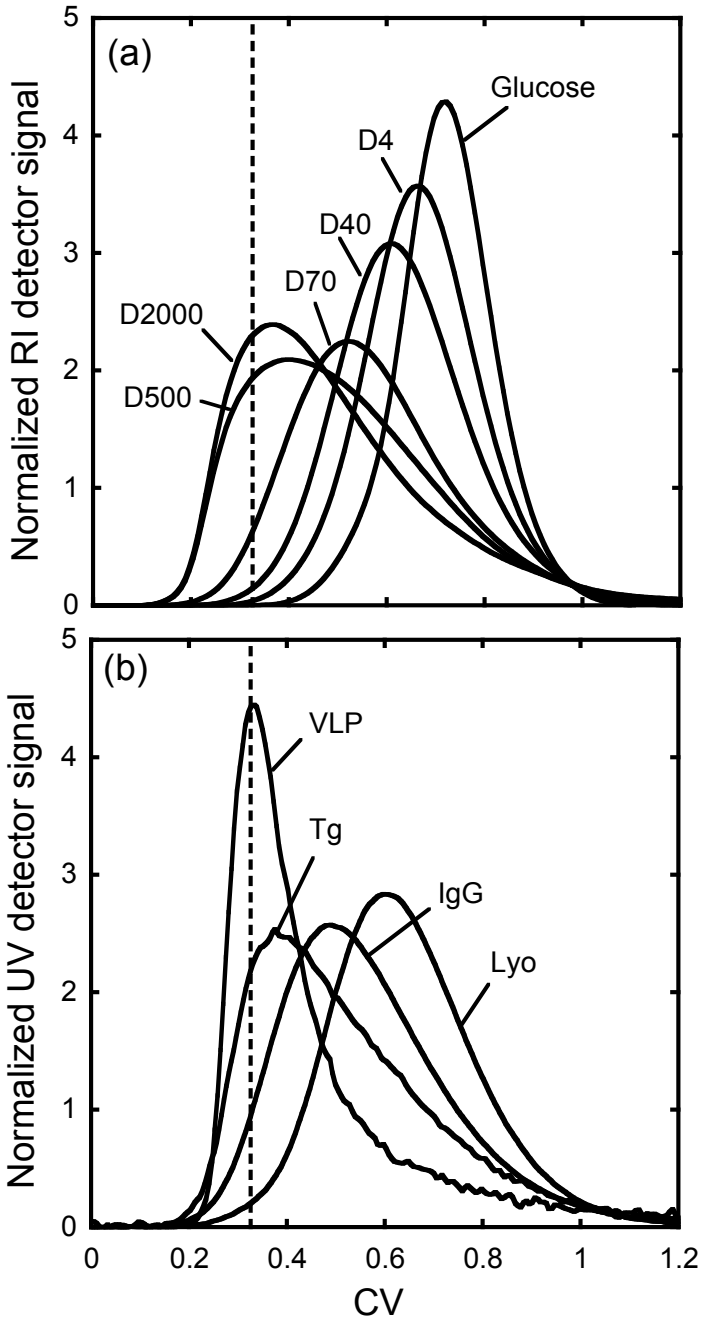

Figure 2.5. Chromatograms obtained for pulse injections of (a) dextrans and (b) proteins under non-binding conditions. Column length = 5 cm, mobile phase velocity = 150 cm/h.

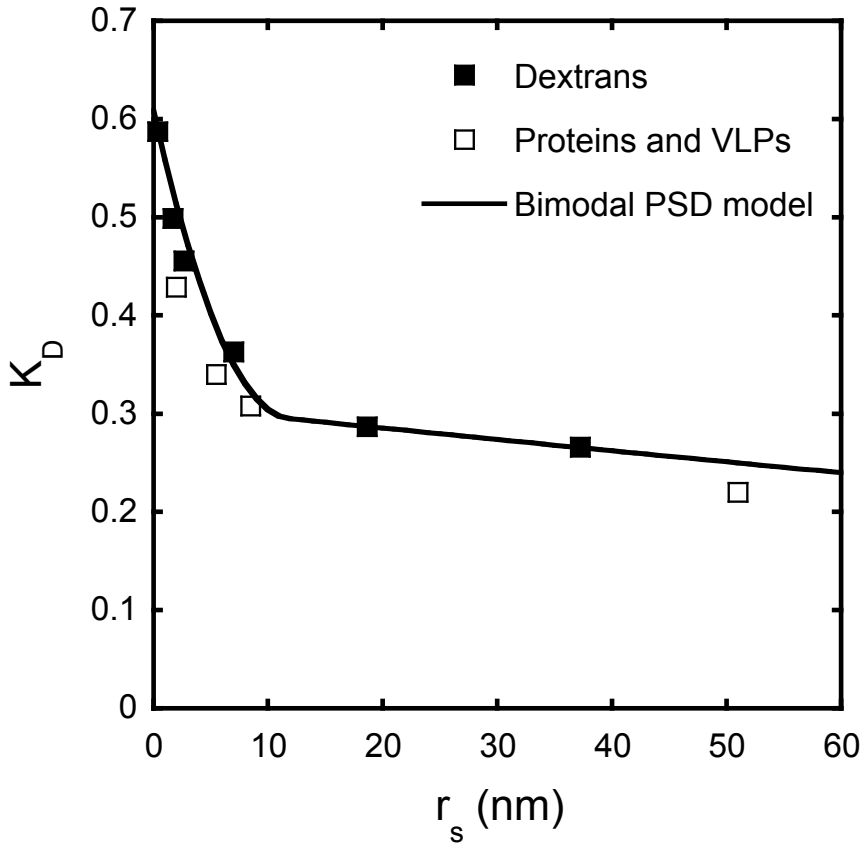

Figure 2.6. K_D versus hydrodynamic radius (r_s) of dextran standards, proteins and VLPs for non-binding conditions. The line is based on a bimodal pore size distribution (PSD) model (eq. 2.5).

2.3.2 HETP for Non-binding Conditions

Figure 2.7 shows the reduced HETP (h=HETP/d_p) versus reduced velocity (v' = vd_p/D_0) obtained for non-binding conditions for Lyo, IgG, Tg, and the VLPs. The data actually span mobile phase velocities between 60 and 1200 cm/h, but, for each solute, they are shifted toward higher v' values as molecular size increases and D_0 decreases. For Lyo the data follow a straight line, indicating complete dominance of diffusion. A linear relationship is also closely approximated by the IgG data, although a slight curvature is seen at the higher v'-values. A distinct plateau is however seen for both Tg and the VLPs, indicating that their transport becomes dominated by convection. The transition between diffusion and convection- limited mechanism occurs at $v' \sim$ 10,000 for Tg and around 20,000 for the VLPs. The plateau h -values for these species are about 200 and 250, respectively. Since d_p = 52 μm, these values correspond to HETPs on the order of 1 cm. This large value suggests that despite the apparent perfusion effect, suggested by the constant h at high v', the chromatographic efficiency of POROS HS 50 is low at high mobile phase velocities.

The generalized van Deemter relationship obtained by Carta and Rodrigues, eq. 1.4 [20], was used in comparison with the experimental data to determine the best fitting values of τ_M and F. A summary of these fitting parameters is shown in Table 2.4, along with the maximum value of $D_e/\widetilde{D}_e$ and the estimated values of $\left[(b-1)/b^2\right](\tau_m/\tau_M)(r_m/r_p)^2$ based on τ_m= 2 and r_m= 0.25 μm. Since, as seen from these values, $\left(D_e/\widetilde{D}_e\right) >> \left[(b-1)/b^2\right](\tau_m/\tau_M)(r_m/r_p)^2$, the micropores diffusional resistance is predicted to be indeed negligible for these conditions. Thus, eq. 1.4 reduces to the following equation:

$$h = \frac{HETP}{d_p} = a + \frac{1}{30}\frac{\varepsilon}{1-\varepsilon}\left(\frac{k'}{1+k'}\right)^2 \frac{\tau_M}{\varepsilon_M K_{D,M}}\frac{D_e}{\widetilde{D}_e} v' \qquad (2.8)$$

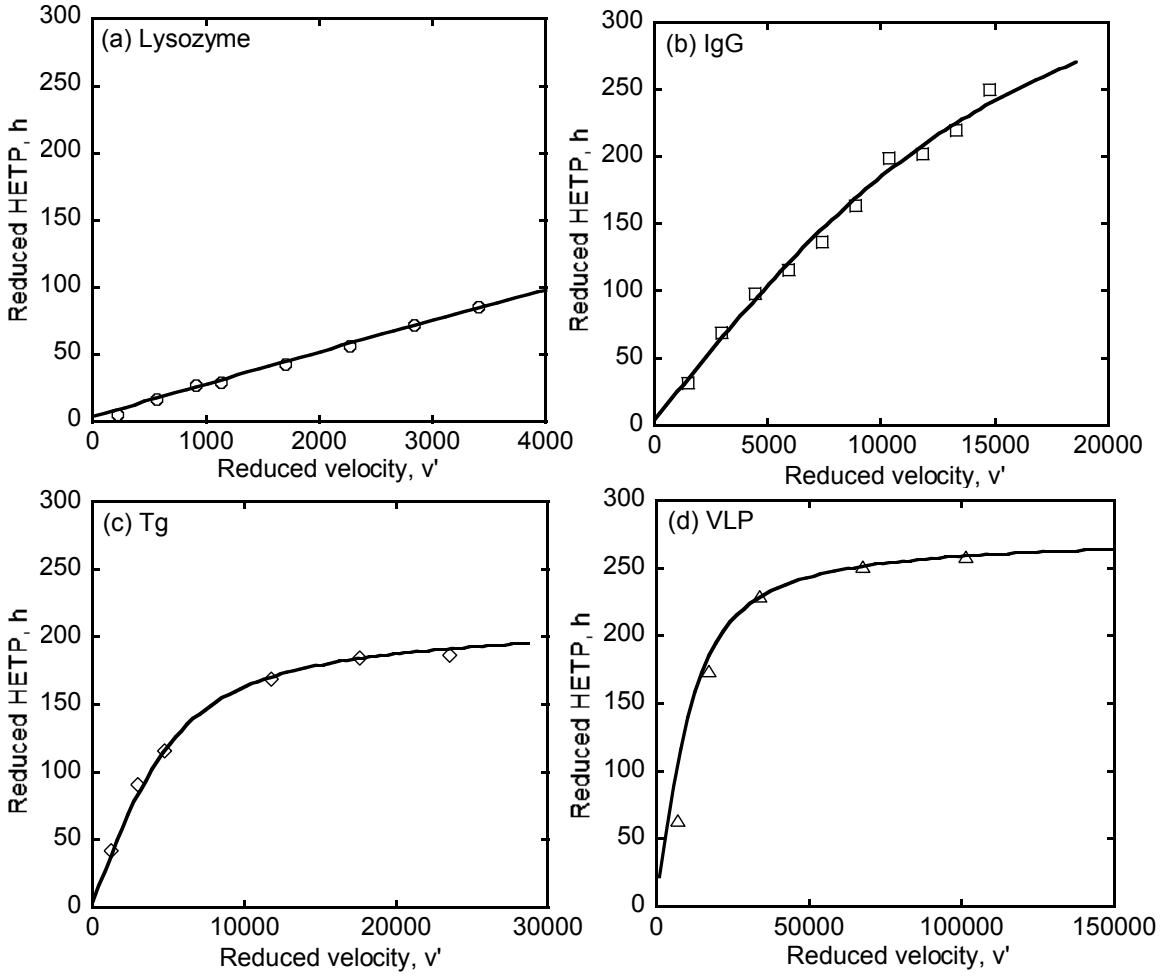

Figure 2.7. Reduced HETP vs. reduced velocity for non-binding conditions. D_0-values used to calculate *v'* are 1.1×10^{-6}, 4.0×10^{-7}, 2.6×10^{-7}, and 3.5×10^{-8} cm^2/s for Lyo (a), IgG (b), Tg (c), and VLPs (d), respectively, spanning mobile phase velocities between 60 and 1200 cm/h. Lines are based on eq. 10 with parameters from Table 2.4.

Figure 2.7 shows good agreement between calculated and experimental curves using these parameters. Since the different probes cover different ranges of conditions, the degree of correlation among the fitted parameters is very small. The τ_M values are typical for porous media. For Lyo, perfusion is negligible, because of its high D_0. Diffusion in the microparticle pores is also very fast since Lyo diffuses freely in the 11 nm radius micropores and the microparticles are very small. Thus, only τ_M and a are relevant. For IgG, diffusion is also dominant, as the HETP increases linearly with flow rate. Diffusion in the microparticle pores is still fast. The VLPs are completely excluded from the microparticle pores. Thus, the only relevant parameters are τ_M and F. The value of a determined for Lyo was used for all probes. Finally, for Tg, diffusion in the microparticle pores is likely to be severely hindered because of its size (8.5 nm radius) is close to that of the micropores (11 nm). Thus, τ_M is relevant and F becomes important at high flow rates.

Table 2.4. Parameters for perfusion model based on eq. 1.4 based on $a = 4$.

Solute	τ_M	F	$\left(D_e/\widetilde{D}_e\right)_{max}$ [(a)]	$\frac{b-1}{b^2}\frac{\tau_m}{\tau_M}\left(\frac{r_m}{r_p}\right)^2$ [(b)]
Lyo	1.9	No effect	0.96	2.3×10^{-5}
IgG	2.1	0.00050	0.76	1.3×10^{-5}
Tg	3.4	0.00082	0.27	0.23×10^{-5}
VLPs	2.0	0.00058	0.12	0

(a) at 1,200 cm/h

(b) based on $\tau_m = 2$, $r_m = 0.25$ μm

2.3.3 Protein Adsorption

Figure 2.8 shows the adsorption isotherms of IgG and Tg. The adsorption isotherms are highly favorable for both proteins. The maximum binding capacity was determined to be 150 ± 10 and 100 ± 10 mg/mL of particle volume for IgG and Tg, respectively. The CLSM images in Fig. 2.9 and 2.10 show the progress of adsorption of these two proteins over time under both no-flow and flow conditions. Fairly sharp fronts can be observed for both no-flow (top) and high-flow (bottom) conditions. In the case of IgG (Fig. 2.9), the adsorption front is circular under both conditions. However, Tg shows a circular adsorption front for the batch experiments only, while a noncircular front is clearly seen under flow conditions (Fig. 2.10). The intraparticle Peclet number for these experiments can be estimated based on the previous HETP measurements conducted under non-binding conditions, although the condition in the capillary is not exactly the same as in columns due to the different packing densities. At 1,000 cm/h, the parameters in Table 2.4 yield $Pe_{intra} = 1.9$ and 8.2 for IgG and Tg, respectively, which, based on eq.

1.3, give the corresponding values of $\tilde{D}_e / D_e$ of 1.2 and 3.1, respectively. This estimation predicts, as seen experimentally, that the effect of perfusion would be very small for IgG (~20% improvement in transport) but significant for Tg (~300% improvement in transport).

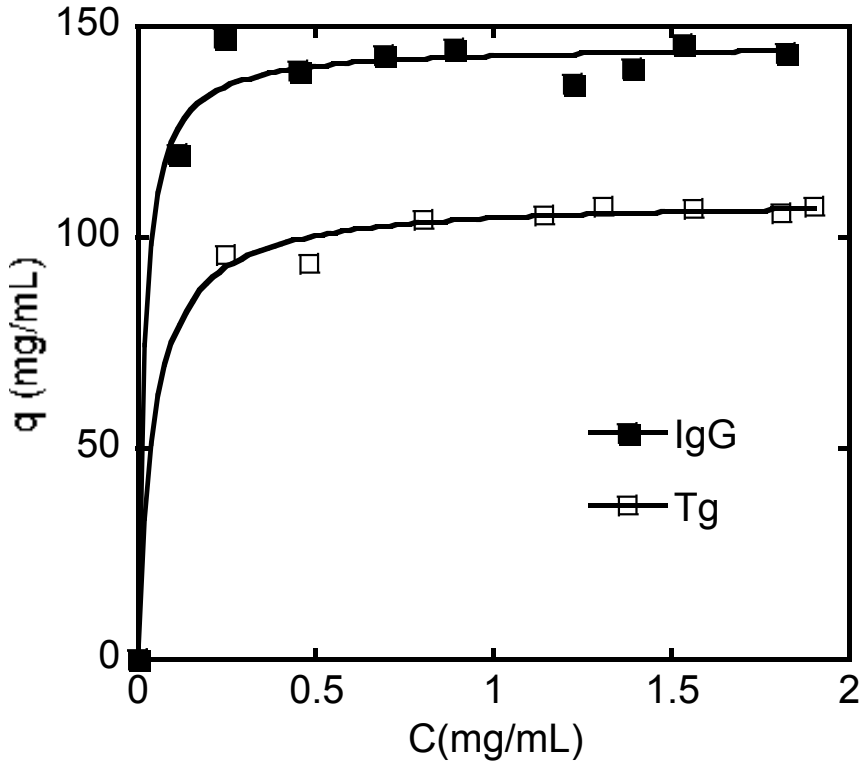

Figure 2.8. Adsorption isotherms for IgG and Tg in 20 mM acetate buffer at pH 5. Lines are the Langmuir isotherm $q = q_m KC/(1 + KC)$ where K is the equilibrium constant.

(a) Batch adsorption of 2 mg/mL IgG

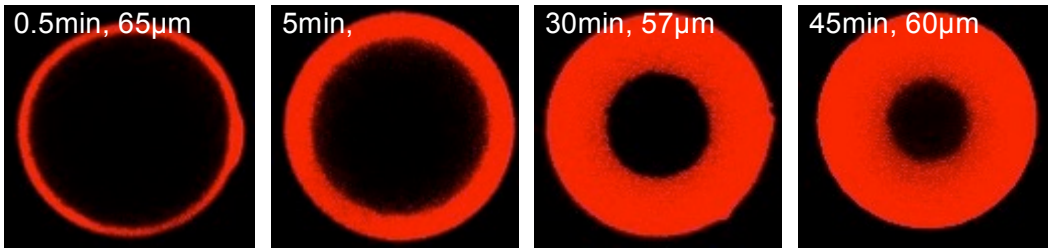

(b) Adsorption of 1 mg/mL IgG in flow cell at 1000 cm/h

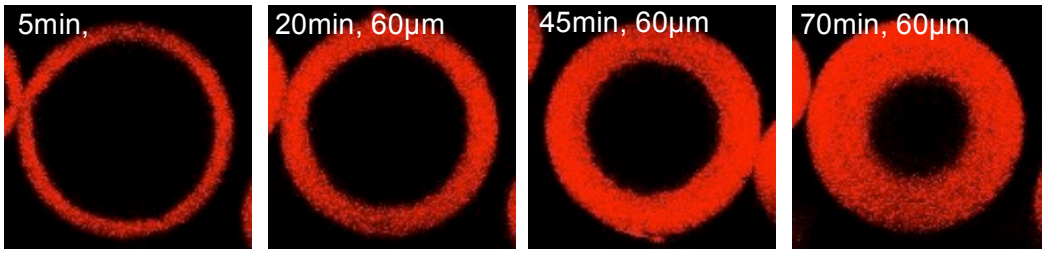

Figure 2.9. Representative equatorial CLSM images for (a) batch adsorption of 2 mg/mL IgG and (b) adsorption of 1 mg/mL IgG in the flow cell at 1000 cm/h. Different particles with diameter shown were imaged in (a). The same particle was imaged in (b) with flow direction from left to right.

(a) Batch adsorption of 2 mg/mL Tg

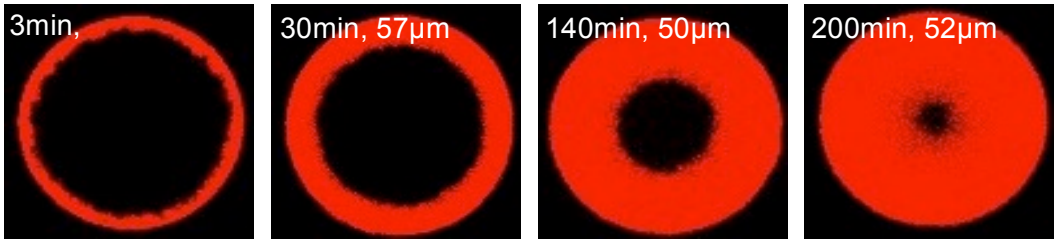

(b) Adsorption of 2 mg/mL Tg in flow cell at 1000 cm/h

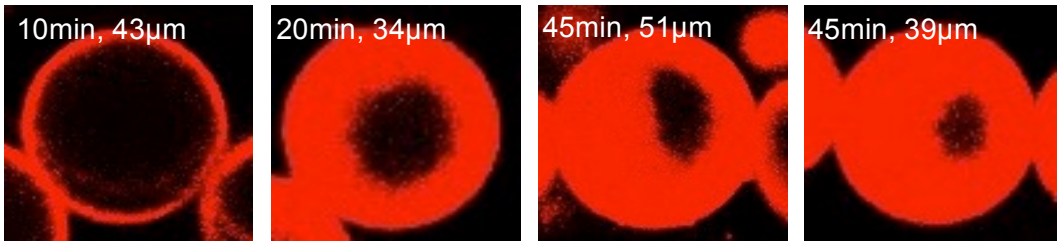

Figure 2.10. Representative equatorial CLSM images for (a) batch adsorption of 2 mg/mL Tg and (b) adsorption of 2 mg/mL Tg in the flow cell at 1000 cm/h. Different particles with diameter shown were imaged in (a) and (b). In (b) the flow direction is from left to right**.**

For the batch adsorption case, the adsorption kinetics is apparently consistent with the classical shrinking core model for both IgG and Tg. Accordingly, the normalized position of the adsorption front in the particle, $\rho_{sat} = r_{sat} / r_p$, is related to time by the following equation [21]:

$$f(\rho_{sat}) = 2\rho_{sat}^3 - 3\rho_{sat}^2 + 1 = \frac{6D_e C_0}{q_m r_p^2} t \tag{2.9}$$

where C_0 is protein solution concentration and q_m the binding capacity. Fig. 2.11 shows that the plots of $f(\rho_{sat})$ vs. $C_0 t / q_m r_p^2$ yield straight lines for both IgG and Tg with corresponding effective pore diffusivities D_e = (2.5 ± 0.1) × 10^{-8} and (0.47 ± 0.06) × 10^{-8} cm^2/s, respectively. The IgG results obtained at 1,000 cm/h based on the average depth of penetration of the adsorption front is also shown in Fig. 2.11. Since the profiles show a small degree of asymmetry, the model cannot be applied rigorously for these conditions. However, the plot is still approximately linear and the corresponding effective pore diffusivity is (3.1 ± 0.1) × 10^{-8} cm^2/s, which is 24% higher than the value obtained in the batch experiment, consistent with predictions based on eq. 1.3 with the estimated Pe_{intra}=1.9.

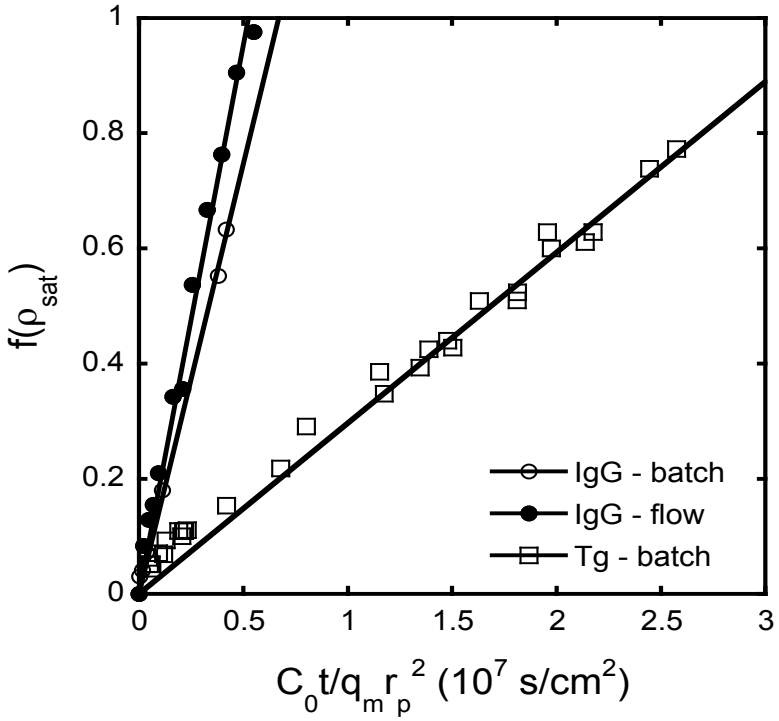

Figure 2.11. Dimensionless position of adsorption front vs. normalized time for IgG and Tg adsorption based on CLSM images of POROS HS 50 particles. IgG data are shown for both batch adsorption and for adsorption in the flow cell at 1,000 cm/h.

In the case of Tg adsorption at 1,000 cm/h, the highly noncircular intraparticle concentration profiles require a different analysis method. In this case, images were collected at different *z*-positions perpendicular to the field of view and to the direction of flow in 2 μm intervals. By determining for each section the percentage of area saturated with Tg, the fractional saturation of the particle was obtained, which was then calculated by averaging the particle diameter according to the following equation:

$$\frac{\bar{q}}{q_m} = \frac{3}{4r_p^3} \sum_i \phi_i r_{p,i}^2 \Delta z \qquad (2.10)$$

where ϕ_i is the fractional saturation for section i, $r_{p,i}$ is the section radius, and Δz the section thickness. ϕ_i was determined graphically by finding the contour of the fluorescent zone and determining the area within that contour as a fraction of the total area, using LSM Image Examiner software.

Fig. 2.12 shows representative *z*-stacks for Tg adsorption at 1,000 cm/h flow. The images show a decrease in fluorescence intensity from bottom (closer to the microscope objective lens) to top as a result of fluorescence attenuation effects. It is apparent that the pattern of adsorbed Tg also varies from bottom to top. The sections near the top and bottom (at low and high *z*-values) are almost uniformly fluorescent indicating complete saturation while sections near the particle center show asymmetrically distributed fluorescence that skew towards the direction of flow. These results, based on the assumption that the fluorescence signal is directly related to the protein bound, are consistent with the patterns predicted by the theoretical model of Liapis et al. for the convection-dominated case of high Pe_{intra} [12]. Fig. 2.13 shows the $\bar{q}/q_m$ values calculated from eq. 2.10 for both batch and flow adsorption of Tg. The results are plotted to a time scale normalized by the square of the actual particle radius for the purpose of comparison. As seen in this figure, fast complete saturation of the particle is obtained under flow conditions if compared with batch experiment. The lines show predictions of the shrinking core, pore diffusion according to the following equation:

$$3 - 2\frac{\bar{q}}{q_m} - 3\left(1 - \frac{\bar{q}}{q_m}\right)^{\frac{2}{3}} = \frac{6D_e C_0 t}{q_m r_p^2} \qquad (2.11)$$

which is consistent with eq. 2.9. The line for the batch case is shown for $D_e = 0.47 \times 10^{-8}$ cm^2/s, which is determined from the linearized fit in Fig. 2.11. The same equation is also used to the flow data with an effective diffusivity 1.5×10^{-8} cm^2/s. Although, the fit to the flow data is only approximate, this fitted diffusivity provides an estimate of the convection-enhanced diffusivity. For these conditions we obtained $\tilde{D}_e / D_e$ ~1.5/0.47=3.2, which agrees well with the value predicted based of the value of F estimated from the HETP data.

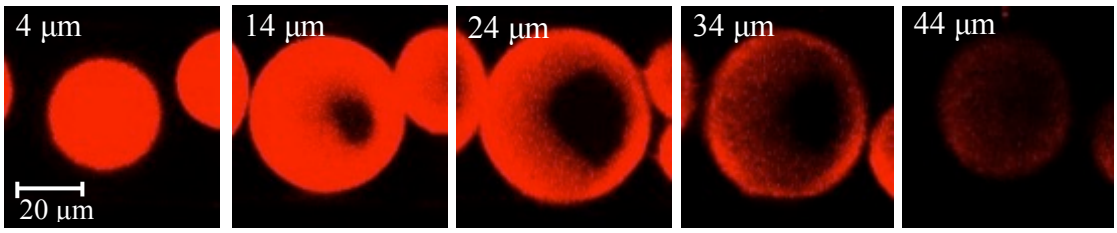

Figure 2.12. Representative CLSM images of 2 mg/mL Tg adsorption in a 54 μm diameter particle in the flow cell at 1000 cm/h. Optical sections are shown at different vertical distances to the bottom of the particle perpendicular to the field of view as indicated. Flow is from left to right.

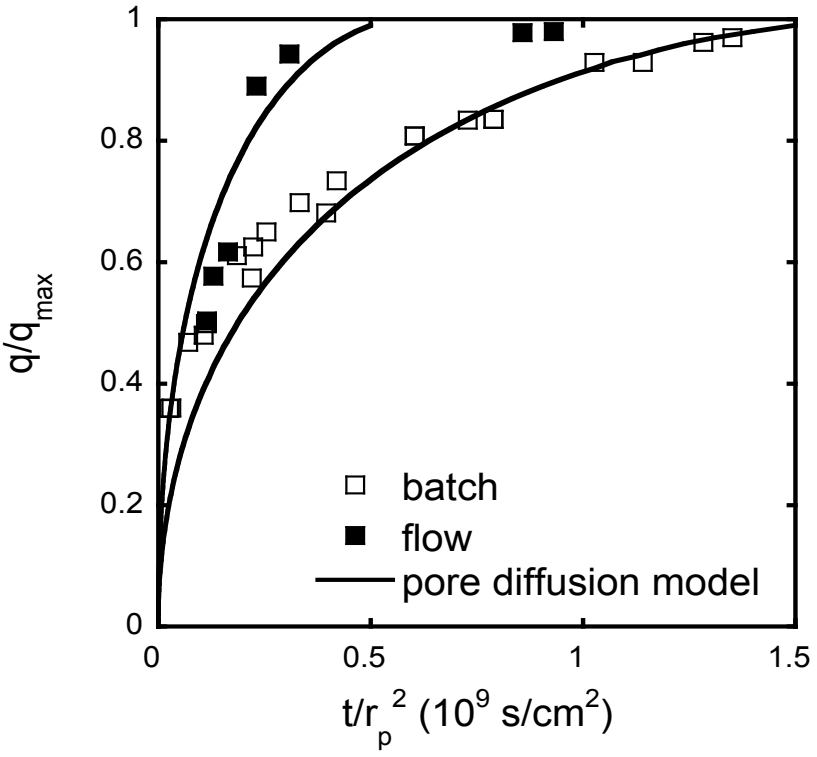

Figure 2.13. Adsorption kinetics of 2 mg/mL Tg determined by CLSM under batch (no-flow) adsorption conditions and in the flow cell at 1,000 cm/h. Lines are based on the pore diffusion model as discussed in the text.

2.3.4 VLP Adsorption

Figure 2.14 shows CLSM images for the adsorption of VLPs on POROS HS 50 particles in both batch (top) and flow conditions (bottom). It is clear that in both cases, the adsorption of VLP is confined to a thin shell, 1 to 2 μm thick, on the outer surface of the POROS HS 50 beads. This behavior is highly possibly caused by the blocked access to

the through-pores by the bound VLPs. As seen in Fig. 2.4b, the clean resin contains pores that have dimensions in the 100 to 500 nm range. Since, based on DLS measurements that VLPs have r_s = 50 nm, which gives about 100 nm in size, it is perhaps not surprising that access to the underlying pore network is largely precluded by a small amount of VLPs adsorbed at the particle outer surface.

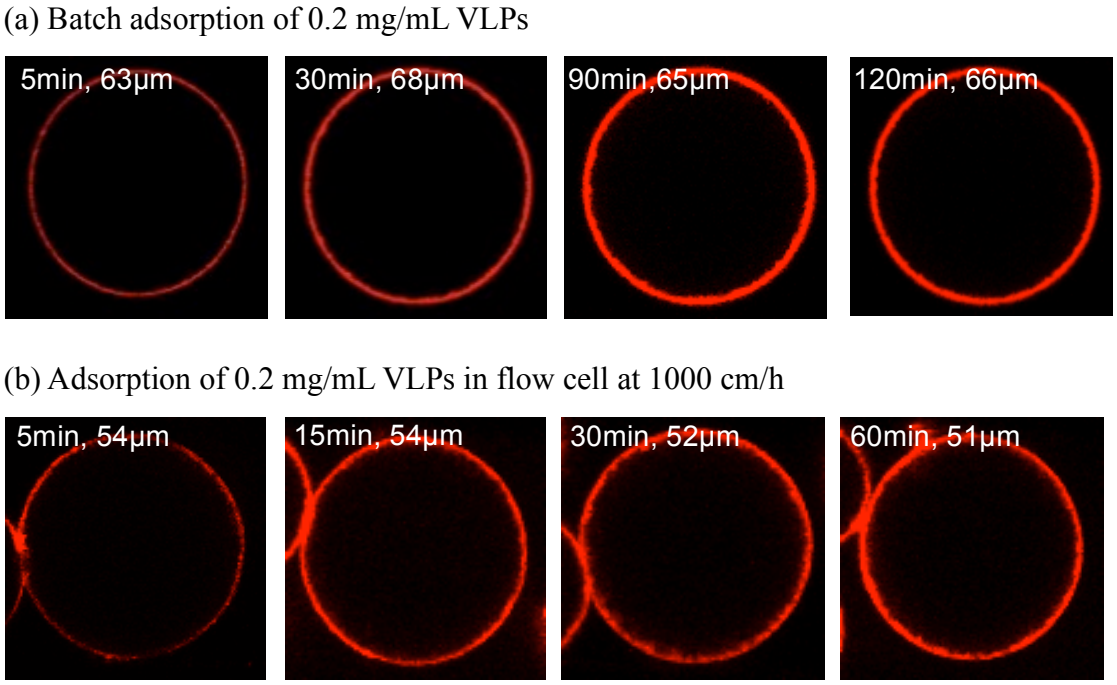

Figure 2.14. Representative equatorial CLSM images for (a) batch adsorption of 0.2 mg/mL VLPs and (b) adsorption of 0.2 mg/mL VLPs in the flow cell at 1,000 cm/h. Different particles with diameter shown were imaged in (a) and (b). In (b) the flow direction is from left to right.

The results of post-labeling CLSM experiment of VLPs are shown in Fig. 2.15. For comparison, the same post-labeling method was also used for IgG and, as a control, for virgin POROS HS 50 beads with no protein bound. All the proteins and VLP solutions

were prepared at pH 7 and the Dylight 488 labeling reactions were conducted after exposing POROS HS 50 beads in the solution for a certain time. The adsorption of IgG and VLPs was performed in batch mode, by adding an aliquot of resin particles to protein solutions and taking samples of the beads at different times. The results (Fig. 2.15) show that (1) the fluorescent tag does not react with POROS HS 50 (Fig. 2.15a); (2) IgG exhibits the same pattern of fluorescence as that seen with pre-labeled protein (Fig. 2.15b, c); and (3) VLP still has little penetration into the resin particle even after 2 hours (Fig. 2.15d), consistent with the results with pre-labeled VLPs. As a result, the effects of Rhodamine-red fluorescent labeling on the adsorption of VLPs on POROS HS 50 can be excluded and confirm that VLP binding is limited to a thin layer at the bead surface.

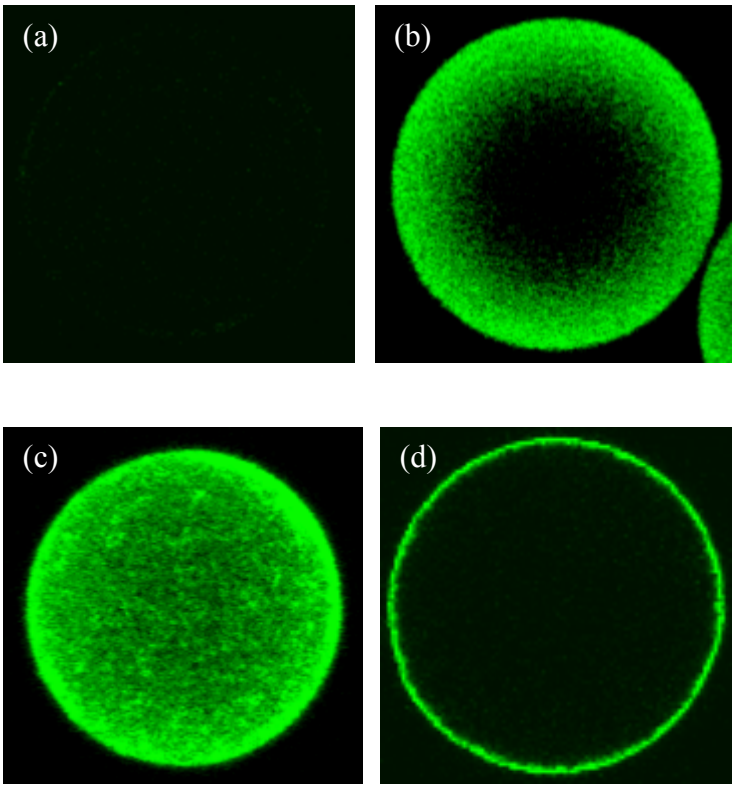

Figure 2.15. Representative equatorial CLSM images for batch adsorption on POROS HS 50 followed by post-labeling with Dylight 488 of (a) blank POROS HS 50 beads, (b) IgG adsorbed for 30 min, (c) IgG adsorbed for 120 min, and (d) VLPs adsorbed for 2 hours.

TEMs were obtained for particles that had been exposed to VLPs for 24 h under binding conditions to further confirm this hypothesis. Fig. 2.16 shows the results along with those for a clean particle. Comparing with the pores that are clearly open at the outer surface of the clean particle (Fig. 2.4b), the VLP-exposed bead shows a distinct layer blocking the pores is visible at the outer surface. Although the thickness of this layer is smaller than seen in the CLSM images, which was likely due to the dehydration and embedding process, the TEM provides clear evidence that the transport is hindered by bound VLPs. Trilisky and Lenhoff reached similar conclusion for the adsorption of adenovirus type 5 (Ad5) having an approximate diameter of 80 nm in PL-SAX 4000 A resins, whose pores are in the 400 nm range, based images obtained by cryo-scanning electron microscopy [22]. Together, these results suggest that matrices with even larger pores would be needed to accommodate VLPs or other bioparticles in this size range.

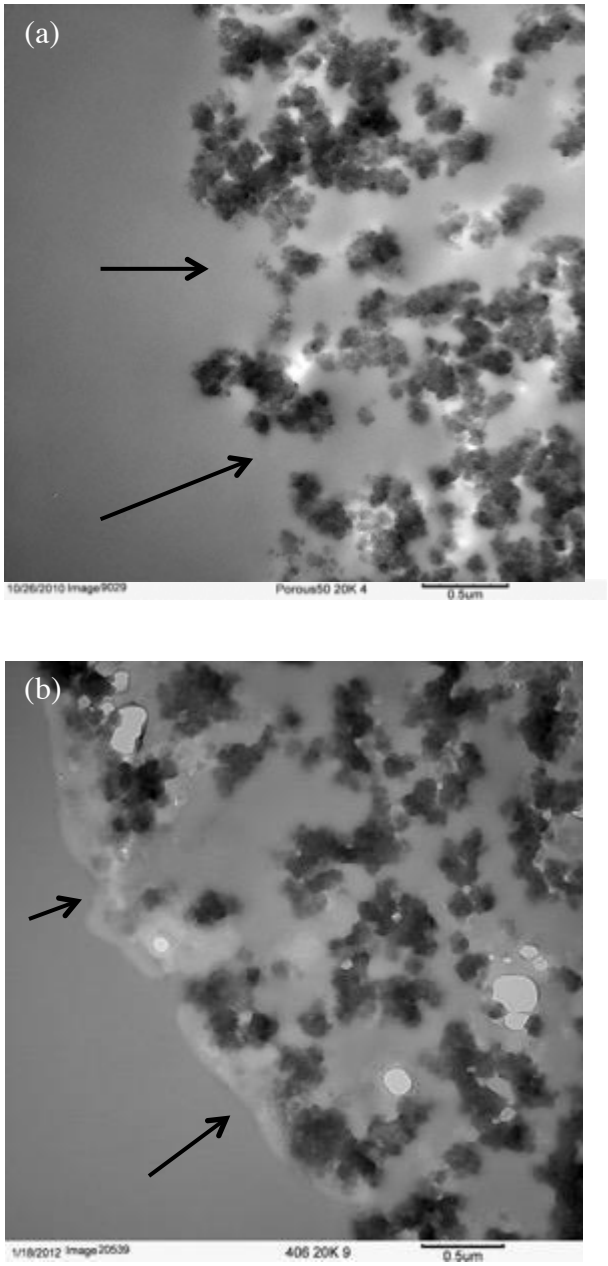

Figure 2.16. TEM images at 20K magnification of sections of (a) POROS HS 50 particles clean and (b) exposed to VLPs for 24 h. Arrows indicate open pores in (a) and pore occluded by an adsorbed layer in (b).

2.3.5 Adsorption of Latex Particles on POROS HS 50

Fluorescently-labeled latex particles were used to determine if the results obtained for the VLPs can be generalized to other nanoparticles with similar size. For this purpose, amine-modified polystyrene latex particles with nominal mean diameter of 50 nm were obtained from Sigma-Aldrich (Catalog No. L0780, St. Louis, MO). These latex particles were pre-labeled with a blue fluorescent dye with maximum excitation and emission wavelengths at 360 nm and 420 nm, respectively. Because of the amine groups, they are positively charged and are expected to bind strongly to POROS HS 50. The nanoparticles were used both as received and after labeling with Rhodamine-red, in order to enhance their fluorescence. The binding capacity was estimated by assuming monolayer coverage of the surface area associated with the resin's macropores across the entire beads using the following equation adapted from Etzel [23]:

$$\text{Monolayer binding capacity} = \frac{2\pi}{3\sqrt{3}} \rho_s r_s \tag{2.12}$$

where ρ_s is the nanoparticle density (~1.05 g/mL according to the supplier), and r_s is the nanoparticle radius. The surface area of the large pores was estimated from the total perimeter of the microgranules obtained from the TEM images of the sections of POROS HS 50 particles, which is around 1.4 m^2/mL beads. The resulting estimated binding capacity is about 44.4 mg/mL beads. Accordingly, based on the shrinking core model (eq. 2.9), assuming that they can diffuse into the resin beads, the time for saturating POROS HS 50 beads at 2 mg/mL nanoparticle concentration should be about 1.3 hours.

Adsorption experiments were carried out first with the latex nanoparticles as received. The particles were diluted in 10 mM Na_2HPO_4 buffer at pH 6, to ensure that the

amine group on the particle surface is positively charged, to a final solution concentration of 2 mg/mL. A small amount of POROS HS 50 particles (estimated capable of adsorbing less than 10% of the total latex particles), was added into the solution and mixed at room temperature. After a certain time, the sample was centrifuged to remove excess solution from the resin. The beads were then washed with the 10 mM phosphate buffer and resuspended in benzyl alcohol for the purpose of refractive index matching and observation with CLSM. Unfortunately, at the excitation wavelength needed, the resin backbone also fluoresced. Thus, the latex nanoparticles were labeled with Rhodamine-red. The labeling procedure was similar as that for VLPs that was described in section 4.1.3 but using a dye-to-latex nanoparticle molar ratio of 100:1.

In order to exclude the effects of autofluorescence from the resin backbone, Rhodamine-Red was used to label the latex particles and provide fluorescent emission at different wavelength.

CLSM images for Rhodamine Red labeled latex nanoparticles adsorption on POROS HS 50 beads are shown in Fig. 2.17a (1 h) and b (overnight) in comparison with the 1.5 h image of VLPs adsorption. The 1-hour adsorption of latex particles shows profiles similar to the 1.5-hour sample of VLPs adsorption, that the adsorbate molecules form a thin layer on the surface of POROS HS 50 particles. As seen from these images, at relatively short times the latex nanoparticle behavior is similar to that of the VLPs, with adsorption limited to a thin layer at the bead surface. The overnight sample of latex particles shows more penetration into the resin beads compared with the 1-hour sample, however the penetration is still very limited and the bulk of the binding surface area inside the resin bead is not utilized.

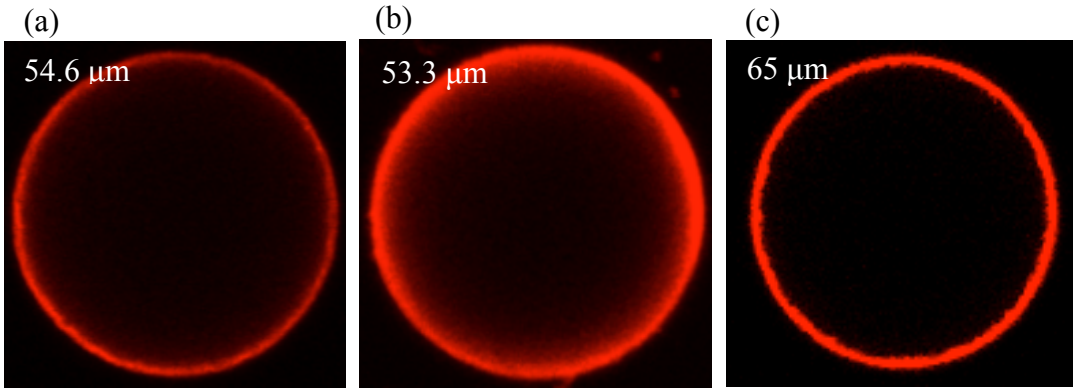

Figure 2.17. Representative equatorial CLSM images for batch adsorption of Rhodamine Red labeled 50 nm latex particles on POROS HS 50 after 1 h (a) and overnight (b). (c) shows the image of VLP adsorption on POROS HS 50 obtained previously (Fig. 2.14a) after 1 h of contact with the resin.

2.3.6 VLPs Desorption from POROS HS 50

Fig. 2.18 shows CLSM images of VLPs desorption from POROS HS 50 particles in both batch and high-flow conditions. POROS HS 50 particles had been equilibrated with a 0.3 mg/mL VLP solution for 24 h in the binding buffer (200 mM MOPS, 250 mM Sodium Citrate, pH 7.0). The particles were then immersed in the desorption buffer (50 mM MOPS, 1250 mM NaCl, 5 mM Na_3PO_4, pH 7.0). Similar behavior can be observed for both cases. Initially, the VLPs are confined to a thin layer on the adsorbent particles surface. Desorption of VLPs layer can be observed within 2 min of exposure to the desorption buffer. However, desorption is obviously incomplete and the accumulated layer on the external surface of the absorbent particle still persists after 60 minutes.

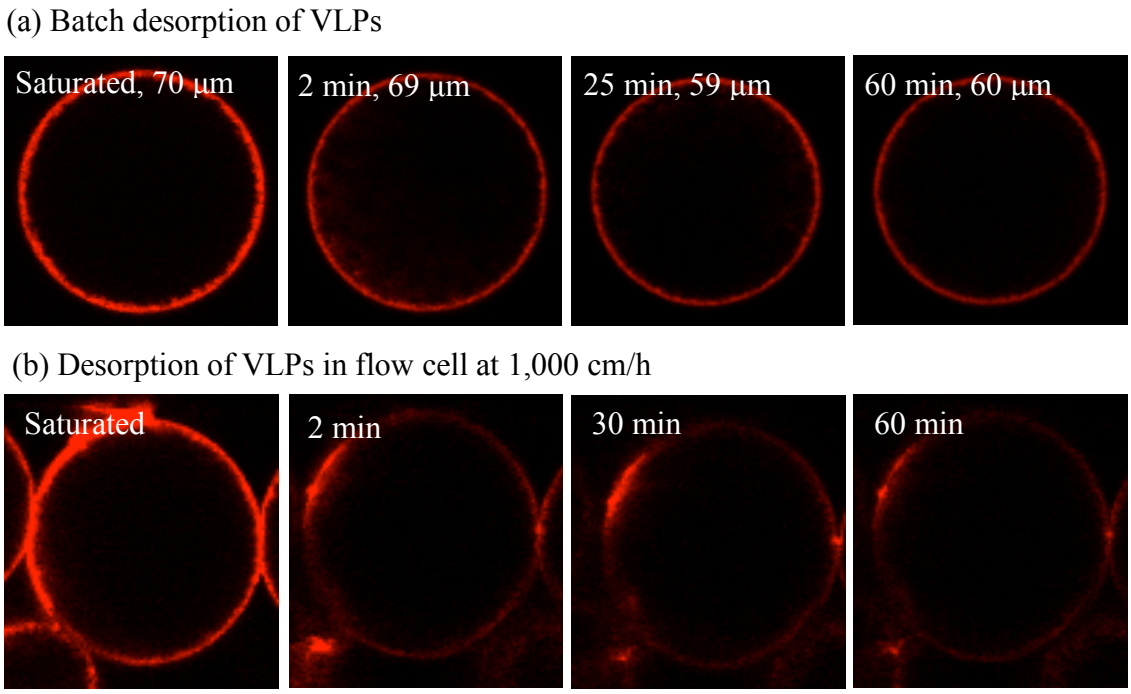

Figure 2.18. Representative equatorial CLSM images for VLP desorption under (a) batch experiments and (b) 1000 cm/h flow condition. Different particles with diameter shown were imaged in (a). In (b) the particle diameter is 48 µm and the flow direction is from left to right.

2.4 Conclusion

The resin used in this work, POROS HS 50, has a structure consistent with the description of perfusion chromatography: a bimodal distribution of pores including large open pores transecting a network of smaller pores present within microparticle aggregates around 500 nm in size. HETP measurements for model proteins (Lyo, IgG, Tg) and VLPs under non-binding conditions suggest that perfusion occurs with an intraparticle flow ratio F between 0.0005 and 0.0008. These small values indicate that for small proteins (e.g. Lyo), the effects of perfusion on chromatographic performance are negligible and only slight for larger proteins such as IgG even at 1000 cm/h flow velocity, shown as an approximately linear relationship in van Deemter plot. However, for very large proteins (e.g. Tg) and VLPs, the reduced HETP becomes independence of flow rate at higher reduced velocity, indicating the effects of perfusion become substantial or even dominant. Confocal microscopy images of protein adsorption under flow conditions also show different behaviors for model proteins and VLPs. The result of IgG shows fairly symmetrical intraparticle concentration profiles, which is consistent with classical shrinking core model, suggesting a pore diffusion controlled transport. For Tg, the intraparticle concentration profiles show asymmetry, skewing in the direction of flow, confirms the effects of perfusion for Tg under binding conditions. The profiles at 1000 cm/h, for conditions that correspond to intraparticle Peclet numbers around 8 are quantitatively consistent with the model of Liapis et al. [12] confirming its approximate validity for practical conditions. In the case of VLPs, which are even larger in size than Tg, the effects of perfusion seem to vanish since the binding only occurs exclusively in a thin layer at the particle surface. Similar behavior is also observed for fluorescently

labeled latex nanoparticles of similar size with VLPs. The possible effects of fluorescent labeling on VLPs adsorption is excluded by post-adsorption labeling experiments of VLPs. These results indicate that the bound VLPs block access to most through-pores preventing both diffusion and convection. The desorption of VLPs from POROS HS 50 particles shows an rapid initial desorption within 2 min, however, little further desorption occurs afterwards and remaining bound VLPs can still be observed even after 60 min.

2.5 List of Symbol

ε	extraparticle porosity
ε_M	macropore porosity
ε_m	micropore porosity
ε_p	intraparticle porosity
ϕ_i	fractional saturation for section i
ρ_s	nanoparticle density
ρ_{sat}	normalized position of the adsorption front in the particle
σ_p	standard deviation of the particle size distribution
τ_M	tortuosity factor in macroparticle pores
τ_m	tortuosity factor in microparticle pores
a	hydrodynamic dispersion factor
C	protein solution concentration (mg/mL)
C_0	initial protein solution concentration (mg/mL)

D_0 free solution diffusivity (cm^2/s)

D_e effective diffusivity (cm^2/s)

$\tilde{D}_e$ convection enhanced effective diffusivity (cm^2/s)

d_p particle diameter (cm)

$\bar{d}_p$ volume-average particle diameter (cm)

F ratio of intraparticle and extraparticle flow velocities

f_j volume fraction of particles of diameter $d_{p,j}$

$HETP$ height equivalent to the theoretical plate (cm)

h reduced HETP

K adsorption constant in Langmuir model (mL/g)

K_D distribution coefficient

$K_{D,M}$ size exclusion in the macroparticle pores

$K_{D,m}$ size exclusion in the microparticle pores

k' retention factor

k_f external mass transfer coefficient (cm/s)

L column length (cm)

P pressure (Pa)

Pe_{intra} intraparticle Peclet number

q adsorbed phase protein concentration (mg/mL)

q_m maximum adsorption capacity in Langmuir model (mg/mL)

$\bar{q}/q_m$ fractional saturation of the particle

r_m microsphere radius (nm)

r_p particle radius (μm)

$r_{pore,M}$ macropore radius (nm)

$r_{pore,m}$ micropore radius (nm)

r_s molecular radium (nm)

r_{sat} radius of adsorption front (μm)

t time (s)

u superficial velocity (cm/s)

V_{column} column volume (mL)

v fluid velocity (cm/s)

v' reduced velocity ($=vd_p/D_0$)

2.6 References

[1] Afeyan, N. B., Gordon, N. F., Mazsaroff, I., Varady, L., Fulton, S. P., Yang, Y. B., & Regnier, F. E. (1990). Flow-through particles for the high-performance liquid chromatographic separation of biomolecules: perfusion chromatography. *J. Chromatogr., 519*(1), 1-29.

[2] Cook, J. C., Joyce, J. G., George, H. a, Schultz, L. D., Hurni, W. M., Jansen, K. U., Hepler, R. W., et al. (1999). Purification of virus-like particles of recombinant human papillomavirus type 11 major capsid protein L1 from Saccharomyces cerevisiae. *Protein Express. Purif.*, *17*(3), 477-84.

[3] Chen, X. S., Garcea, R. L., Goldberg, I., Casini, G., Harrison, S. C. (2000). Structure of small virus-like particles assembled from the L1 protein of human papillomavirus 16. *Mol. cell*, *5*(3), 557-67.

[4] Mach, H., Volkin, D. B., Troutman, R. D., Wang, B., Luo, Z., Jansen, K. U., Shi, L. (2006). Disassembly and reassembly of yeast-derived recombinant human papillomavirus virus-like particles (HPV VLPs). *J. Pharm. Sci.*, *95*(10), 2195–2206.

[5] Shi, L., Sanyal, G., Ni, A., Luo, Z., Doshna, S., Wang, B., Graham, T. L., et al. (2005). Stabilization of human papillomavirus virus-like particles by non-ionic surfactants. *J. Pharm. Sci.*, *94*(7), 1538-51.

[6] McCoy, M., Kalghatgi, K., Regnier, F.E., Afeyan, N. (1996). Perfusion chromatography - Characterization of column packings for chromatography of proteins. *J. Chromatogr. A, 743*(1), 221-229.

[7] Carta, G., Gregory, M.E., Kirwan, D.J., Massaldi, H.A. (1992). Chromatography with permeable supports: Theory and comparison with experiments. *Sep. Technol., 2*(2), 62-72.

[8] Frey, D.D., Schweinheim, E., Horváth, C. (1993). Effect of intraparticle convection on the chromatography of biomacromolecules. *Biotechnol. Prog., 9*(3), 273-284.

[9] Rodrigues, A.E., Chenou, C., De La Rendueles Vega, M. (1996). Protein separation by liquid chromatography using permeable POROS Q/M particles. *Chem. Eng. J., 61*(3), 191-201.

[10] Weaver Jr., L.E., Carta, G. (1996). Protein adsorption on cation exchangers: Comparison of macroporous and gel-composite media. *Biotechnol. Prog., 12*(3), 342-355.

[11] Pfeiffer, J.F., Chen, J.C., Hsu, J.T. (1996). Permeability of Gigaporous Particles. *AIChE J., 42*(4), 932-939.

[12] Liapis, A.I., Xu, Y., Crosser, O.K., Tongta, A. (1995). "Perfusion chromatography". The effects of intra-particle convective velocity and microsphere size on column performance. *J. Chromatogr. A, 702*(1-2), 45-57.

[13] Pérez-Almodóvar, E., Tao, Y., Carta, G. (2011). Protein adsorption and transport in cation exchangers with a rigid backbone matrix with and without polymeric surface extenders. *Biotechnol. Prog. 27*(5), 1264-72.

[14] Tyn, M.T., Gusek, T.W. (1990). Prediction of diffusion coefficients of proteins. *Biotechnol. Bioeng., 35*(4), 327-338.

[15] Carta, G., Jungbauer, A. (2010) Protein Chromatography: Process Development and Scale-Up, Wiley-VCH, Weinheim, Germany.

[16] Hagel, L., Ostberg, M., Andersson, T. (1996). Apparent pore size distributions of chromatography media. J. Chromatogr. A, 743(1), 33-42.

[17] Wypych, G. (2012) Knovel Solvents – A Properties Database. ChemTec Publishing, New York, NY, USA.

[18] Tao, Y., Almodovar, E. X. P., Carta, G., Ferreira, G., & Robbins, D. (2011). Adsorption kinetics of deamidated antibody variants on macroporous and dextran-grafted cation exchangers. III. Microscopic studies. J. Chromatogr. A, 1218(44), 8027-35.

[19] Yao, Y., Lenhoff, A.M. (2004). Determination of pore size distributions of porous chromatographic adsorbents by inverse size-exclusion chromatography. *J. Chromatogr. A, 1037*(1-2), 273-282.

[20] Carta, G., Rodrigues, A.E. (1993). Diffusion and convection in chromatographic processes using permeable supports with a bidisperse pore structure. *Chem. Eng. Sci., 48*(23), 3927-3935.

[21] Ruthven, D.M. (1984) Principles of Adsorption and Adsorption Processes. Wiley, New York, NY, USA.

[22] Trilisky, E., Lenhoff, A., (2007). Sorption processes in ion-exchange chromatography of viruses. *J. Chromatogr. A, 1142*, 7-12.

[23] Etzel, M. R. Layered stacks, In Monolithic Materials; Preparation, Properties, and Allications, Svec, F., Tennikova, T. B., Deyl, Z., Eds.; Journal of Chromatography Library; Elsevier: Boston, 2003; 213 -234.

Chapter 3
Particle Size Effects on Protein and Virus-Like Particle Adsorption on Perfusion Chromatography Media

3.1 Introduction

As discussed in Chapter 1, the adsorption kinetics of large biomolecules in conventional stationary phases is controlled predominantly by intraparticle diffusion, due to the fact that their transport is restricted by diffusional hindrance when the molecular size approaches the size of the matrix pores [1]. Even when the matrix pore size greatly exceeds the molecular size, however, transport is still slow since the molecular diffusion coefficients of these molecules are small [2]. Perfusion chromatography was originally developed to overcome intraparticle diffusional limitations in chromatography columns through the use of adsorbent particles with a bimodal pore structure that allows convective, pressure driven flow within larger pores transecting the particle while retaining significant binding capacity within the smaller, diffusive pores, which are connected to the convective through-pores [3].

A few models have been developed to predict the magnitude of intraparticle flow in such materials. The simplest one assumes that the ratio of intraparticle and extraparticle flows, F, is equal to the ratio of intraparticle and extraparticle hydraulic permeabilities. With reference to Fig. 1.3, the following relationship has been proposed based on the assumption that the particles can be represented as an assemblage of microparticles of

radius r_m and that both intraparticle and extraparticle permeabilities can be expressed according to the Carman-Kozeny equation [4-8]:

$$F = \left(\frac{\varepsilon_M}{\varepsilon}\right)^3 \left(\frac{1-\varepsilon}{1-\varepsilon_M}\right)^2 \left(\frac{r_m}{r_p}\right)^2 \tag{3.1}$$

where ε_M and ε and are the intraparticle and extraparticle void fractions, respectively, and r_p is the particle radius. The assumption that the microparticle radius is equal to three times the pore radius is often made, leading to [6, 7]:

$$F = 9\left(\frac{\varepsilon_M}{\varepsilon}\right)^3 \left(\frac{1-\varepsilon}{1-\varepsilon_M}\right)^2 \left(\frac{r_{pore,M}}{r_p}\right)^2 \tag{3.2}$$

where $r_{pore,M}$ is the macropores radius.

A second, more complex model is that of Neale et al. [9] introduced by Carta et al. [10] to describe flow in perfusion chromatography media. This model uses the Happel free surface model [11] to describe flow in the extraparticle porosity of the chromatography column coupled with the Brinkmann extension of Darcy's law [12] to describe intraparticle flow. In the general case, the Neale et al. model predicts a variable mobile phase velocity within the particle. In practice, however, since for actual perfusion chromatography media the intraparticle permeability is much smaller than the extraparticle permeability, the Neale et al. model predicts a nearly uniform intraparticle velocity whose magnitude agrees closely with that predicted by eq. 3.1 [10].

A theoretical model was developed by Carta et al. and Carta and Rodrigues for spherical particles based on the pulse response behavior of a chromatographic column under linear isotherm conditions. This model, given by the following equation, describes

the convection-enhanced transport through an enhanced effective diffusivity $\widetilde{D}_e$ and an intraparticle Peclet number, $Pe_{intra} = ur_p F / 3D_e$ [6, 10]:

$$\frac{\widetilde{D}_e}{D_e} = \frac{Pe_{intra}}{3}\left[\frac{1}{\tanh(Pe_{intra})} - \frac{1}{Pe_{intra}}\right]^{-1} \tag{3.3}$$

where D_e is the effective diffusivity without effects of convection. At high values of Pe_{intra}, eq. 3.3 yields

$$\widetilde{D}_e = \frac{ur_p F}{9} \tag{3.4}$$

which corresponds to conditions where intraparticle transport in the convective pores is completely convection controlled and independent of diffusion. A similar result, also based on the assumption that the adsorption isotherm is linear, has been obtained by Frey et al. [7] based on the Glueckauf linear driving force (LDF) approximation [13]. Liapis and McCoy [14] and Liapis et al. [15] obtained numerical solutions of the intraparticle convection-diffusion model of Carta et al. [10] for the Langmuir isotherm case for slab-shaped and spherical particles. For spherical particles under strong binding conditions, the calculations of Liapis et al. [15] show spherically asymmetrical intraparticle profiles that are increasingly skewed in the direction of flow at high Pe_{intra}. It should be noted that even though eq. 3.3 was developed for the linear isotherm case, the same expression can also be used to predict analytically breakthrough curves for a favorable isotherm using the LDF approximation by defining the rate coefficient as:

$$k = \frac{15\widetilde{D}_e}{r_p^2} \tag{3.5}$$

As shown by Carta [16], this equation yields results that are nearly coincident with those predicted by the numerical results of Liapis et al. for the full model indicating that the simpler LDF formulation is sufficient to explain the effects of the relevant and structural characteristics of the stationary phase.

Regardless of the model used, it is evident that particle size is expected to have a large effect. If intraparticle convection is absent, $\widetilde{D}_{\mathrm{e}} = D_{\mathrm{e}}$, and eq. 3.5 predicts that, as is well known, the mass transfer rate varies in inverse proportion to the square of the particle size. On the other hand, if intraparticle convection is dominant, combining eqs. 3.1 and 3.3, yields $\widetilde{D}_{\mathrm{e}} \propto u r_{\mathrm{p}} F \propto u / r_{\mathrm{p}}$, which results in a mass transfer rate that is expected to vary with the cube of the particle size.

The overarching goal this part of the dissertation is to determine experimentally the effects of particle size on perfusion chromatography. There are four specific objectives. The first is to determine the structural characteristics of POROS HS 20, which has structure similar to that of POROS HS 50, but about one half the particle radius. The second is to obtain the HETP as a function of flow rate for different proteins and a VLP under non-binding conditions and, thus, elucidate transport in the absence of binding. The third is to determine the intraparticle adsorbed concentration profiles during transient adsorption of proteins and VLPs on POROS HS 20 using CLSM and, thus, elucidate transport under binding conditions. The final objective is to compare the experimental results to available models to determine their ability to predict performance for actual systems.

3.2 Materials and Methods

3.2.1 Materials

The resin used in this work, POROS HS 20, was obtained from Applied Biosystems (Life Technologies Corporation, Grand Island, NY, USA). According to the supplier, POROS HS 20 has the same structure as POROS HS 50, but smaller particle size. Both materials are based on a poly(styrene-divinylbenzene) backbone functionalized with sulfopropyl cation exchange groups. The particle size distribution was obtained from taking microphotographs of POROS HS 20 particles suspended in aqueous solution and the images were analyzed by Image J. The volume-average particle diameter $\bar{d}_{\mathrm{p}}$ and standard deviation σ_{p} of the particle size distribution were then calculated from the following equations:

$$\bar{d}_{\mathrm{p}} = \sum_{\mathrm{j=1}}^{\mathrm{M}} f_{\mathrm{j}} d_{\mathrm{p,j}} \tag{3.6}$$

$$\sigma_{\mathrm{p}} = \sqrt{\sum_{\mathrm{j=1}}^{\mathrm{M}} f_{\mathrm{j}} \left(d_{\mathrm{p,j}} - \bar{d}_{\mathrm{p}} \right)^2} \tag{3.7}$$

where f_{j} is the volume fraction of particles of diameter $d_{\mathrm{p,j}}$. The particle size distribution of was found, as shown in Fig. 3.1, to span the range from 12 to 36 μm. The volume-average particle diameter is 23 μm, about one half the volume-average particle diameter of the POROS HS 50 sample used in Chapter 2 (Fig. 2.3).

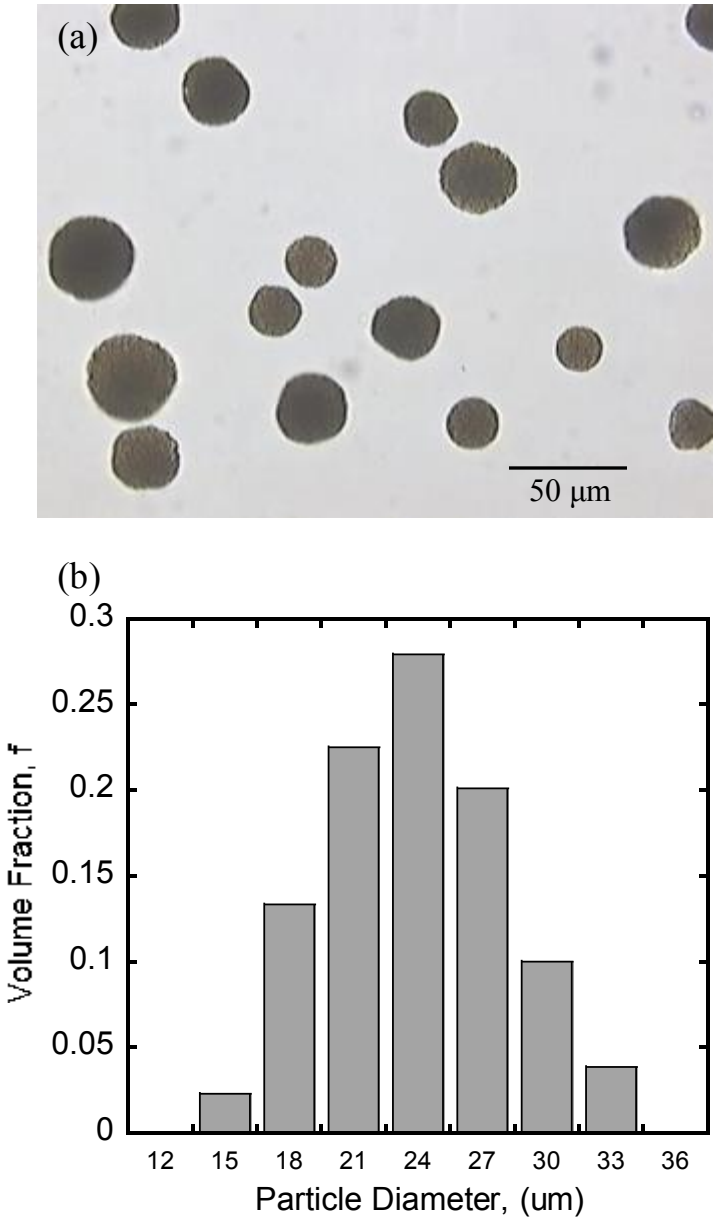

Figure 3.1. (a) Representative microphotographs of POROS HS 20 sample at 100 X magnification; (b) particle size distributions for POROS HS 20 sample.

The proteins and VLPs used are also the same as those described in Section 2.2.1 and are chicken egg white lysozyme (Lyo, M_r ~ 15 kDa, pI ~ 11), a monoclonal antibody (IgG, M_r ~ 150 kDa, pI ~ 8.6) available in our laboratory, and bovine thyroglobulin (Tg, M_r ~ 690 kDa, pI ~ 5). Both Lyo and Tg were obtained from Sigma Chemical Co. (St. Louis, MO, USA). The molecular mass of the mAb is determined by non-reducing SDS-PAGE and was characterized by size-exclusion chromatography (SEC) using a Superdex 200 size-exclusion column (10×200 mm) obtained from GE Healthcare and the purity of the sample was determined as >99% monomer. VLPs of recombinant human papillomavirus (HPV) Type 11 capsid protein L1 were provided by Merck & Co., Inc. (West Point, NJ, USA). All other chemicals were purchased from Fisher Scientific (Pittsburgh, PA, USA). The non-ionic surfactant Polysorbate 80 (PS-80, obtained from Amresco, Solon, OH, USA) was added to the VLP solutions at the 0.015 wt% level to improve stability [17]. These solutions remained stable for several days at 4 °C and for at least 1 day at room temperature.

3.2.2 Methods

The methods used in this work are essentially the same as those previously described in Section 2.2.2 and are described here only succinctly. The resin charge density was determined by frontal analysis. For this purpose, a 1-mL column packed with the resin sample was first equilibrated with 50 mM sodium acetate at pH 5.0 and then subjected to a step change to arginine acetate at pH 5.0. The ensuing arginine breakthrough curve, monitored by following the UV absorbance, was used to calculate the charge density by material balance. Since the arginine-sodium exchange is favorable for these conditions, a sharp breakthrough curve is obtained resulting in a precise

determination of the resin charge density [18]. Fig. 3.2 shows the arginine-sodium exchange curves for POROS HS 20 and POROS HS 50. The resulting values of the charge density were 71 and 135 μequiv/mL of packed bed for POROS HS 20 and POROS HS 50, respectively.

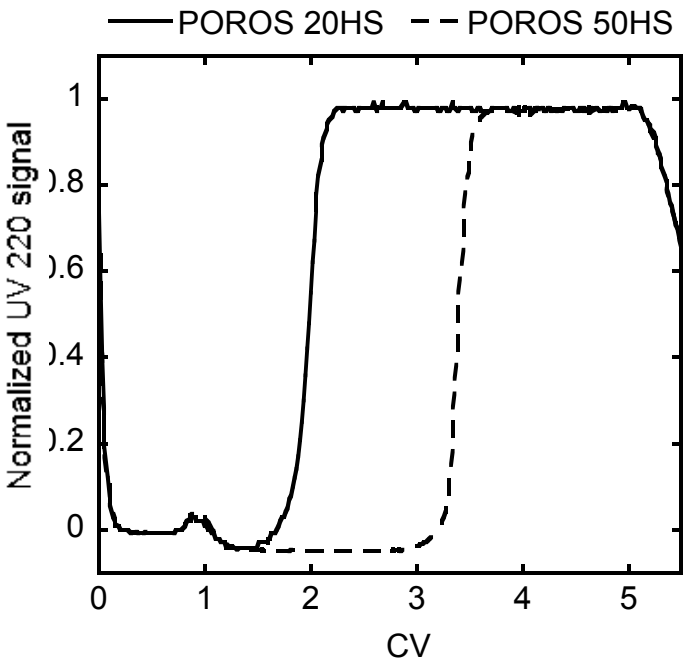

Figure 3.2. Arginine-sodium exchange curves for POROS HS 20 and POROS HS 50.

The internal structure of the resin was determined by transmission electron microscopy (TEM). POROS HS 20 particles were first dehydrated with water-ethanol mixtures increasing from 0 to 100% ethanol and then embedded in LRWhite resin (London Resin Company, London, UK), by first saturating them with a 50:50 (v/v) mixture of ethanol and LRWhite and then with 100% LRWhite. After curing overnight at 45 °C, the embedded samples were sectioned with an ultramicrotome to produce 80 nm slices, which were then imaged with a Jeol 100 CX transmission electron microscope.

Inverse size exclusion chromatography (iSEC) was used to determine the accessible intraparticle volume and the apparent pore size using as probes glucose and dextran samples with molecular mass between 4 and 2,000 kDa, obtained from Spectrum Chemical Manufacturing Co. (Gardena, CA, USA). A packed column with a 0.5 cm diameter and 5 cm column length was used for this purpose. The experiment was conducted at a flow rate of 0.5 mL/min (150 cm/h) with a mobile phase consisting of 1 M NaCl in 10 mM Na_2HPO_4 at pH 7.0. 10–20 μL injections of each probe were made with a Waters HPLC system. The same measurements were made with proteins and VLPs samples, with a mobile phase consisting of 1.5 M NaCl in 10 mM Na_2HPO_4 at pH 7.0. The first moment of each peak, μ, was obtained by calculating the apparent first moment and subtracting from it the first moment obtained without the resin using the columns with inlet and outlet plungers pushed together. The extraparticle porosity, $\varepsilon = 0.326$, of the column used for these measurements was obtained using the Carman-Kozeny equation [19] based on the linear pressure-flow curve observed for this column.

Isocratic pulse response experiments were conducted under nonbinding conditions (1 M NaCl for Lyo, IgG and Tg, and 1.5 M NaCl for the VLPs) to determine pore accessibility by proteins and VLPs and to determine the HETP as a function of mobile phase velocity. These measurements were made with the same column used for iSEC at flow rates between 0.2 to 4 ml/min corresponding to mobile phase superficial velocities between 60 and 1200 cm/h. The ensuing peaks were analyzed by the moment method as discussed by Carta and Jungbauer [1] as described in detail in Section 2.2.2 by eqs. 2.5-2.7.

The protein adsorption capacity was determined from batch experiments using a material balance based on the residual protein concentrations in solutions contacted with resin samples for 24 hours. The density of the hydrated resin particles, determined with a picnometer to be 1.05 g/mL, was used to convert the amount of protein adsorbed from a mass basis to units of mg per mL of hydrated particle volume. Breakthrough curves, obtained with 1-mL packed columns (0.5 cm diameter × 5 cm long) at a velocity of 300 cm/h, were used to confirm the batch capacity values by determining the area under the breakthrough curve. Protein solutions were prepared in aqueous buffers containing 20 mM CH_3COONa at pH 5.0 for IgG and Tg.

Confocal laser scanning microscopy (CLSM) was used to determine the intraparticle concentration profiles of adsorbed IgG, Tg, and VLPs using samples labeled with Rhodamine Red™-X dye obtained from Invitrogen Corporation (Carlsbad, CA, USA) as described in Section 2.2.2 and [20]. Batch measurements were made by suspending the particles in an agitated protein solution, withdrawing samples with a pipette from the solution at set time intervals, and rapidly removing the solution removed together with the particles by spinning the samples in a microcentrifuge filer tube. Since the POROS HS 20 particles are opaque in aqueous solution, as was the case for POROS HS 50, the CLSM images were collected after rapidly immersing the particles in benzyl alcohol. Since benzyl alcohol matches approximately the refractive index of the resin backbone, the particles become sufficiently transparent to allow collect of fluorescence emitted throughout the beads. CLSM images under flow condition were collected using the flow cell described in detail in Section 2.2.2. For this purpose, the particles were inserted in 50 um capillaries with a square section (Polymicro Technologies, Phoenix, AZ,

USA). The capillaries were first fed with the protein solution for a set period of time and then rapidly flushed with benzyl alcohol prior to imaging. Optical sections of the resin beads were collected in 2 μm z-increments and analyzed using LSM Image Examiner software (Carl Zeiss MicroImaging, LLC, Thornwood, New York, NY, USA). A new capillary was used for each successive measurement to assure that the benzyl alcohol did not alter the resin structure.

3.3 Results and Discussion

3.3.1 Resin Structure

Figure 3.3 shows side-by-side representative TEMs of POROS HS 20 and POROS HS 50 particles at two different magnifications. The lighter gray areas are the acrylic resin used to embed the particles while the darker areas are the POROS backbone. White spots visible in the images are artifacts caused by incomplete infiltration and/or sectioning. The structure appears to be essentially the same for both samples. At low magnification (Fig. 3.3a and b), a distribution of pore sizes is visible in both materials. At higher magnification (Fig. 3.3c and d), the microgranular structure of these materials becomes evident for both samples which appear to consist of 100–200 nm granules forming microparticle aggregates that are 500 to 1000 nm in diameter. It is clear that both large pores, which appear to transect the particles, and smaller pores, which are located within the microparticle aggregates, are present in both resins.

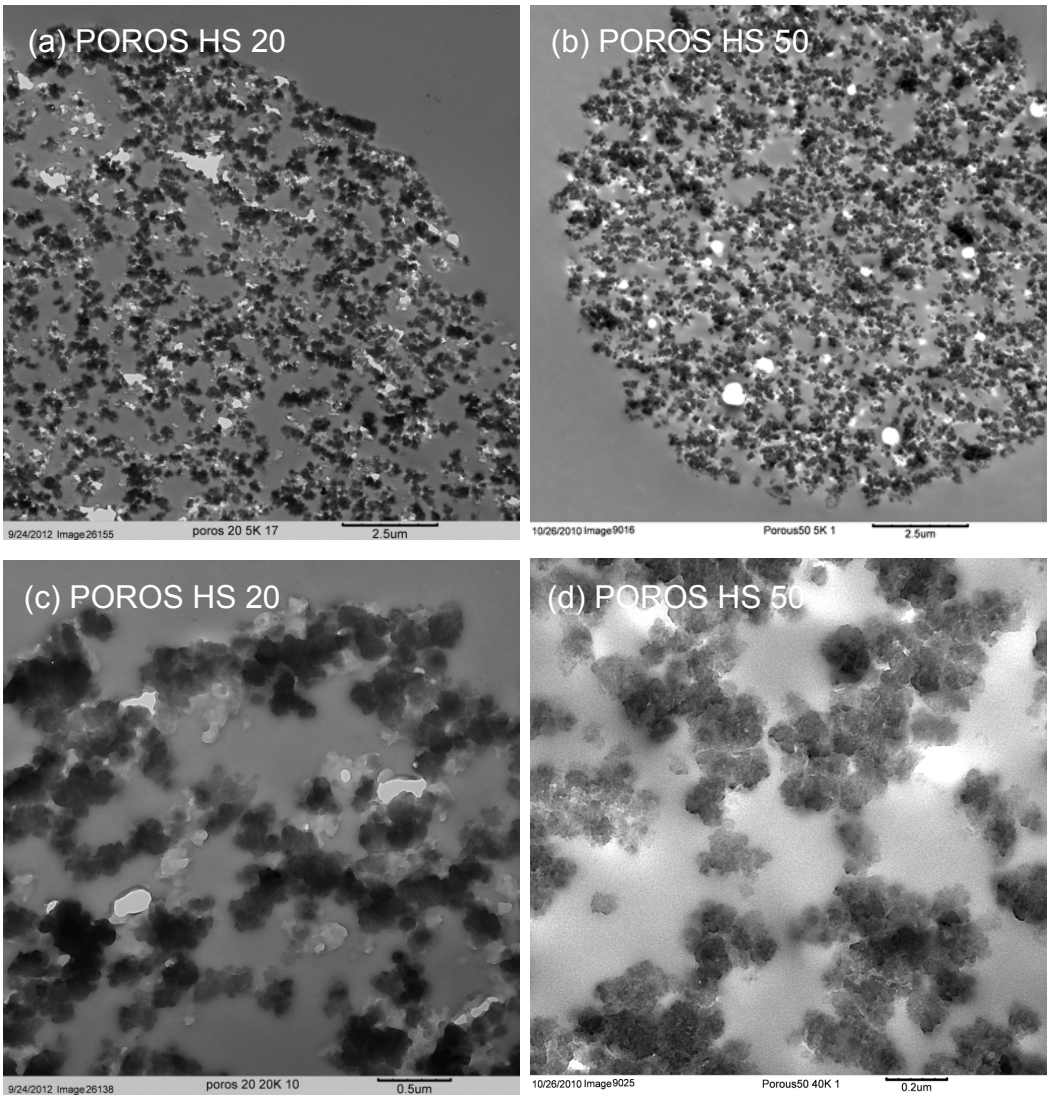

Figure 3.3. TEM images of POROS HS 20 (a and c) and POROS HS 50 (b and d) at 5 K and 20 K magnifications.

Figure 3.4 shows the isocratic elution peaks for dextrans and unretained proteins and VLPs obtained for non-binding conditions. The column extraparticle void fraction is represented by the vertical dashed line. In terms of elution volumes, these results are very similar to those obtained previously for POROS HS 50 (Fig. 2.5). Glucose elutes at about 0.7 CV and dextran with 2,000 kD molecular mass eluting as a broad, skewed peak between 0.2 and 1.2 CV. The results indicate that for both materials, while glucose gains access a large fraction of the intraparticle volume, the dextrans are excluded to an increasing extent as their molecular mass increases. As seen in Fig. 3.4b, the proteins are also partially excluded, eluting earlier as the molecular mass increases, while the VLPs are eluted in a manner similar to the 2,000 kD dextran. K_D-values calculated from these data as described in Section 2.3.1 by the following equations:

$$K_D = \varepsilon_M K_{D,M} + (1 - \varepsilon_M)\varepsilon_m K_{D,m} \tag{3.8}$$

where ε_M and ε_m are the macropore and micropore porosities, respectively, and

$$K_{D,M} = \left(1 - \frac{r_s}{r_{pore,M}}\right)^2 \tag{3.9}$$

$$K_{D,m} = \left(1 - \frac{r_s}{r_{pore,m}}\right)^2 \tag{3.10}$$

are the distribution coefficients for partitioning in the macropores and microprores, respectively. Fig. 3.5 shows K_D-values as a function of hydrodynamic radius together with the data obtained previously chapter for POROS HS 50. For both materials, K_D initially decreases rapidly as r_s increases, but then declines much more gradually for $r_s >$

10 nm. The K_D-data to a bimodal pore size distribution with radii $r_{pore,M}$ and $r_{pore,m}$ are fitted using eq. 3.8-3.10. Table 3.1 summarizes the fitted values in comparison to those obtained previously for POROS HS 50. Obviously, the values are very similar confirming that the two resin samples have nearly the same structure.

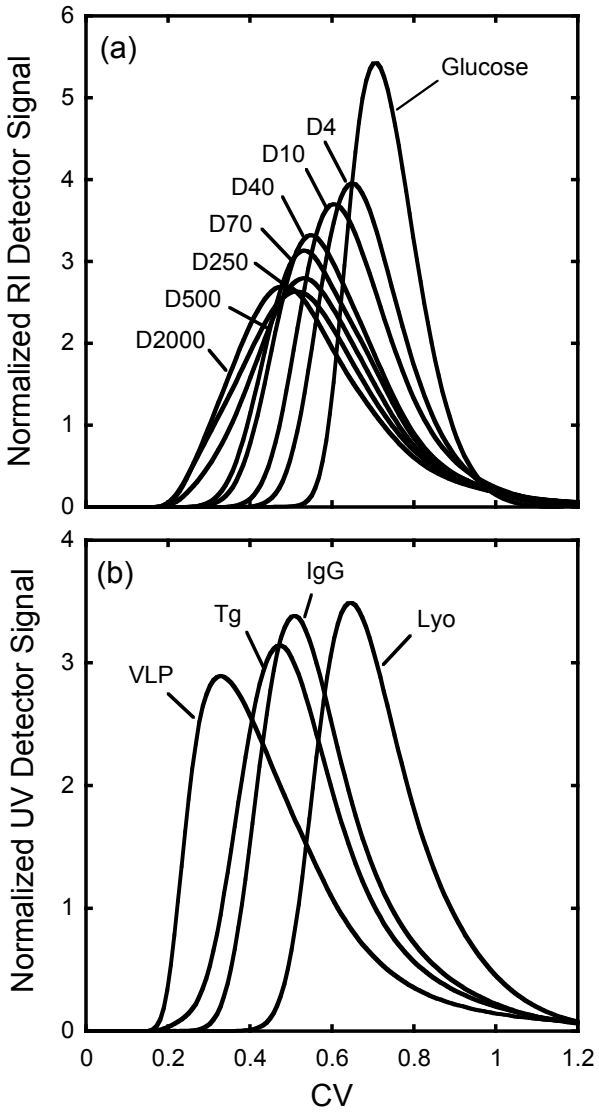

Figure 3.4. Representative iSEC chromatograms for a POROS HS 20 column of (a) dextran and (b) protein and VLP samples under non-binding conditions. The mobile phase velocity is 150 cm/h.

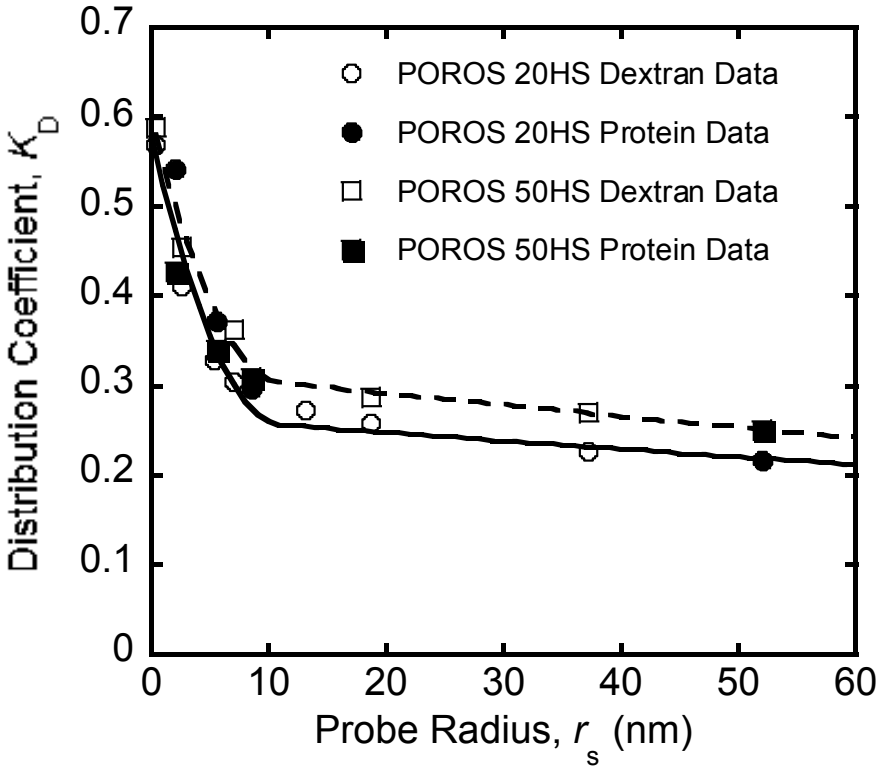

Figure 3.5. K_D-values determined from iSEC for POROS HS 20 and POROS HS 50 vs. probe hydrodynamic radius. The lines are based on eq.3.8 with parameters from Table 3.1.

Table 3.1. Porosities and pore sizes determined from iSEC.

	POROS HS 20	POROS HS 50
ε_p	0.58	0.60
ε_M	0.27	0.32
ε_m	0.43	0.41
$r_{pore,M}$ (nm)	550 ± 15	470 ± 10
$r_{pore,m}$ (nm)	11 ± 4	11 ± 4

3.3.2 HETP for Non-Binding Conditions

Figure 3.6 shows the reduced HETP (h=HETP/d_p) versus reduced velocity (v' = vd_p /D_0) obtained for non-binding conditions for all three proteins and the VLPs for POROS HS 20 in comparison with previous data for POROS HS 50. For both resins, the actual mobile phase velocities cover the same range from 60 to 1200 cm/h, but, for each solute, the data are shifted toward smaller *v'* values for POROS HS 20 because of the smaller particle diameter. Note that the four graphs are shown on the same vertical scale but over different ranges of *v'* according to the different values of D_0. For Lyo (Fig. 3.6a), the data follow straight lines, indicating essentially complete dominance of diffusion for both resin samples. Increasingly distinct plateaus are observed, however, for IgG, Tg, and the VLP with the transition from linear to constant HETP occurring at lower *v'* values for POROS HS 20 compared to POROS HS 50 and for IgG compared to the larger Tg and VLP.

As described in Section 2.3.2, the following equation adapted from ref. [6] was used to fit the HETP data:

$$h = a + \frac{1}{30}\frac{\varepsilon}{1-\varepsilon}\left(\frac{k'}{1+k'}\right)^2 \frac{\tau_M}{\varepsilon_M K_{D,M}}\left[\frac{D_e}{\widetilde{D}_e} + \frac{b-1}{b^2}\frac{\tau_m}{\tau_M}\left(\frac{r_m}{r_p}\right)^2\right]v' \qquad (3.11)$$

which describes the effects of perfusion for a column packed with particles with radius r_p, which, in turn, are composed of microparticles of radius r_m containing diffusive pores. Since, based on the TEMs, r_m is on the order of 0.5 μm, (r_m/r_p) << 1 , making the second term in brackets of eq. 3.11 negligibly small, which reduces eq. 3.11 to the following equation:

$$h = \frac{HETP}{d_p} = a + \frac{1}{30}\frac{\varepsilon}{1-\varepsilon}\left(\frac{k'}{1+k'}\right)^2 \frac{\tau_M}{\varepsilon_M K_{D,M}}\frac{D_e}{\widetilde{D}_e}v' \qquad (3.12)$$

Since the ratio $D_e / \widetilde{D}_e$ is theoretically described by eq. 3.3, the only fitting parameters are the intraparticle flow fraction, F, and the macropore tortuosity factor, τ_M. Table 3.2 gives a summary of the values of these parameters determined by fitting eq. 3.11 to the HETP data. Calculated curves are shown in Fig. 3.6. As seen from Table 3.2, similar values of τ_M are obtained for the two resins, averaging 3.1 and 2.4 for POROS HS 20 and 50, respectively, consistent with their similar structure. However, much higher values of F, averaging 0.0018, are obtained for POROS HS 20 compared to POROS HS 50, for which the average F-value is 0.00063. According to eq. 3.1, F is dependent on the extraparticle and intraparticle porosities and on the microparticle radius, r_m. Since ε and ε_M are known for each resin from the iSEC data, eq. 3.1 can be used to calculate what values of r_m are consistent with the regressed values of F. The resulting values of r_m are 0.68 and 0.65 μm for POROS HS 20 and POROS HS 50, respectively. Since these values are nearly the same for both resins and are roughly consistent with the TEMs, it appears that eq. 3.1 can indeed be used to predict the effects of particle size. Note that the ratio of F-values for the two resins is about 2.9, which is less than the ratio of the square of the particle diameters. The difference is caused by the different values of ε_M, which are 0.27 and 0.32 for POROS HS 20 and POROS HS 50, respectively. Although this difference is only about 19%, the effect of ε_M on F is very strong according to eq. 3.1 resulting in a substantially lower value of F for POROS HS 20.

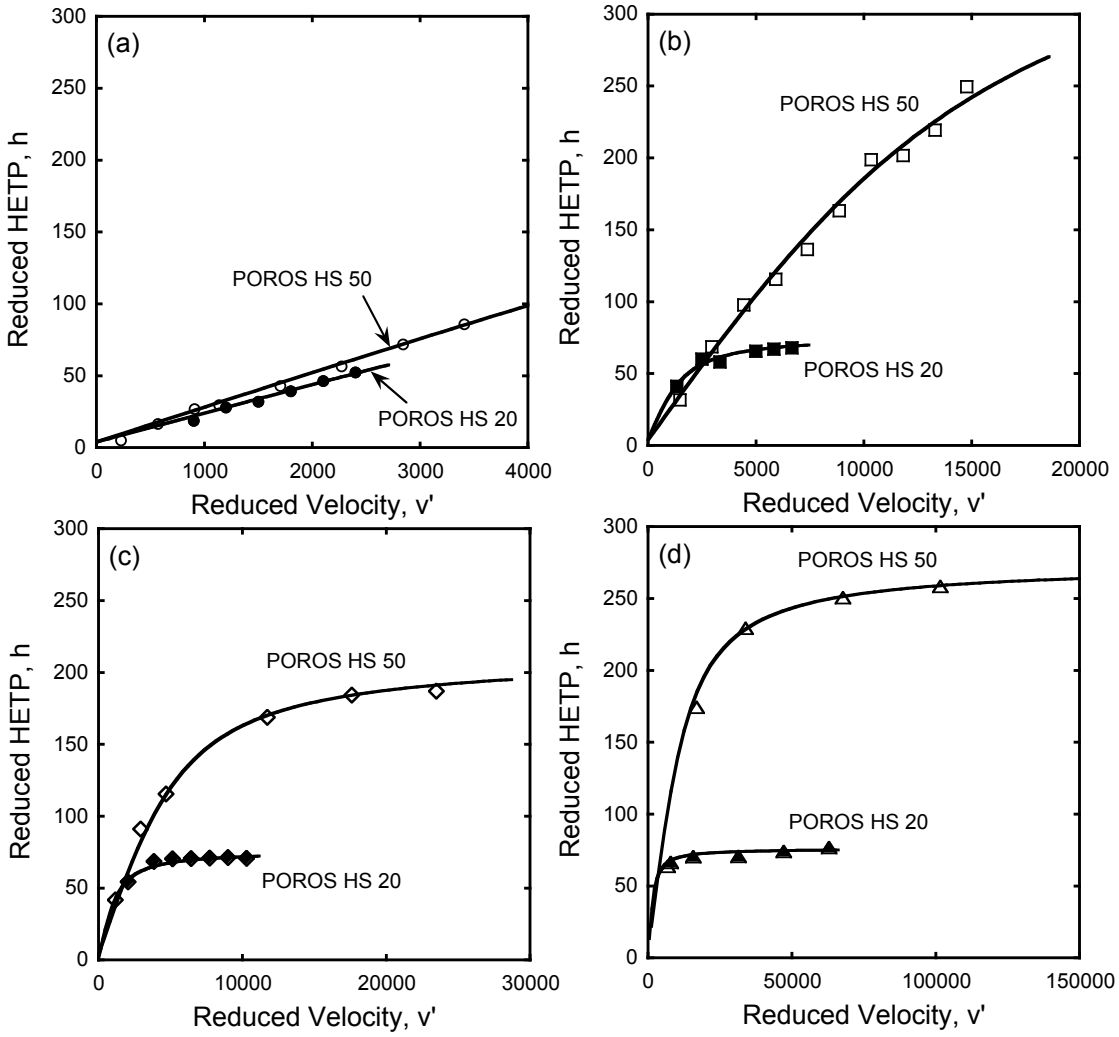

Figure 3.6. Reduced HETP vs. reduced velocity for proteins and VLPs under non-binding conditions. Solid symbols are for POROS HS 20. Open symbols are for POROS HS 50 and are from Section 2.3.2. Lines are based on eq. 8 with parameters from Tables 3.1 and 3.2.

Table 3.2. Parameters for perfusion model based on HETP data according to eq. 3.11 with $a = 4$ and $b = 0$.

	POROS HS 20		POROS HS 50	
	τ_M	F	τ_M	F
Lyo	1.4	No effect	1.9	No effect
IgG	3.3	0.0022	2.1	0.00050
Tg	4.5	0.0017	3.4	0.00082
VLP	3.0	0.0016	2.0	0.00058
Average	3.1	0.0018	2.4	0.00063

3.3.3 Protein Adsorption Equilibrium and Kinetics

Figure 3.7 shows the adsorption isotherms for IgG on both POROS resins. Both resins exhibit sharp isotherms for these conditions. However, despite the fact that the matrix structures is very similar, the binding capacity is about 26% lower for POROS HS 20 compared to POROS HS 50, likely as a result of the lower charge density of POROS HS 20 (see Section 3.2.2). In both cases, the data are described approximately by the Langmuir isotherm, $q = q_m KC/(1+KC)$, with q_m = 105 ± 2 mg/mL and K = 96 ± 20 mL/mg for POROS HS 20 and q_m = 143 ± 3 mg/mL and K = 120 ± 60 mL/mg for POROS HS 50.

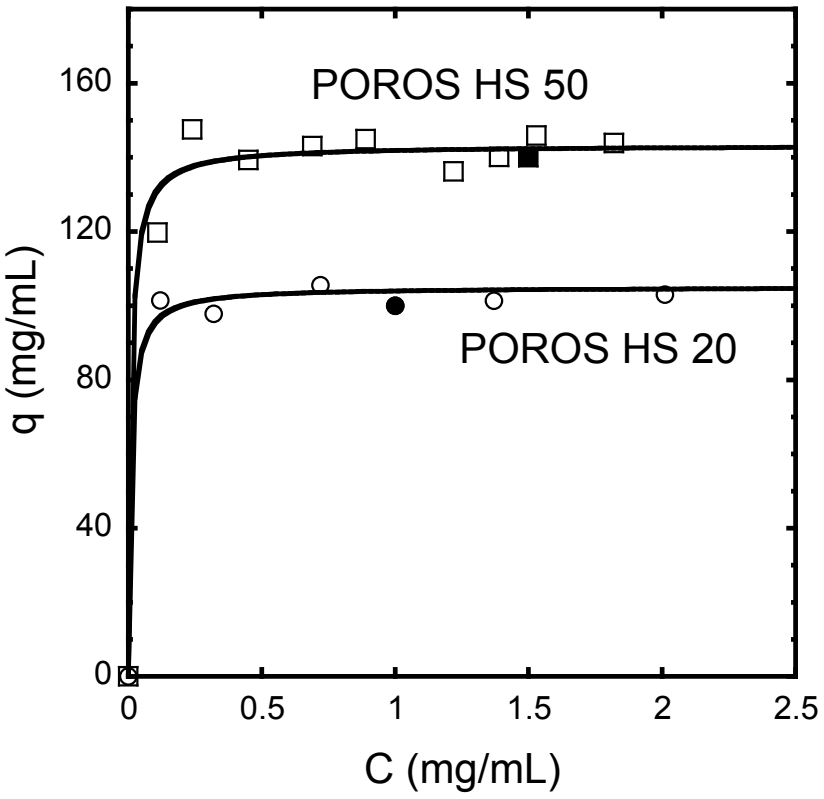

Figure 3.7. Adsorption isotherms for IgG on POROS HS 20 and POROS HS 50 in 20 mM sodium acetate at pH 5.0. Lines are the Langmuir isotherm $q = q_m KC/(1 + KC)$ where K is the equilibrium constant. Open symbols are batch data. Solid symbols are based on breakthrough experiments conducted with 1-mL columns at a 1 min residence time.

Figure 3.8 shows representative CLSM images of the progress IgG adsorption on POROS HS 20 over time under both batch and flow conditions at 1000 cm/h. For comparison purposes, an image of IgG adsorption on POROS HS 50 is included for the same conditions of the POROS HS 20 experiments. For batch adsorption (Fig. 3.8a), the CLSM images show fairly sharp and relatively symmetrical adsorption fronts consistent with the shrinking core model [21] indicating diffusion dominated mass transfer. For these conditions, the normalized position of the adsorption front in the particle, $\rho_{sat} = r_{sat} / r_p$, is related to time by the following equation [22]:

$$f(\rho_{sat}) = 2\rho_{sat}^3 - 3\rho_{sat}^2 + 1 = \frac{6 D_e C_0}{q_m r_p^2} t \tag{3.13}$$

where C_0 is protein solution concentration, t is time and q_m the binding capacity. Fig. 3.9 shows the IgG batch adsorption data plotted according to eq. 3.13 as $f(\rho_{sat})$ vs. $C_0 t / q_m r_p^2$. The slope of the ensuing straight line yields an effective pore diffusivity D_e = (3.1 ± 0.1) $\times 10^{-8}$ cm^2/s. This value is similar in magnitude to that obtained for the same conditions in Section 2.3.3 for POROS HS 50, D_e = (2.5 ± 0.1) $\times 10^{-8}$ cm^2/s, indicating that diffusional transport of IgG occurs at similar rates in the two resins. The tortuosity factor POROS HS 20, calculated as $\tau_M = \varepsilon_M K_{D,M} D_0 / D_e$, is 3.4 ± 0.1, which is consistent with the value determined for non-binding conditions, indicating that diffusional transport in this resin is not affected by protein binding.

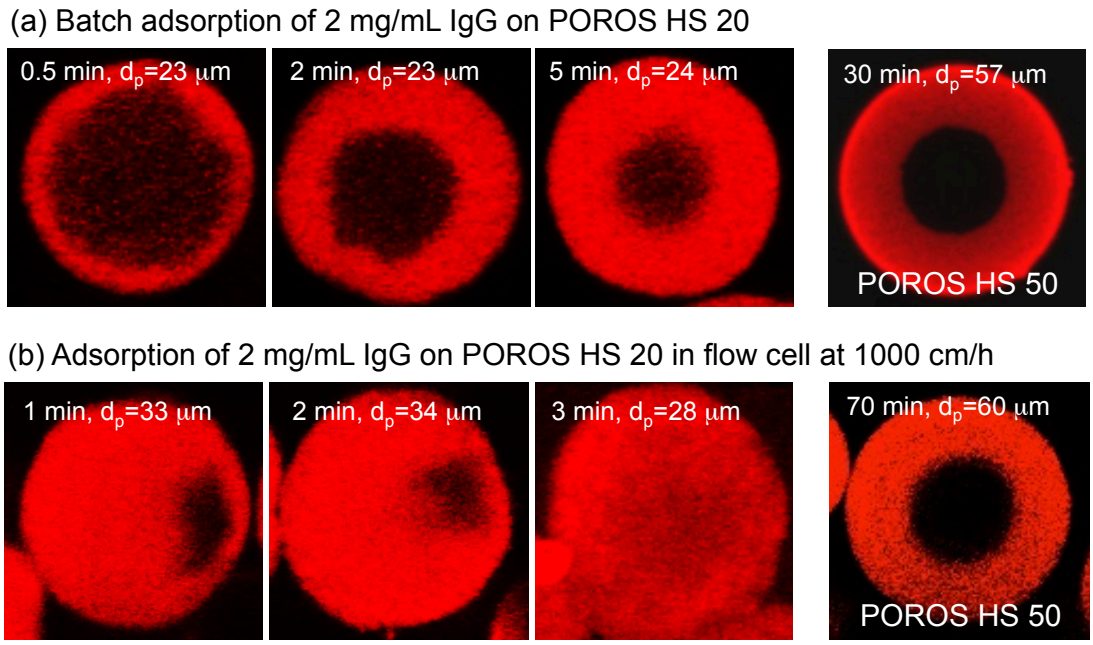

Figure 3.8. CLSM images for the adsorption of 2 mg/mL IgG in 20 mM sodium acetate at pH 5.0 on POROS HS 20 under (a) batch adsorption conditions and (b) flow condition at 1000 cm/hr. The two panels on the right hand side are for POROS HS 50 in Section 2.3.3 at 2 mg/mL IgG (a) and 1 mg/mL IgG (b) under conditions otherwise identical to the POROS HS 20 data. Flow in b is from left to right.

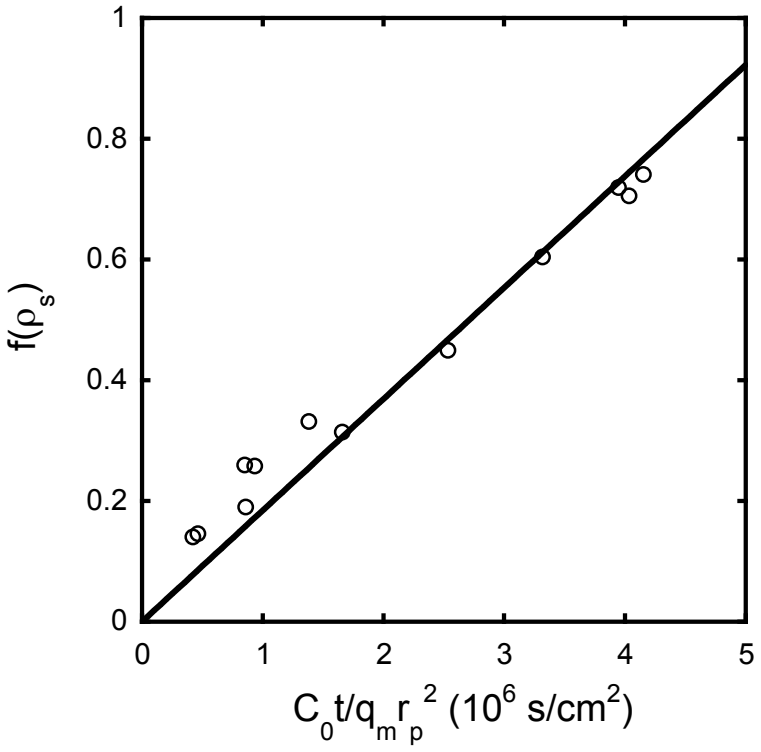

Figure 3.9. Plot of dimensionless position of adsorption front vs. reduced time according to eq. 11 for batch adsorption of 2 mg/mL IgG in 20 mM sodium acetate at pH 5.0 on POROS HS 20 based on CLSM images.

For flow conditions (Fig. 3.8b), the adsorption front in POROS HS 20 is clearly asymmetrical and stretched in the direction of flow. The overall rate also appears to be much faster than for the batch measurements, with the particles achieving saturation in less than 3 min. By comparison, as seen from the right-hand side panels of Fig. 3.8, the effects of flow on the adsorption kinetics are very small for POROS HS 50. In this case, the adsorption front is nearly symmetrical under both conditions and propagates at the same rate when the different IgG concentration used in the two experiments (2 mg/mL in the batch measurement and 1 mg/mL under flow) is accounted for.

In order to quantitatively determine the adsorption rate under flow, the fractional saturation of POROS HS 20 particles loaded with IgG under flow was obtained by averaging the degree of saturation of optical sections of the same particle at 4 μm intervals along the z-axis perpendicular to the field of view and to the direction of flow. The fraction of area saturated with IgG for each section, ϕ_i, was determined graphically using the same method as described in detail in Section 2.2.3. The fractional saturation of the particle was then calculated by averaging across the particle diameter according to the following equation:

$$\frac{\bar{q}}{q_m} = \frac{3}{4r_p^3} \sum_i \phi_i r_{p,i}^2 \Delta z \tag{3.14}$$

where Δz the section thickness.

Figure 3.10 shows the z-stacks for two different POROS HS 20 particles exposed to 2 mg/mL IgG for 2 min at 1000 cm/h. Due to fluorescence attenuation effects, the intensity of the fluorescence decreases somewhat from the bottom (closer to the microscope objective lens) to the top (farthest form the objective lens) of the particle. Nonetheless, it is evident that sections near both bottom and top of the particle (i.e. at low and high z-values) are nearly completely saturated, while those near the particle center show asymmetrically distributed degree of saturation. These results are qualitatively consistent with the patterns predicted by the theoretical model of Liapis et al. [16] at high values of Pe_{intra}, as well as with the results for the adsorption of the slower-diffusing Tg on POROS HS 50 shown in Fig. 2.12. By setting $\bar{q}/q_m = 1 - \rho_{sat}^3$, the following equation derived from eq. 3.13 was used to calculate the convection-enhanced effective diffusivity $\tilde{D}_e$ for each particle:

$$3 - 2\frac{\bar{q}}{q_m} - 3\left(1 - \frac{\bar{q}}{q_m}\right)^{\frac{2}{3}} = \frac{6D_e C_0 t}{q_m r_p^2} \tag{3.15}$$

The resulting values for the two particles are 6.9×10^{-8} and 7.1×10^{-8} cm^2/s, respectively. Since, in the absence of flow, $D_e = 3.1 \times 10^{-8}$ cm^2/s, the ratios $\widetilde{D}_e / D_e$ for the two particles are 2.2 and 2.3, respectively. Based on the HETP measurements, F is on the order of 0.0018, which 1000 cm/h yields values of Pe_{intra} of 8.6 and 7.5, respectively. In turn with these values of Pe_{intra} eq. 3.3 gives $\widetilde{D}_e / D_e$ = 3.3 and 2.9, respectively, for the two particles. Considering the fact that the particles in the capillary are only a rough approximation of the flow conditions in the actual packed column experimental and predicted values of $\widetilde{D}_e / D_e$ are reasonably close to the experimental values, consistent with mass transfer rates that are 2 to 3 times higher under flow than those observed under no-flow conditions.

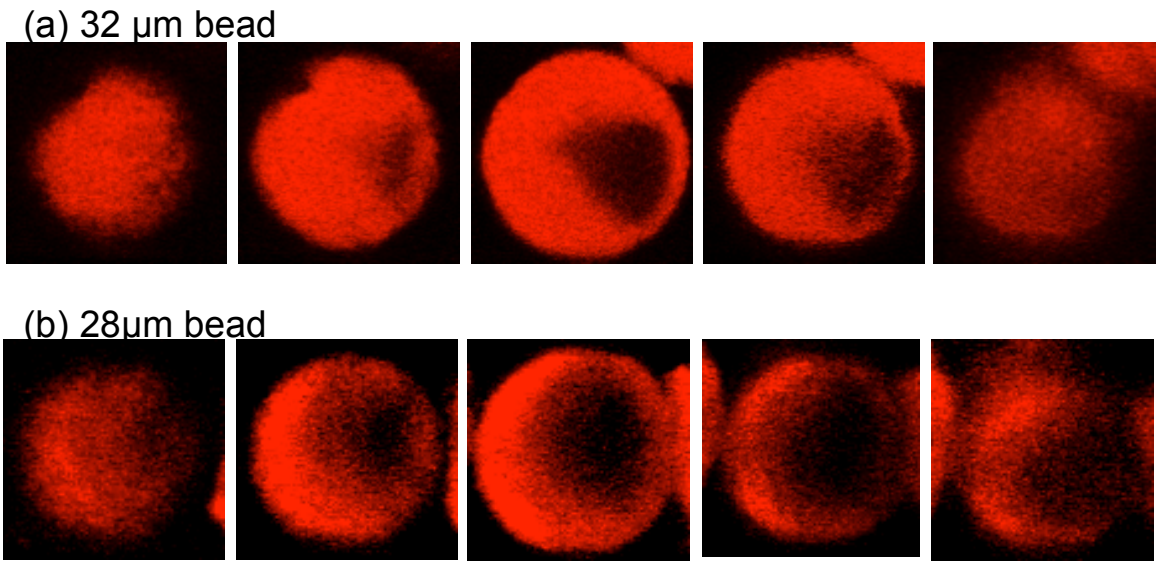

Figure 3.10. CLSM images of representative sections of two different POROS HS 20 particles exposed to 2 mg/mL IgG for 2 min in the flow cell at 1000 cm/h. The sections shown are located at vertical distances of 3, 7, 16, 22 and 28 µm for the 32 µm particle (a) and at vertical distances of 3, 7, 13, 19 and 25 µm for the 28 µm particle (b) from the bottom of each particle. In both cases, distances are given from the particle top (left) to the bottom (right). Flow is from left to right.

3.3.4 VLP Adsorption

Figure 3.11 shows CLSM images for the adsorption of VLPs on POROS HS 20 particles in both batch and flow conditions. Representative images, based on results from Section 2.3.3 at a 2-hour contact time are also shown for POROS HS 50. Both cases show similar results with adsorption apparently confined to a thin shell, 1–2 µm thick, on the outer surface of the beads. Thus, it appears that the bound VLPs block access to the through-pores. The depth of penetration of the bound VLPs is similar in magnitude for POROS HS 20 and POROS HS 50. Because of the spherical geometry, a relatively large fraction of the binding capacity resides near the outer edge of the beads. For

example, although a 1-μm surface layer of bound VLPs is only 9% of the particle radius; this value corresponds to about 24% of the potential binding capacity. Thus, POROS HS 20, as a result of its smaller size, is expected to have a greater VLP binding capacity on a volumetric basis. The higher relative surface roughness of the POROS HS 20 beads, seen in the TEM images, may also contribute to this result. Nevertheless, it is evident that matrices with even larger pores would be needed to allow transport and adsorption of these VLPs throughout the particle volume.

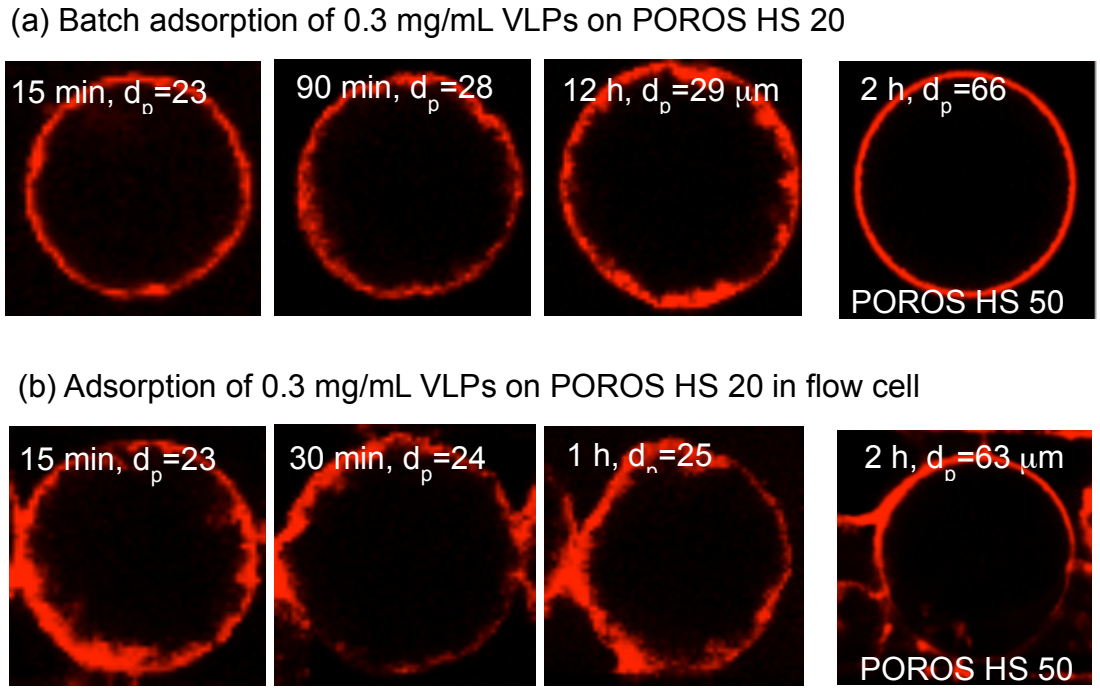

Figure 3.11. CLSM images for the adsorption of 0.3 mg/mL VLPs in 200 mM MOPS and 250 mM citrate buffer at pH 7 on POROS HS 20 under (a) batch adsorption conditions and (b) flow condition at 1000 cm/hr. The two panels on the right hand side are for POROS HS 50 under conditions otherwise identical to the POROS HS 20 data and are both from Section 2.3.3. Flow in b is from left to right.

3.4 Conclusions

The particle size has a strong effect of protein and VLP transport in perfusion chromatography media for non-binding conditions. For these conditions, comparison of POROS HS 20, with a 23 μm average particle diameter and POROS HS 50, with a 52 μm particle diameter, shows a much stronger effect of intraparticle convection on the HETP for the latter, with the POROS HS 20 HETP becoming independent of flow rate and, thus,

convection dominated at reduced velocities of only about 6000. Much higher reduced velocities, around 15,000, are needed for POROS HS 50 to attain a dominance of intraparticle convections. The intraparticle concentration profiles obtained by CLSM for the adsorption of IgG on POROS HS 20 show a large effect of flow. At 1000 cm/h, as a result of intraparticle convection, the intraparticle concentration profiles become asymmetrical and skewed in the direction of flow as predicted by the theoretical model of Liapis et al. [15]. By comparison, POROS HS 50 shows nearly symmetrical adsorbed concentration profiles for the same protein both for conditions of no flow and at a flow rate of 1000 cm/h as a result of the larger particle size. Qualitatively similar results are obtained, however, for the VLPs, independent of particle size. For both POROS HS 20 and POROS HS 50, VLP adsorption is restricted to a thin layer near the particle surface, whose thickness is on the same order of magnitude as the size of the microparticles that make up the resin beads, likely as a result of pore blocking by the bound VLPs. In this case, one advantage of the smaller particles is that the VLP binding capacity is likely larger since the adsorbed layer, while nearly the same in thickness occupies a greater fraction of the particle volume. From a quantitative viewpoint, eq. 3.1 appears to be adequate for predicting the intraparticle flow ratio. In order to make quantitative predictions, however, it is necessary to establish a value of the microparticle size, r_m, which is consistent with the chromatographic behavior. Once this is determined, the effects of particle size are predicted by eq. 3.1 using empirically determined porosity values. As shown in this work for IgG, the same value of F, obtained for non-binding conditions can be used to predict transport rates under flow for conditions where the

protein is bound using a convection enhanced effective diffusivity, $\widetilde{D}_e$, calculated according to eq. 1.3.

3.5 List of Symbol

ε	extraparticle porosity
ε_M	macropore porosity
ε_m	micropore porosity
ε_p	intraparticle porosity
ϕ_i	fractional saturation for section i
ρ_{sat}	normalized position of the adsorption front in the particle
σ_p	standard deviation of the particle size distribution
τ_M	tortuosity factor in macroparticle pores
τ_m	tortuosity factor in microparticle pores
a	hydrodynamic dispersion factor
C	protein solution concentration (mg/mL)
C_0	initial protein solution concentration (mg/mL)
D_0	free solution diffusivity (cm^2/s)
D_e	effective diffusivity (cm^2/s)
$\widetilde{D}_e$	convection enhanced effective diffusivity (cm^2/s)
d_p	particle diameter (cm)

$\bar{d}_p$ volume-average particle diameter (cm)

F ratio of intraparticle and extraparticle flow velocities

f_j volume fraction of particles of diameter $d_{p,j}$

$HETP$ height equivalent to the theoretical plate (cm)

h reduced HETP

K adsorption constant in Langmuir model (mL/g)

K_D distribution coefficient

$K_{D,M}$ size exclusion in the macroparticle pores

$K_{D,m}$ size exclusion in the microparticle pores

k rate coefficient for LDF model (s^{-1})

k' retention factor

L column length (cm)

Pe_{intra} intraparticle Peclet number

q adsorbed phase protein concentration (mg/mL)

q_m maximum adsorption capacity in Langmuir model (mg/mL)

$\bar{q}/q_m$ fractional saturation of the particle

r_m microsphere radius (nm)

r_p particle radius (μm)

$r_{pore,M}$ macropore radius (nm)

$r_{pore,m}$ micropore radius (nm)

r_s molecular radius (nm)

r_{sat} radius of adsorption front (μm)

t time (s)

u superficial velocity (cm/s)

V_{column} column volume (mL)

v fluid velocity (cm/s)

v' reduced velocity ($=vd_p / D_0$)

3.6 References

[1] Carta, G., Jungbauer, A. (2010). Protein Chromatography – Process Development and Scale-up. Wiley-VCH, Weinheim, Germany

[2] Cussler, E.L. (2009). Diffusion: Mass Transfer in Fluid Systems, third ed.. Cambridge University Press

[3] Afeyan, N. B., Gordon, N. F., Mazsaroff, I., Varady, L., Fulton, S. P., Yang, Y. B., & Regnier, F. E. (1990). Flow-through particles for the high-performance liquid chromatographic separation of biomolecules: perfusion chromatography. *J. Chromatogr., 519*(1), 1-29

[4] Komiyama, H., Inoue, H. (1974). Effects of intraparticle flow on catalytic reactions. *J. Chem. Eng. Japan, 7*, 281-286

[5] Rodrigues, A.E., Ahn, B., Zoulalian, A. (1982). Intraparticle-forced convection effect in catalyst diffusivity measurements and reactor design, *AIChE J., 28,* 541-546

[6] Carta, G., Rodrigues, A.E. (1993). Diffusion and convection in chromatographic processes using permeable supports with a bidisperse pore structure. *Chem. Eng. Sci., 48*(23), 3927-3935

[7] Frey, D.D., Schweinheim, E., Horváth, C. (1993). Effect of intraparticle convection on the chromatography of biomacromolecules. *Biotechnol. Prog., 9*(3), 273-284

[8] Rodrigues, A.E. (1997). Permeable packings and perfusion chromatography in protein separation, *J. Chromatogr. A, 699,* 47-61

[9] Neale, G., Epstein, N., Nader, W. (1973). Creeping flow relative to permeable spheres. *Chem. Eng. Sci., 28,* 1865-1874

[10] Carta, G., Gregory, M.E., Kirwan, D.J., Massaldi, H.A. (1992). Chromatography with permeable supports: Theory and comparison with experiments. *Sep. Technol., 2*(2), 62-72

[11] Happel, J. (1958). Viscous flow in multiparticle systems: Slow motion of fluids relative to beds of spherical particles. *AIChE J., 4*, 197-201

[12] Brinkman, H. C. (1949). On the permeability of media consisting of closely packed porous particles. *Appl. Sci. Res., 1,* 81-86

[13] Glueckauf, E. (1955). Theory of chromatography. Part 9. The "theoretical plate" concept in column separations. *Trans. Faraday SOC., 51,*1540-1551.

[14] Liapis, A.I., McCoy, M.A. (1992). Theory of perfusion chromatography. *J. Chromatogr., 599*(1-2), 87-104

[15] Liapis, A.I., Xu, Y., Crosser, O.K., Tongta, A. (1995). "Perfusion chromatography". The effects of intra-particle convective velocity and microsphere size on column performance. *J. Chromatogr. A, 702*(1-2), 45-57

[16] Carta, G. (1995). Linear driving force approximation for intraparticle diffusion and Cconvection in permeable supports. *Chem. Eng. Sci., 50*, 887-889

[17] Shi, L., Sanyal, G., Ni, A., Luo, Z., Doshna, S., Wang, B., Graham, T. L., et al. (2005). Stabilization of human papillomavirus virus-like particles by non-ionic surfactants. *J. Pharm. Sci.*, *94*(7), 1538-51

[18] Perez-Almodovar, E.X., Glatz, B., Carta, G. (2012). Counterion effects on protein adsorption equilibrium and kinetics in polymer-grafted cation exchangers. *J. Chromatogr., A, 1253*, 83-93

[19] Bird, R.B., Stewart, W.E., Lightfoot, E.N. (2006). Transport Phenomena, second ed., Wiley, New York

[20] Perez-Almodovar, E.X., Wu, Y.G., Carta, G. (2012). Multicomponent adsorption of monoclonal antibodies on macroporous and polymer grafted cation exchangers. *J. Chromatogr., A, 1264,* 48-56.

[21] Ruthven, D.M. (1984) Principles of Adsorption and Adsorption Processes. Wiley, New York, NY, USA.

[22] LeVan, M.D., Carta, G., Yon, C.M. (1997). Adsorption and Ion Exchange Perry's Chemical Engineering Handbook. (7^{th} Edition). Sect. 16, McGraw-Hill, Columbus.

Chapter 4

Proteins and Virus-like Particle Adsorption and Recovery on Monolithic Columns and Recovery Properties on Perfusion Media

4.1 Introduction

Convective chromatographic stationary phases can be classified into two categories: perfusion chromatography media and monoliths [1]. Both stationary phases are designed to enhance the column efficiency and overcome the mass transfer resistance of large biomolecules by providing convective flow in large through pores or channels. In perfusion media only a small fraction of the mobile phase flows in the intraparticle pores, while in monoliths, all of the mobile phase flows within the matrix pores. Several analytical and process applications of perfusion chromatography media have been reported for proteins [2-7], plasmids [8], as well as for the capture step in a commercial process used to purify VLPs of recombinant HPV Type 11 major capsid protein L1 described by Cook et al. [9]. POROS HS 50, a strong cation exchanger designed for perfusion chromatography is employed in this process, where the VLPs are loaded onto a POROS HS 50 chromatography column and eluted with a salt gradient. It has been postulated that the convective pores are accessible to the VLPs thereby allowing VLP binding to occur throughout the beads. However, isocratic pulse response experiments and confocal laser scanning microscopy (CLSM) results in Chapter 2 show that although significant enhancement provided by convective transport can be observed for VLPs on

POROS HS 50 column under non-binding conditions, the adsorption of VLPs on POROS HS 50 beads was restricted to a thin superficial layer on the bead surface. Although the size of the macropores in POROS HS 50 beads may be large enough to accommodate VLPs with a 50 nm molecular radius, the bound VLPs on the pore surface appear to block the macropores (Fig. 2.16) and prevent the additional VLPs from reaching the particle core.

Monoliths are generally considered not favorable for the purification of smaller proteins when compared to porous particles due to their much smaller binding surface area caused by their larger pore size, and because the relatively fast diffusional transport of such proteins in porous media is not severely hindered [10]. However, as shown in Chapter 2 and 3, transport of biomolecules with very large size in conventional porous media or even in perfusion chromatography matrices is slow and severely hindered. Monoliths, on the other hand, provide large flow channels (2-5 μm in diameter [1]) that allow convective flow of the mobile phase through the whole matrix, as well as smaller pores inside the skeleton structure [11-13]. Silica monoliths are composed of a porous silica network and are typically employed in the separation of small organic compounds [14]. Polymer-based monoliths, prepared by different polymerization methods, have broader size distribution of the flow channels compared to silica monolith [15], and are used widely in the separation of large biomolecules and even cells [16-20]. Several studies have shown that no significant diffusional transport resistances exist for large molecular weight compounds in polymer based monoliths columns even at high flow rates, indicating that the performance of monoliths columns is generally independent of molecular size [21]. Thus, although the binding capacities are much smaller for proteins

due to smaller surface areas, monoliths have become a very useful tool for processing large biomolecules such as plasmid DNA and viruses because of the absence of mass transfer limitations. Monoliths columns operated under axial and radial flow conditions have been developed. The latter design has been chosen for the purpose of maintaining high volumetric flow rate with relatively low pressure, allowing higher speed of operation and lower column height comparing with axial flow columns with the same column volume [22, 23].

However, due to the random nature of the monolith pore network, the possible existence of dead-end or constricted pores within the structure is a potential disadvantage for polymer monolith columns. Such pores may affect product recovery as the adsorbate molecules can become trapped in the flow channels. For example, Rupar et al. [24] found that the recovery in the purification of *Potato virus Y* using monolith columns was only around 50%. Additionally, severe spatial heterogeneity in porosity and pore size may lead to uneven flow and, thus, poor chromatographic performance.

The objective of this work is three fold: (1) to determine the structural characteristics of a radial-flow monolith column; (2) to determine band broadening effects for proteins and VLPs on the monolith column under both non-binding and strong binding conditions and compare them with those seen for with POROS HS particles; and (3) to determine the adsorption and recovery properties of proteins and VLPs on the monolith column and compare them with those of POROS HS particles.

4.2. Materials and Methods

4.2.1 Materials

The resins used in this work, POROS HS 50 and POROS HS 20, are the same with those used in Chapter 2 and 3, and were purchased from Applied Biosystems (Life Technologies Corporation, Grand Island, NY). According to the manufacturer, both POROS HS particles are composed of a poly(styrene-divinylbenzene) backbone functionalized with strong cation exchange groups. The interior pore structure has a bimodal pore size distribution for both with smaller pores less than 50 nm and large pores up to 1,000 nm in diameter. The average particle diameters of the two resin samples are 52 and 23 μm, respectively, with a range of sizes from 35 to 75 and 15 to 33 μm, for POROS HS 50 and POROS HS 20, respectively (Fig. 2.3 and 3.1).

"Convective Interaction Media" (CIM) SO3-1 and QA-1 tube monolith columns were obtained from BIA Separation (Villach, Austria). This SO3-1 monolith is a strong cation exchanger, consisting of a sulfonyl-functionalized polymeric backbone while the QA-1 monolith is an anion exchanger based on quaternary ammonium ion functionality. Both monoliths are shaped as a hollow cylinder and are contained in a polypropylene housing which allows the mobile phase to run in a radial direction, from the outer to the inner surface. A schematic of the CIM SO3-1 column is shown in Fig. 4.1. The outer and inner diameters of the monolith used in this work are 18.6 and 6.7 mm, respectively, and its length is 4.2 mm; the total bed volume is 1 mL. According to the monolith manufacturer, the porosity, ε, and the specific surface area, A, of the monolith, determined by mercury intrusion porosimetry, are 0.63 and 8.49 m^2/g, respectively.

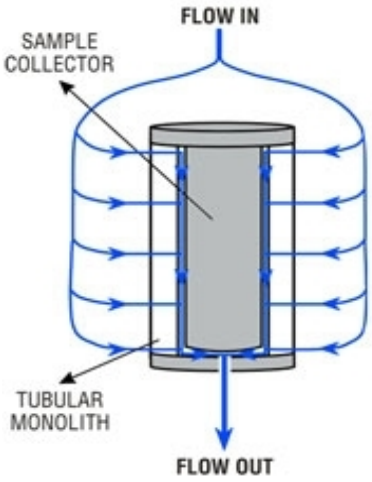

Figure 4.1. Schematic and flow distribution in CIM SO3-1 tube monolith column [25].

Proteins and VLPs used in this work are the same with those described in the previous chapters. Chicken egg white lysozyme (Lyo) and bovine thyroglobulin (Tg) are obtained from Sigma Chemical Co. (St. Louis, MO) and used as received. A monoclonal antibody (IgG) with pI 8.6, was purified to >99% monomer with a GE Healthcare (Piscataway, NJ) Superdex 200 column as reported by Tao et al. [26]. VLPs of recombinant HPV Type 11 capsid protein L1 were provided by Merck & Co., Inc. (West Point, NJ). The process used to recover and purity the VLPs from S. Cerevisiae was described by Cook et al. [9]. All other chemicals were obtained from Fisher Scientific (Pittsburgh, PA, USA). The hydrodynamic radius, r_s, of the test solutes used was determined with a DynaPro NanoStar dynamic light scattering (DLS) detector (Wyatt Technology Corporation), which gave values of 5.5 ± 0.5, 8.5 ± 1.0, and 50 ± 10 nm, for IgG, Tg, and VLP samples, respectively. The corresponding solution diffusivities, D_0, at 25 °C are 4.0×10^{-7}, 2.6×10^{-7}, and 3.5×10^{-8} cm^2/s are consistent with the respective molecular masses. The hydrodynamic radius of Lyo, estimated based on its known D_0-value of 1.1×10^{-6} cm^2/s is 2.3 nm. All chromatography and adsorption experiments were

conducted at room temperature, 25 °C unless otherwise indicated. Protein solutions were prepared in aqueous buffers containing 10 mM Na_2HPO_4 at pH 7.0 for Lyo, 20 mM CH_3COONa at pH 5.0 for IgG and Tg, and in 50 mM phosphate buffer at pH 7 for the VLPs. 1.25 M NaCl was added for non-binding conditions. The non-ionic surfactant Polysorbate 80 (PS-80, obtained from Amresco, Solon, OH) was added to the VLP solutions at the 0.015 wt% level to improve stability [27]. These solutions remained stable for several days at 4 °C and for at least one day at room temperature.

4.2.2 Methods

Most of the methods used in this work are essentially the same as those previously presented in Section 2.2.2 and are described here only succinctly. The internal structure of POROS HS resins was determined by transmission electron microscopy (TEM) as described and discussed in detail in Chapter 2 and 3. Both TEM and scanning electron microscopy (SEM) were used to determine the internal structure of the monolith column. At the conclusion of experimental runs, both the CIM SO3-1 and QA-1 columns were sacrificed and opened to remove the monolith matrix from the housing. Samples from different part of the monolith matrix were collected by cutting small blocks of, approximately 3 mm × 3 mm in size with a scalpel. The samples were fixed on aluminum pin stub specimen mounts (Ted Pella. Inc, Redding, CA) using double faced adhesive tape, and imaged with a Zeiss Sigma HD VP scanning electron microscope. TEM were obtained by embedding the dehydrated samples in LRWhite (London Resin Company, London, UK), followed by sectioning with an ultramicrotome to produce 80 nm slices, which were then imaged with a Jeol 100 CX transmission electron microscope.

Inverse size exclusion chromatography (iSEC) was used to determine the accessible intraparticle volume of the monolith column. For this purpose, glucose and dextran samples with molecular mass between 4 and 2000 kDa, obtained from Spectrum Chemical Manufacturing Co. (Gardena, CA), were injected onto the monoliths column. The column was operated at a flow rate of 0.5 mL/min with a mobile phase consisting of 1 M NaCl in 10 mM Na_2HPO_4 at pH 7.0. 10-20 μL injections of 5 g/L solution of each probe solved in the mobile phase were made with a Waters HPLC system. The dead volume of the system was measured based on the first moment obtained without the column. The measurement of porosities and apparent pore size distribution of flow packed POROS HS columns are described and discussed in detail in Chapters 2 and 3.

Isocratic pulse response experiments were conducted on the monolith SO3-1 column as follows. Under non-binding conditions, proteins and VLP samples were injected at flow rates of 0.2 to 4 mL/min using an AKTA Explorer 10 unit (GE Healthcare, Piscataway, NJ). The injected samples were 20 μL in volume, made by dissolving each protein and VLP in pH 7.0 phosphate buffer with 1 M NaCl for Lyo, IgG and Tg and in 1.5 M NaCl for the VLPs with detection at 280 nm. The same measurements conducted on POROS HS columns are described in Chapter 2 and 3 were made and the ensuing peaks were analyzed by the moment method as detailed by Carta and Jungbauer [28].

Frontal analysis experiments of Lyo and IgG were conducted with the 0.5 cm × 5 cm flow packed POROS HS columns and monolith column at flow rates of 0.5, 1 and 2 mL/min, using an AKTA Explorer 10 unit from GE Healthcare. The column was first equilibrated with 10 mM Na_2HPO_4 at pH 7.0 for Lyo and 20 mM CH_3COONa at pH 5.0 for IgG, followed by loading corresponding protein sample onto the column until a

complete breakthrough curve was obtained. Detection of proteins breakthrough and subsequent elution was by UV at 280 nm. The amount of protein actually bound to the columns was obtained from the breakthrough curves by integrating the outlet concentration profile.

Load-wash-elute experiments of VLPs on packed POROS HS columns and monolith column were conducted to determine the recovery of VLPs. For this purpose, a VLPs sample was first buffer-exchanged into the binding buffer consisting of 200 mM MOPS and 250 mM citrate at pH 7.0. The feed concentration of VLP was determined from the AKTA UV detector obtained by flowing the sample through in a column by-pass configuration. Columns were first cleaned by 0.5 M NaOH and equilibrated with the binding buffer. The entire load/elute process was performed at a flow rate of 0.2 mL/min to achieve the same residence time of 4.7 min typical of how the actual process is operated. A certain volume of the VLP sample was first loaded. The column was then washed with 10 column volume of HS wash buffer (50 mM MOPS, 750 mM NaCl and 5 mM Na_3PO_4 at pH 7.0), and eluted with a linear gradient from 100% HS wash buffer to 100% elution buffer (50 mM MOPS, 1500 mM NaCl and 5 mM Na_3PO_4 at pH 7.0) over a 10 CV and 100% elution buffer for 2 additional CVs. The amount of VLPs actually bound to the columns was obtained from the breakthrough curves by mass balance using the concentration of VLPs at the outlet and feed solution. The amount of VLPs recovered was obtained based on the elution peak area.

4.3 Results and Discussion

4.3.1. Monolith Structure

The CIM SO3-1 tube monolith used in this dissertation was opened for determination of the internal structure after completing other experiments. A new CIM QA-1 tube monolith column, a strong anion exchange column which has similar physical structure as CIM SO3-1 tube monolith was also sacrificed for this purpose. Fig. 4.2 shows side-by-side the SEM images of the two monoliths from samples taken at different locations. The images from samples taken from the top surface (Fig. 4.2 top row) and the interior (Fig. 4.2 middle row) of the monolith show similar structures for both columns. These samples show that both monoliths have a microgranular matrix structure consisting of interconnected nodular about 0.5 to 1 μm in diameter, with a distribution of large flow channels of 1000-2000 μm in diameter as well as much smaller channels in between. Compared with POROS HS particles, the large flow channels in the monoliths have larger size, which is considered to be an advantage of transport of large biomolecules such as VLPs. However, the samples taken from the side surface of the matrix (Fig. 4.2 bottom row), where the mobile phase flows into the monoliths under normal operating conditions, show a dense 'skin' layer that covers a majority of the surface area, leaving very few open pores on the surface. The reasons why this 'skin' surface layer is present are not known. A possibility is that the skin layer is there by design for the purpose of attaining better flow distribution; however, it is obvious that this layer may hinder transport of large molecules into and out of the monolith.

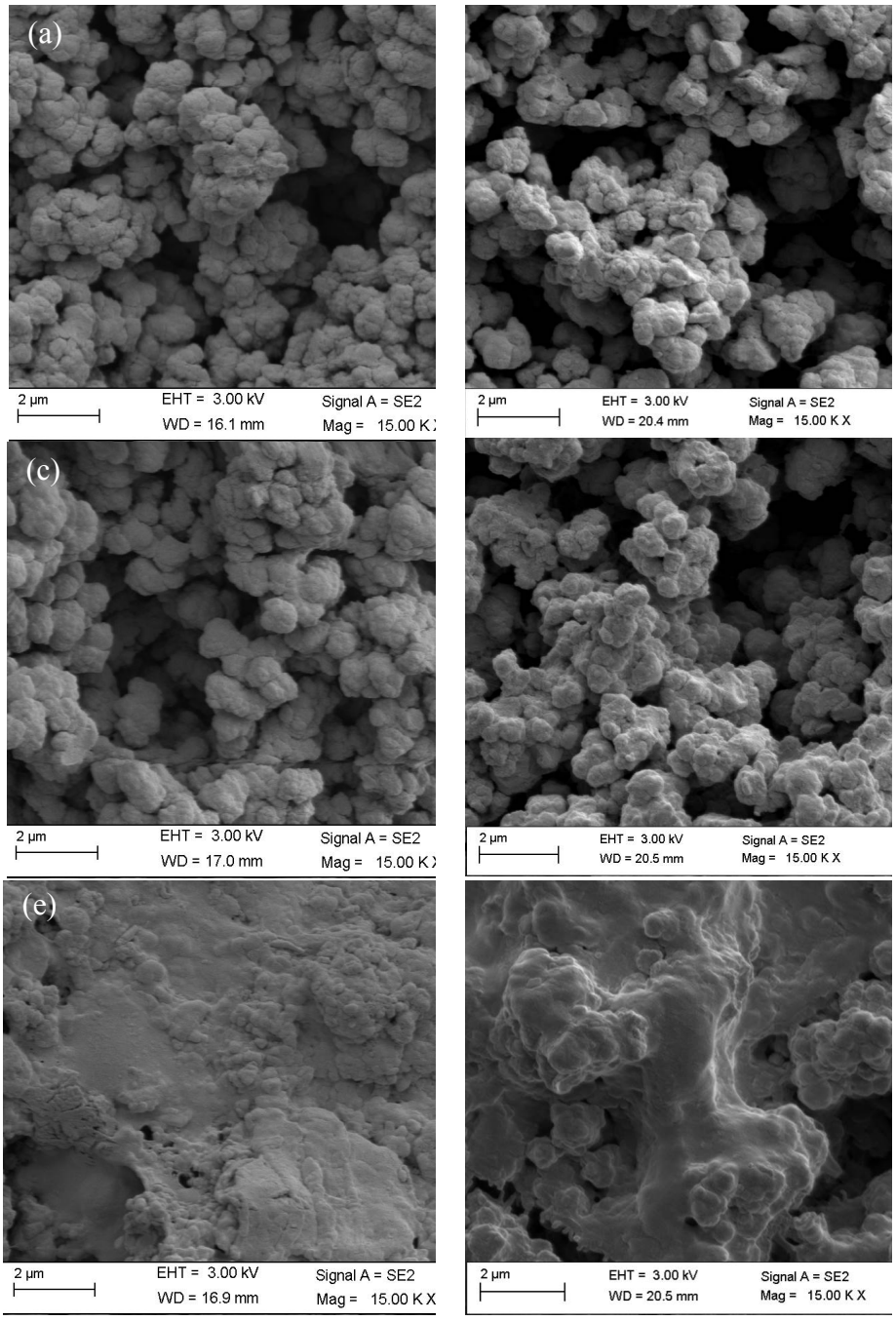

Figure 4.2. SEM images of CIM SO3-1 monoliths column (left column) and QA-1 monoliths column (right column) samples obtained from the surface on the top of the monoliths (top row), the interior of the monoliths (middle row) and the surface of the side of the monolith (bottom row) at 15K magnification.

TEM images of the monolith columns (Fig. 4.3a and b) were also obtained to compare with that of POROS HS resins (Fig. 4.3c and d). The darker area in the images represents the backbone of the monolith or POROS HS particles, and the lighter grey area represents LRWhite inside the pores. The very bright spots are imperfection caused by sectioning or the incomplete penetration of LRWhite. Both monolith samples show very large flow channels of ~ 2500 nm as well as smaller pores between the backbone agglomerates. The size of the large flow channels in the monoliths is much greater than that of the through-pores inside the POROS HS particles.

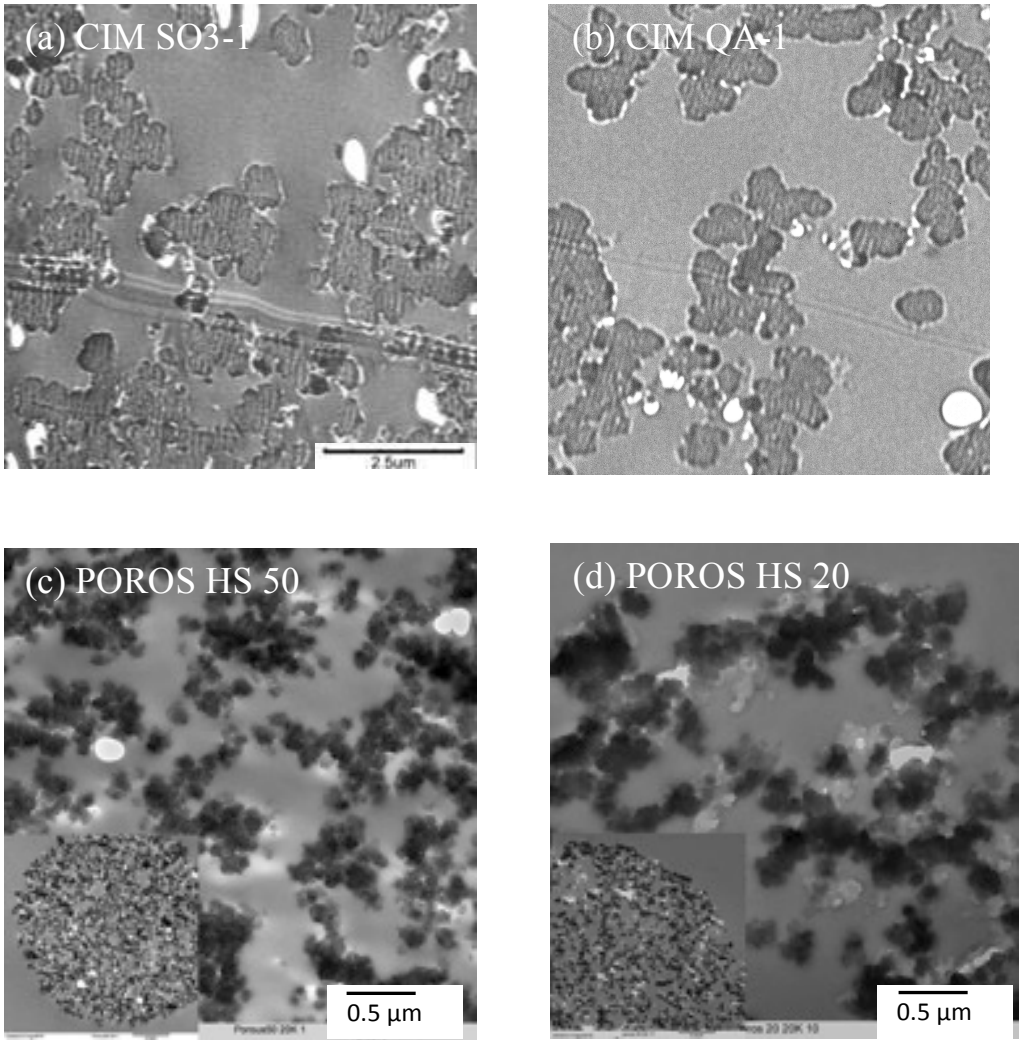

Figure 4.3. TEM images of monolith columns (top row): (a) CIM SO3-1 and (b) CIM QA-1 at 5K magnification; and POROS HS particles (bottom row): (c) POROS HS 50 and (d) POROS HS 20 at 20K magnification. Note the different scale bars for the top and bottom images.

Figure 4.4 shows a plot of pressure drop vs. flow rate Q for the SO3-1 monolith and for a POROS 50HS column with the same volume (1 mL) but a 0.5 cm diameter × 5 cm length aspect ratio. The hydraulic permeability of the monolith was calculated from the pressure drop measurement using Darcy's law [30]:

$$B_0 = u_{\text{ave}} \eta \frac{d_{\text{bed}}}{\Delta P} \tag{4.1}$$

where u_{ave} is the average superficial velocity, η the viscosity of the mobile phase, $d_{\text{bed}} = \frac{1}{2}\left(d_{\text{c,o}} - d_{\text{c,i}}\right)$ the thickness of the monolith, and ΔP the pressure drop. u_{ave} is calculated by the following equation [29]:

$$u_{\text{ave}} = \frac{Q}{\pi \cdot L_0} \frac{\ln\left(\frac{d_{\text{c,o}}}{d_{\text{c,i}}}\right)}{\left(d_{\text{c,o}} - d_{\text{c,i}}\right)} \tag{4.2}$$

where Q is the flow rate, L_0 the monolith length, $d_{\text{c,o}}$ and $d_{\text{c,i}}$ are the outer and inner diameter of the monolith, respectively. The permeability of the monolith is B_0 = 1.21 ± 0.04 × 10^{-14} m^2, which is consistent with the reported value of 1.11 × 10^{-14} m^2 for a disk-shaped monolith from the same manufacturer [31]. The permeability of the POROS HS 50 column is 1.24 × 10^{-12} m^2. Although, the permeability is 100 times lower for the monolith, the pressure drop is approximately the same in the two columns at the same volumetric flow rate because of the different geometries.

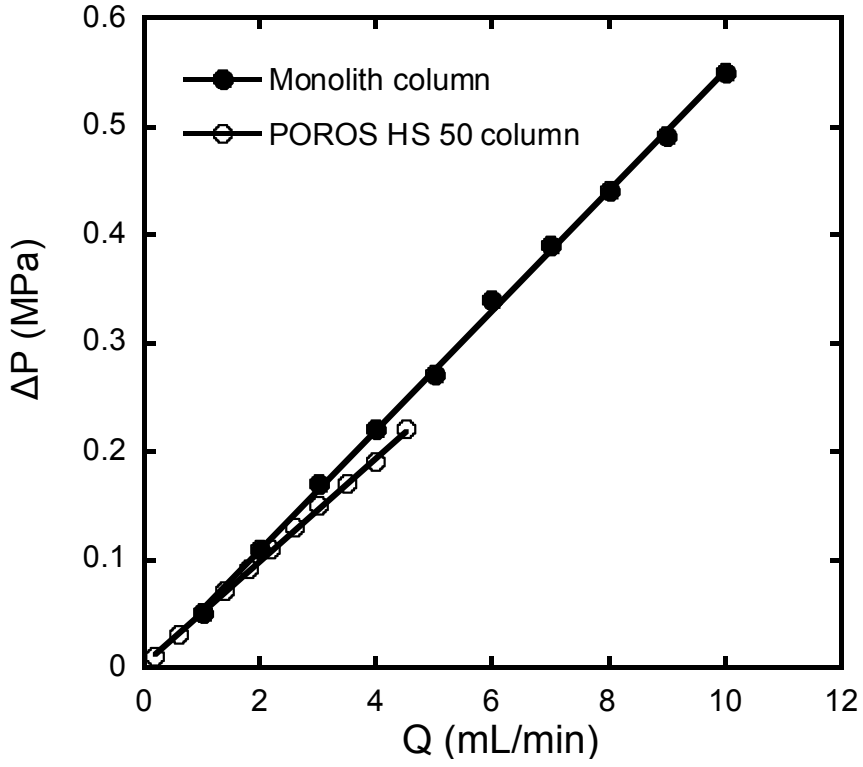

Figure 4.3. Pressure drop (ΔP) vs. flow rate (Q) for the monolith column and the 0.5 cm × 5.0 cm flow-packed POROS HS 50 column, the two columns have the same volume (1 mL).

An equivalent particle diameter, d_{eq}, of the monolith matrix was estimated by using Happel's free surface model, given by the following equation [30]:

$$\Delta P = 18\frac{\eta u d_{bed}}{d_{eq}^2}(1-\varepsilon)\left[\frac{3+2(1-\varepsilon)^{5/3}}{3-\frac{9}{2}(1-\varepsilon)^{1/3}+\frac{9}{2}(1-\varepsilon)^{5/3}-3(1-\varepsilon)^2}\right] \tag{4.3}$$

d_{eq} represents the diameter of particles packed in a column having the same ε and hydraulic permeability as the monolith. A value of d_{eq} = 1.1 μm was obtained based on the monolith porosity ε = 0.63 given by the monolith manufacturer. This value is

consistent with that reported by Tallarek et al. [32], and consistent with the microgranular structure seen by SEM (see Fig. 4.2). The effective diameter of the flow channels in the monolith was estimated by the following equation [33]:

$$B_0 = \varepsilon \frac{d_{ch}^2}{32} \tag{4.4}$$

which assumes that the flow channels are straight cylinders. A value of $d_{ch} = 0.74$ μm was obtained. This value is somewhat smaller than the diameter of the macropores in the monolith (~1.3 μm as determined by the monolith manufacturer using mercury intrusion porosimetry), likely as a result of the tortuosity of the actual flow paths in the monolith.

Fig. 4.4 shows the elution peaks obtained for different dextran probes and glucose in the monolith. The eluted peaks are shifted horizontally to account for the extra column volume. However, an additional "dead volume" exists within the monolith housing. As a result, the elution volumes are larger than the actual monolith volume of 1 mL. Using the retention volume of glucose as a basis, the total void volume, which includes both the monolith pore volume and the housing dead volume, is 1.33 mL. Since the monolith pore volume is 0.63 mL, the dead volume in the housing is 0.70 mL. This volume is actually larger than the monolith volume and is likely to be the cause of the broad, tailing peaks obtained in these experiments. Nevertheless, the important result is that the difference between elution peaks for high and low molecular mass dextrans are very small, indicating that the monolith pores are sufficiently large to prevent size exclusion effects. A slightly higher elution volume is seen only for glucose and low molecular weight dextrans suffesting that some smaller pores axtually exist in the monolith.

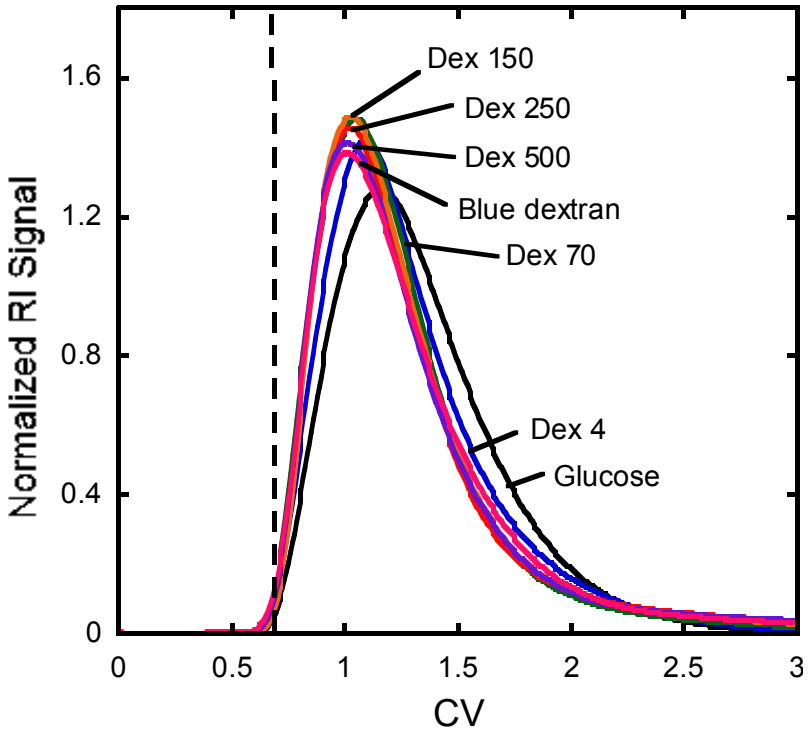

Figure 4.4. Elution peaks for dextran probes and glucose obtained for the monolith at a flow rate of 0.5 mL/min. The dash line represents the housing dead volume (0.7 mL)

Figure 4.5 shows the isocratic elution peaks obtained for Lyo, IgG, Tg, VLPs, and NaCl with the SO3-1 monolith at different flow rates for non-binding conditions (1.5 M NaCl, pH 7.0). It can be seen that IgG, Tg and the VLPs elute essentially at the same volume and that the peak width is not affected by flow rate. Lyo elutes slightly later and the peak is slightly broader than those of IgG, Tg, and the VLPs. Finally, NaCl elutes substantially later and the peak is definitely broader. The results suggest that some small pores exist in the monolith that are accessible by NaCl but not by larger proteins. More importantly, the absence of any flow rate effect on peak broadening confirms that for

these non-binding conditions there are no significant diffusional mass transfer effects and that peak broadening is controlled by hydrodynamic effects.

The recovery from the monolith column under non-binding conditions was obtained based on the eluted peak area in Fig. 4.6 for each proteins and VLPs to determine if the molecules are physically trapped inside the monolith. For proteins, recover was near 100%, indicating the flow channels inside the monolith are large enough for proteins to flow through. However, the recovery of VLPs from the monolith column is only 52% even under non-binding conditions, which is significantly lower than that obtained on POROS HS columns (79% and 78% for POROS HS 50 and POROS HS 20, respectively). This result suggests that although the large flow channels in monolith have much bigger size than the through-pores in POROS HS particles, there might be some small channels in the monolith that trap the VLPs causing the lower recovery under non-binding conditions.

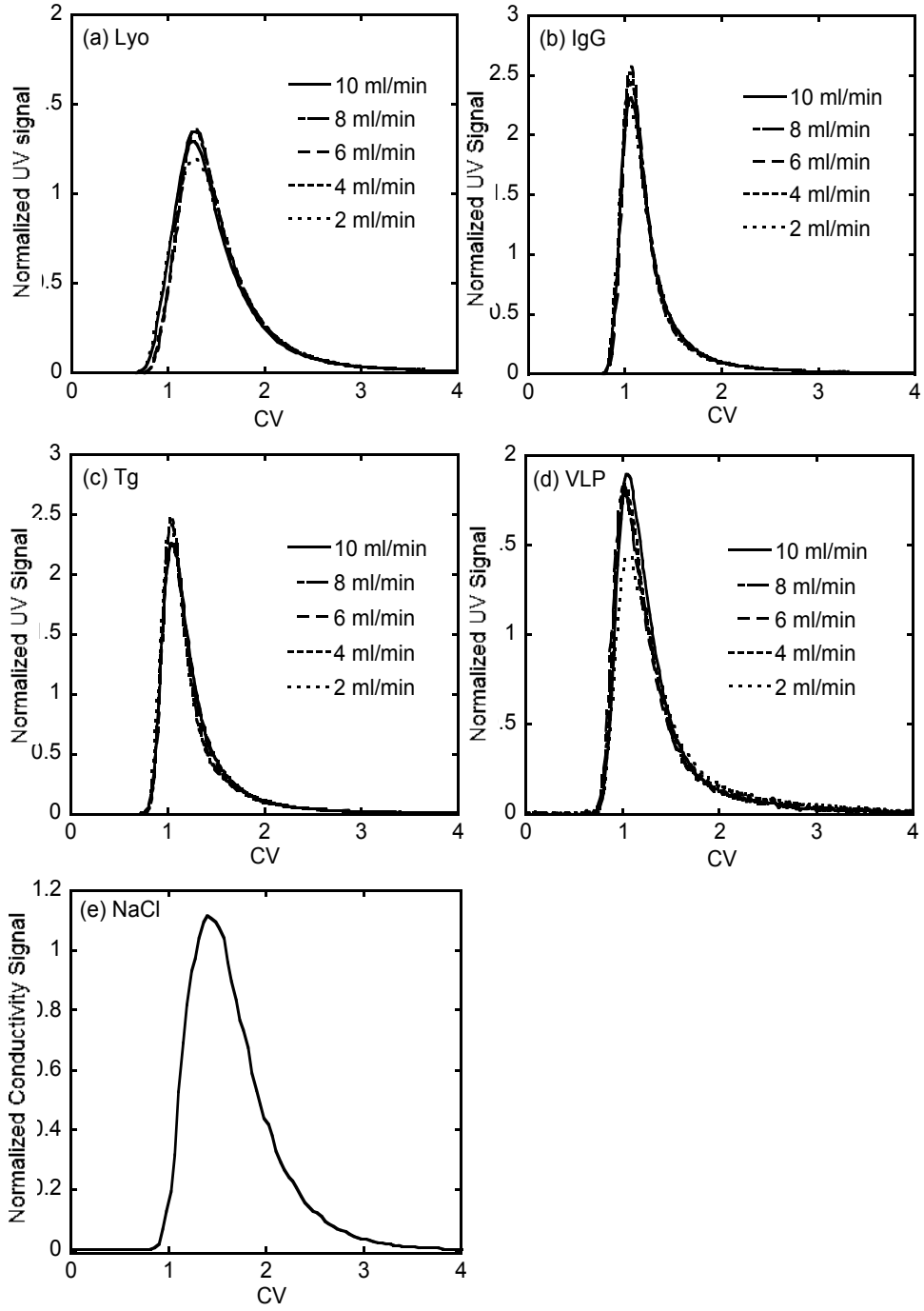

Figure 4.5. Chromatographic peaks of (a) Lyo, (b) IgG, (c) Tg, (d) VLP and (e) NaCl, obtained for the SO3-1 monolith column under non-binding conditions. CV values are shown after subtracting the extra column volume but not the housing dead volume of 0.7 CV.

Figure 4.6 shows the first moment of the elution peaks of dextran probes, proteins and VLPs obtained from Fig. 4.4 and 4.5. The following equation is used to calculate the μ-value [28]:

$$\mu = \frac{\int_0^\infty \text{signal} \times CV \times d(CV)}{\int_0^\infty \text{signal} \times d(CV)} \tag{4.5}$$

In this plot, an initial rapid decrease of μ occurs as rs increases, but then declines much more gradually for r_s > 10 nm, which is similar to the trend in Fig. 3.4. This result confirms that smaller molecules, such as NaCl, Lyo, glucose and dextran 4, have larger elution CV value, indicating there is less exclusion for these probes compare to others with larger molecular weights.

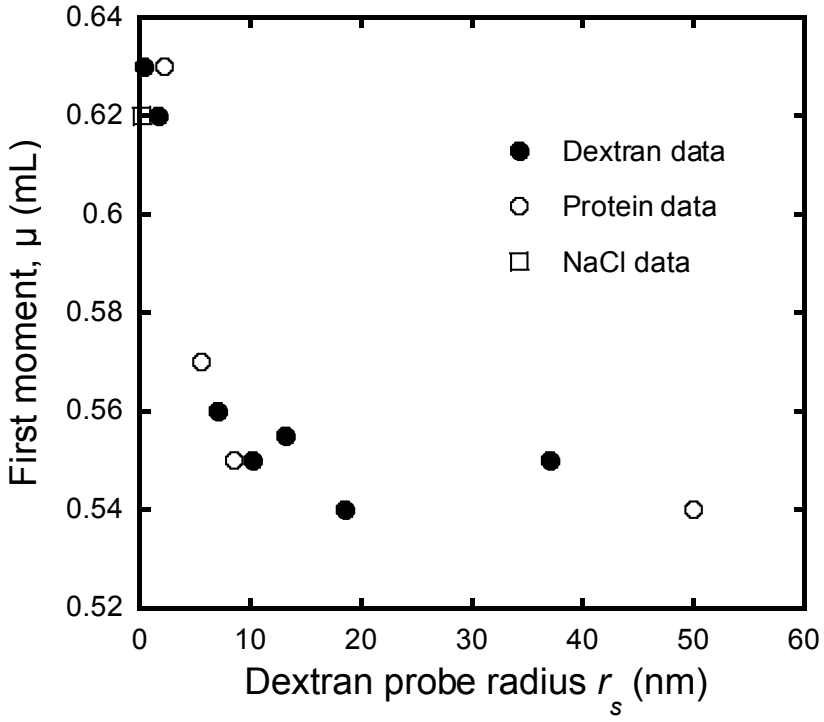

Figure 4.6. First moments of the elution peaks in Fig. 4.4 for the SO3-1 monolith vs. the probe radius r_s. The first moment is calculated based on the elution CV values after subtracting the extra column volume and the housing dead volume of 0.7 mL.

4.3.2. Protein Adsorption

Figure 4.7 compares the breakthrough curves obtained for LYO and IgG for the SO3-1 monolith column, the POROS HS 20 column, and the POROS HS 50 column with the same volume (1 mL) at flow rates of 1, 2 and 4 mL/min under strong binding conditions (10 mM Na_2HPO4, pH 7.0 for Lyo and 20mM CH_3COONa, pH 5.0 for IgG). For the monolith (Fig. 4.7a and b), neither protein shows a significant effect of flow rate indicating that mass transfer resistances are absent. However, both POROS HS 20 and 50 columns (Fig. 4.6c, d and e, f), show breakthrough curves that become increasingly shallower as the flow rate is increased. This effect is much more pronounced for POROS

HS 50, because of its larger particle size compared to POROS HS 20, and for IgG compared to Lyo, because of its smaller diffusivity. Interestingly, Lyo shows a shallower breakthrough curve than for IgG also on the monolith column. Actually, closer examination of these curves on the expanded scale of Fig. 4.8 shows that a small but significant flow rate dependence exists for Lyo. We thus conclude that the shallower breakthrough curve is a result of mass transfer resistances associated with transport of this smaller protein in smaller pores that are apparently present in the monolith as shown by the iSEC and isocratic elution peaks under non-binding conditions.

Figure 4.9 compares the equilibrium binding capacity (EBC) of LYO and IgG obtained by mass balance integrating the breakthrough curves for the monolith and POROS columns. For all three columns, the EBC is, as expected, nearly independent of residence time and much higher for the POROS columns compared to the monolith as a result of the lower surface area available for binding in the monolith.

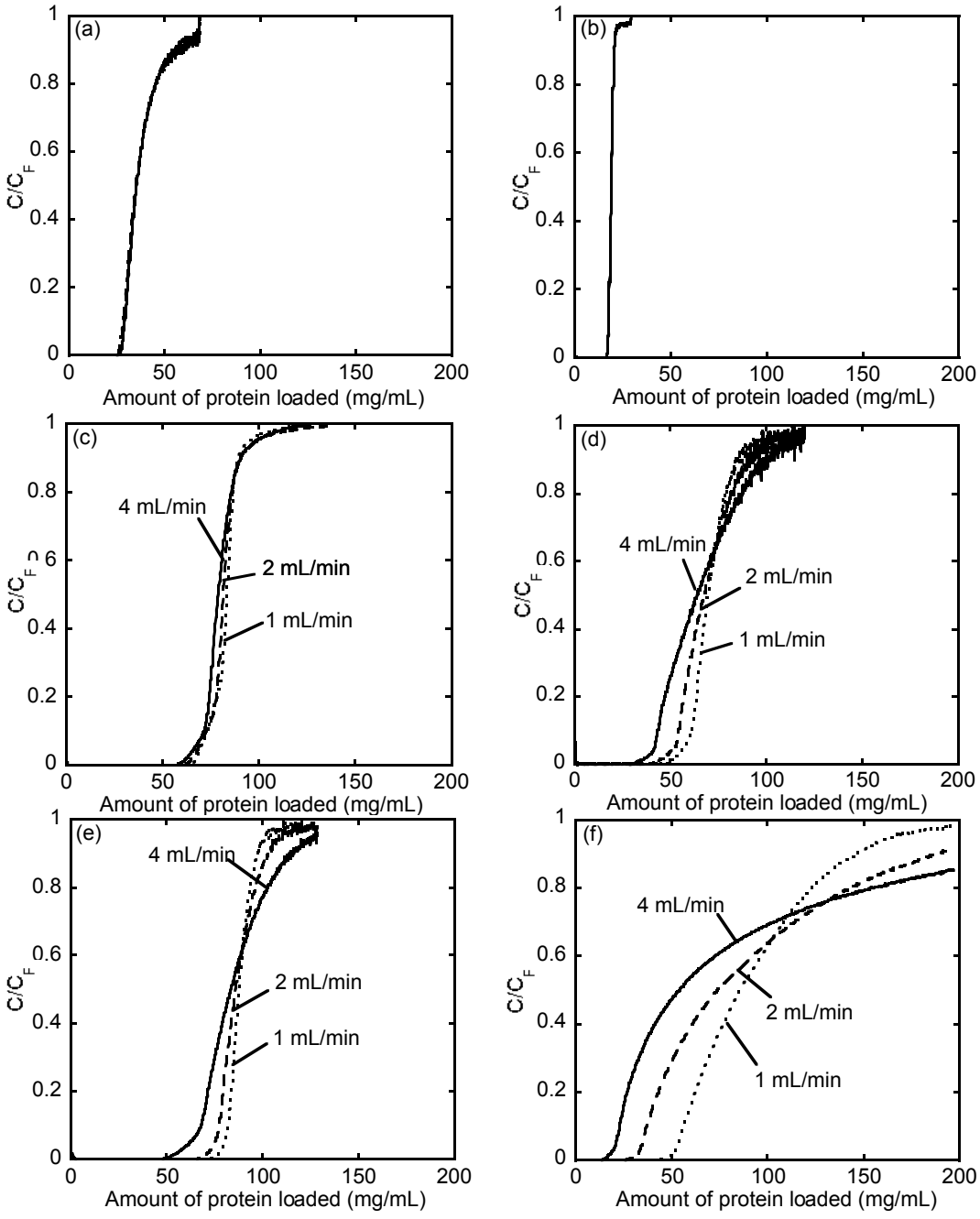

Figure 4.7. Breakthrough behavior of Lyo (left column) and IgG (right column) on the SO3-1 monoliths column (a and b), the POROS HS 20 column (c and d), and the POROS HS 50 column (e and f). The feed concentration C_F is 1 g/L for the monolith and POROS HS 20 columns, and 1.5 g/L for the POROS HS 50 column.

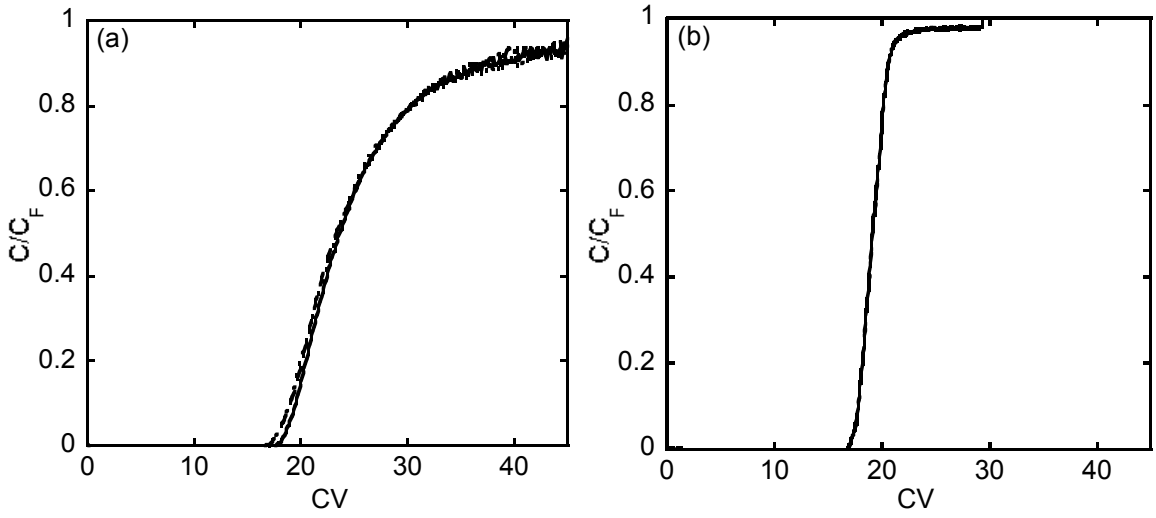

Figure 4.8. Breakthrough behavior of (a) Lyo and (b) IgG on monolith column on expanded scale of Fig. 4.7a and b.

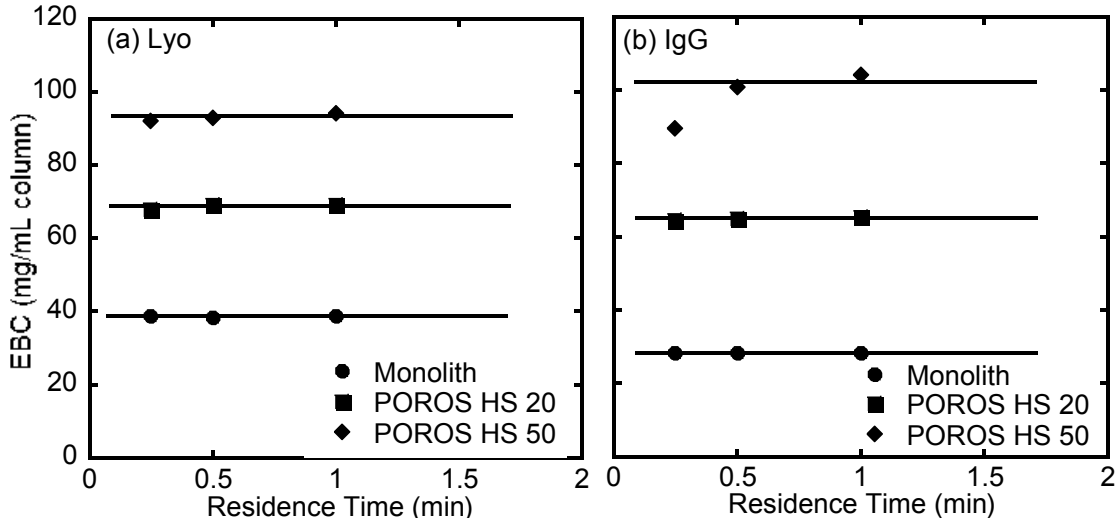

Figure 4.9. EBC of (a) Lyo and (b) IgG vs. residence time on monolith, POROS HS 20, and POROS HS 50 column. The slight decrease of EBC for the POROS HS 50 column at the lowest residence time is due to the incomplete breakthrough.

The dynamic binding capacity (DBC) obtained by mass balance at 10% of breakthrough of LYO and IgG on the monolith and POROS columns is plotted in Fig. 4.10. The DBC of both POROS columns residence time decreases, while the DBC of the monolith column remains the same. The decrease is more pronounced for POROS HS 50, because of its larger particle size, and for IgG, because of its smaller diffusivity. From a practical viewpoint, it is clear that for protein capture, the POROS columns perform better than the monolith over the range of residence times investigated experimentally as a result of the higher EBC of the POROS resins compared to the monolith column. As a result of the high EBC, even if the DBC decreases at lower residence times, the usable capacity of the POROS columns is generally higher than for the monolith. Only below 0.2 min residence time, does the monolith DBC become comparable to the POROS HS 50 DBC for IgG. Much smaller residence times would be needed to the POROS HS 20 DBC to become smaller than that of the monolith.

The results of $DBC_{10\%}$ for Lyo and IgG on POROS HS columns are compared with predictions based on the shrinking core model [34]. The relevant equations are given by Weber and Chackraborty [35] and are as follows:

$$\begin{aligned} n_{pore}\left(1-\tau_1\right) = & \frac{15}{2}\ln\left[1+\left(1-X\right)^{1/3}+\left(1-X\right)^{2/3}\right] \\ & -\frac{15}{\sqrt{3}}\tan^{-1}\left[\frac{2}{\sqrt{3}}\left(1-X\right)^{1/3}+\frac{1}{\sqrt{3}}\right] \\ & -\frac{n_{pore}}{n_{film}}\left[\ln\left(X\right)+1\right]+\frac{5\pi}{2\sqrt{3}}-\frac{5}{2} \end{aligned} \tag{4.5}$$

for constant pattern conditions or long residence times and:

$$n_{pore} = \frac{15}{2}\ln\left[1 + (1-Y)^{1/3} + (1-Y)^{2/3}\right] - \frac{15}{\sqrt{3}}\tan^{-1}\left[\frac{2}{\sqrt{3}}(1-Y)^{1/3} + \frac{1}{\sqrt{3}}\right]$$
$$- \frac{n_{pore}}{n_{film}}\left[\ln(Y) + 1\right] - \frac{15}{2}\ln\left[1 + (1-Y_0)^{1/3} + (1-Y_0)^{2/3}\right] \tag{4.6}$$
$$+ \frac{15}{\sqrt{3}}\tan^{-1}\left[\frac{2}{\sqrt{3}}(1-Y_0)^{1/3} + \frac{1}{\sqrt{3}}\right] + \frac{n_{pore}}{n_{film}}\left[\ln(Y_0) + 1\right]$$

with

$$n_{pore}\tau_1 = 5\left[1.5 - 1.5(1-Y_0)^{2/3} - \left(1 - \frac{n_{pore}}{5n_{film}}\right)Y_0\right] \tag{4.7}$$

for non-constant pattern conditions or short residence times. In these equations, X, τ_1, n_{pore}, and n_{film} are defined as follows:

$$X = \frac{C}{C_F} = \frac{Y}{Y_0} \tag{4.8}$$

$$\tau_1 = \frac{(ut/L) - \varepsilon}{(1-\varepsilon)q_F/C_F} \tag{4.9}$$

$$n_{\text{pore}} = \frac{60(1-\varepsilon)D_e}{d_p^2}\frac{L}{u} \tag{4.10}$$

$$n_{\text{film}} = \frac{6(1-\varepsilon)k_f}{d_p^2}\frac{L}{u} \tag{4.11}$$

For the conditions discussed here, the boundary layer mass transfer coefficient k_f can be determined by the following equations [36]:

$$Sh = \frac{1.09}{\varepsilon}Re^{0.33}Sc^{0.33} \tag{4.12}$$

where Sherwood number $Sh = \frac{k_f d_p}{D_0}$, Reynolds number $Re = \frac{\rho u d_p}{\eta}$ and Schmidt number $Sc = \frac{\eta}{\rho D_0}$. For both Lyo and IgG, the ratio

$$\frac{n_{\text{pore}}}{n_{\text{film}}} = \frac{5}{Bi} = \frac{5D_{\text{e}}}{k_{\text{f}} r_{\text{p}}} \tag{4.13}$$

is much less than unity even at the lowest flow rate, indicating intraparticle mass transfer resistance is dominant. Thus, at $X = 0.1$ (10% breakthrough), for constant pattern, where $n_{\text{pore}}\tau_1 > \frac{5}{2}\left(1 + \frac{n_{\text{pore}}}{n_{\text{film}}}\right)$, eq. 4.5 yields the following simplified result:

$$\tau_{1,10\%} = \frac{DBC_{10\%}}{EBC} \sim 1 - \frac{1.03}{n_{\text{pore}}} \tag{4.14}$$

The general solution given in eq. 4.6 is required for smaller values of the dimensionless time τ_1 and the corresponding calculations involve a trial and error procedure. However, the following approximation, valid up to $n_{\text{pore}}\tau_1 = 2.5$, derived from an empirical fit of the numerical results with X=0.1 and with negligible film resistance ($n_{\text{pore}} / n_{\text{film}} = 0$), can be used in lieu of the more complicated numerical calculation [37]:

$$\tau_{1,10\%} = \frac{DBC_{10\%}}{EBC} \sim 0.364 n_{\text{pore}} - 0.0612 n_{\text{pore}}^2 + 0.00423 n_{\text{pore}}^3 \tag{4.15}$$

The lines in Fig. 4.10 for Lyo and IgG are fitted through the data point at the longest residence time, where, according to the isocratic pulse response experiments, the intraparticle diffusional resistance dominates the mass transfer. For Lyo, the model described above predicts $DBC_{10\%}$ at different residence time very well, with a D_e-value of 1.1×10^{-7} cm^2/s for POROS HS 20 and 1.7×10^{-7} cm^2/s for POROS HS 50. In the case of IgG, however, the experimental data at short residence time for POROS HS 20 columns are clearly higher than the fitted model, indicating an enhancement of mass transfer at short residence time, or higher flow rate. Similar result can also be observed for POROS HS 50, although not as obvious as for POROS HS 20. Fig. 4.11 shows the plot of

$DBC_{10\%}/EBC$ vs. L/ur_p^2, where r_p is the average particle radius, for Lyo and IgG on both POROS HS columns. For IgG breakthrough curve on POROS HS 20, a D_e-value of 3.0×10^{-8} cm^2/s can well fit the long residence time data, which is consistent with the result in CLSM batch adsorption experiment where the flow effect is absent. A higher D_e-value of 7.2×10^{-8} cm^2/s is apparently fitted better for this flow rate. A ratio $\widetilde{D}_e/D_e = 2.4$ is obtained for this condition, which is consistent with the result of CLSM adsorption under flow condition (1000 cm/h). The HETP measurement under non-binding conditions gives a higher ratio of $\widetilde{D}_e/D_e = 2.9$, which is possibly due to lower hindrance from the bound IgG inside the pores. For POROS HS 50, D_e-values of 2.7×10^{-8} cm^2/s and 3.2×10^{-8} cm^2/s are used to fit the data point for the longest and shortest residence time, which yields a ratio of $\widetilde{D}_e/D_e = 1.2$ that is very close to the value obtained from CLSM adsorption experiments. Table 4.1 gives a summary for the D_e-values obtained from CLSM batch/flow adsorption and breakthrough curves for Lyo and IgG on both POROS HS columns, along with the value of $\widetilde{D}_e/D_e$.

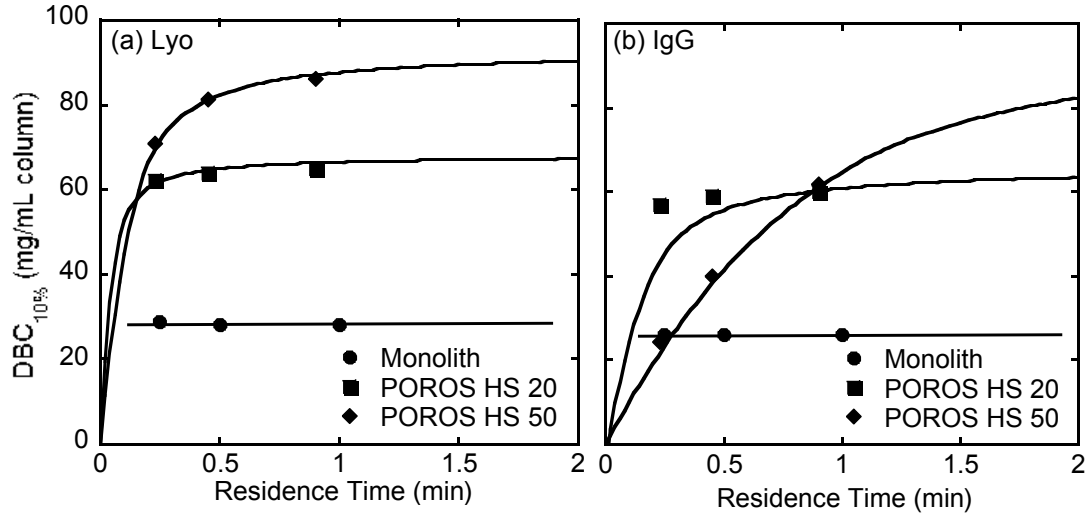

Figure 4.10. DBC at 10% breakthrough of (a) LYO and (b) IgG vs. residence time on monolith, POROS HS 50, and POROS HS 20 column. The solid lines are fitted by eq. 4.14 or 4.15.

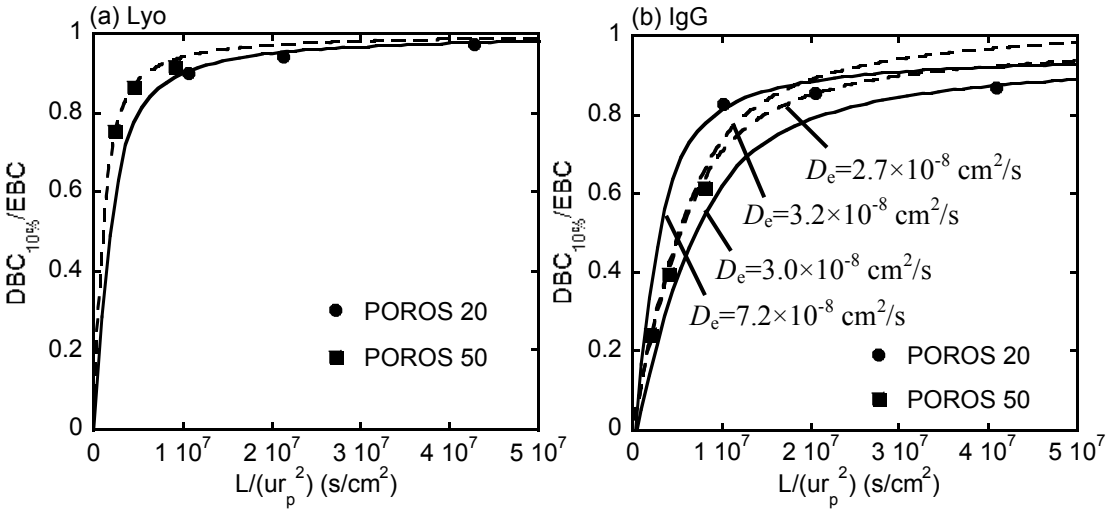

Figure 4.11. The ratio of $\mathrm{DBC}_{10\%}/\mathrm{EBC}$ plotted vs. L/ur_p^2 for Lyo and IgG breakthrough curves on POROS HS 20 and POROS HS 50 columns. The fitted model using eq. 4.14 or

4.15 is represented by solid lines for POROS HS 20 and dash lines for POROS HS 50, respectively.

Table 4.1. Summary of apparent pore effective diffusivities D_e obtained from CLSM batch/flow adsorption, breakthrough curves for Lyo and IgG and HETP measurements under non-binding conditions on both POROS HS columns.

		D_e ($\times 10^7$ cm^2/s)			
		Lyo		IgG	
		POROS HS 20	POROS HS 50	POROS HS 20	POROS HS 50
CLSM	Batch	N/A		0.31	0.25
	Flow			0.7	0.31
$\frac{DBC_{10\%}}{EBC}$	1 ml/min	1.1	1.7	0.30	0.27
	4 ml/min			0.72	0.32
HETP	$\tilde{D}_e/D_e$	~1	~1	2.9	1.2

Figure 4.12 and 4.13 show the load-wash-elute curves of Lyo and IgG, respectively, for the SO3-1 monolith column at 25 °C using different flow direction settings, which are described in Table 4.2. The column was first loaded with 1 mL of 1 g/L protein sample in binding buffer (10 mM Na_2HPO4, pH 7.0 for Lyo and 20mM CH_3COONa, pH 5.0 for IgG), then subsequently washed with 5 CV binding buffer. The bound proteins were then eluted with a linear gradient from 100% binding buffer to 100% elution buffer which containing 1500 mM NaCl over 20 CV. The entire process was first conducted at 4 mL/min flow rate using forward flow direction for load, wash and elution step as indicated by manufacturer. SEM images of the monolith (Fig. 4.2c) showed that

there is a dense “skin” layer on the outer surface where the mobile phase flows into the monolith. Since this structure may have effects on the transport and recovery of proteins and VLPs, further experiments were done reversing the flow direction as indicated in Table 4.2. For Lyo, no significant loss of injected protein was observed and nearly 100% recovery was reached in all four different flow direction settings. For forward flow load and forward flow elution (Fig. 4.12a), the elution peak comes out in the middle of the gradient. For forward flow load and reversed flow elution (Fig. 4.12b), a large portion of the proteins loaded come out at the beginning of elution, followed by the elution of the rest bound proteins later in the gradient. Similar elution profile was obtained for reversed flow load and forward flow elution (Fig. 4.12c). Compared with Fig. 4.16a, the earlier elution in Fig. 4.12b and c is likely due to the shorter transport path length in the elution step for the loaded protein. Finally, using reversed flow for both load and elution (Fig. 4.12d) shows similar elution peak with Fig. 4.12a. The nearly fully recovery of Lyo on monolith column indicating the hindrance effect of the skin layer on the monolith outer surface on Lyo transport and the physical trapping of Lyo in the smaller pores are not significant because of the small size of Lyo molecules.

Table 4.2. Flow direction setting in load-wash-elution experiments for VLP on monolith column.

Fig. 4.14a. Forward flow for load forward flow for elution	Fig. 4.14b. Forward flow for load reversed flow for elution
Load from outer to inner side Elute from outer to inner side 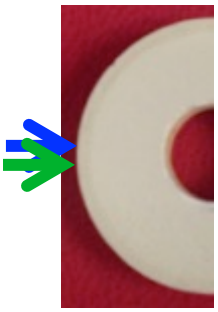	Load from outer to inner side Elute from inner to outer side 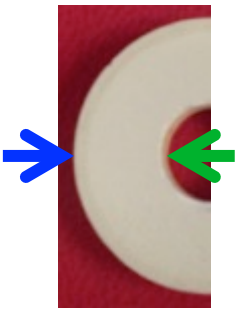
Fig. 4.14c. Reversed flow for load forward flow for elution	Fig. 4.14d. Reversed flow for load reversed flow for elution
Load from inner to outer side Elute from outer to inner side 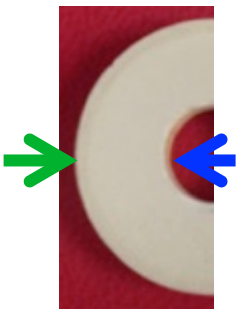	Load from inner to outer side Elute from inner to outer side 

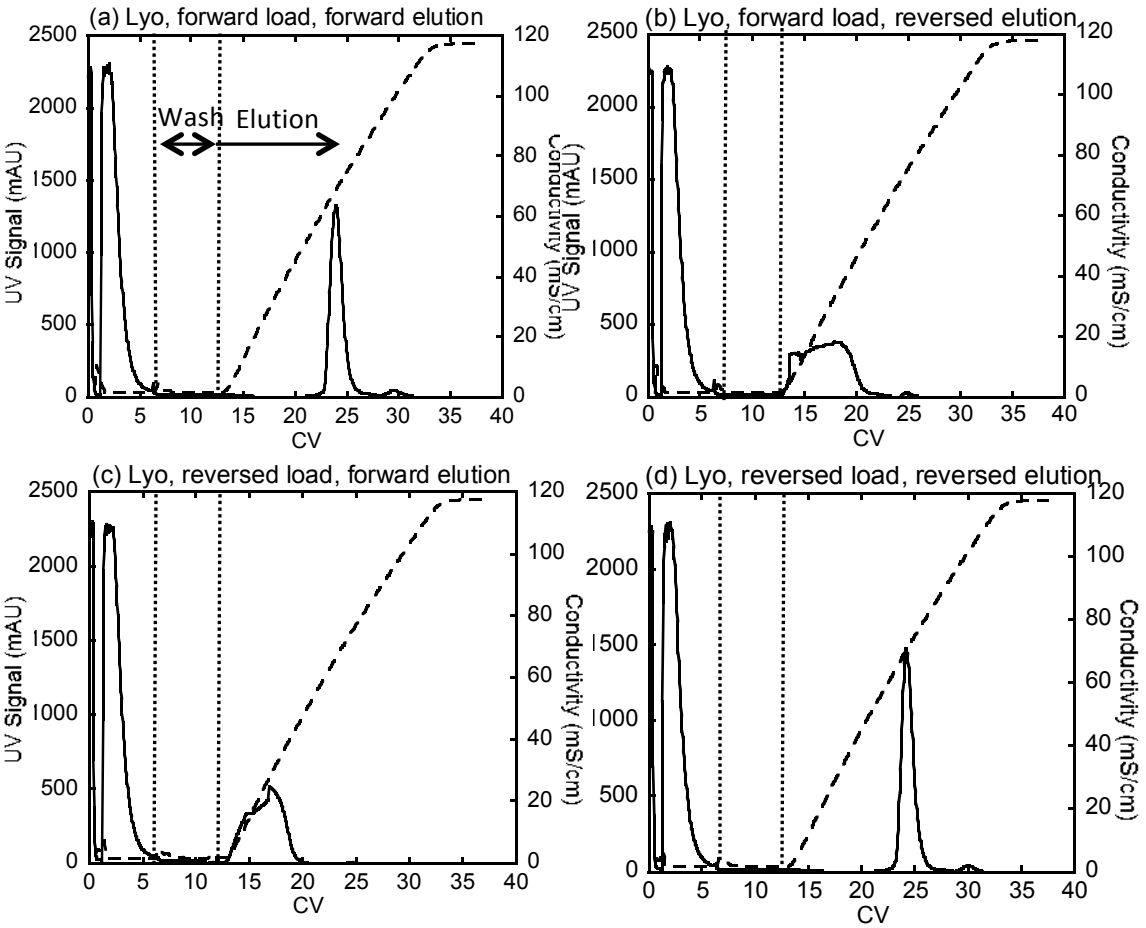

Figure 4.12. Representative load-wash-elute curves for Lyo on monolith column at room temperature operated as follows: (a) forward load and forward elution, (b) forward load and reversed elution, (c) reversed load and forward elution and (d) reversed load and reversed elution.

In the case of IgG, using forward flow load and forward flow elution (Fig. 4.13a) shows similar elution peaks and recovery with the result of using reversed flow load and reversed flow elution (Fig. 4.13d), where the elution peaks come out during the gradient and the recovery of loaded IgG are 88% and 89%, respectively. Compared with the elution peaks of Lyo (Fig. 4.12a and d), IgG peaks are relatively narrower, suggesting less accessible small pores volume for IgG than for Lyo. Meanwhile, the lower recovery of IgG may also indicates more trapping in the small pores due to its larger molecular size. Using forward flow load and reversed flow elution (Fig. 4.13b), the recovery reaches 97% and a double peak, including a large portion of IgG emerging at the beginning of the gradient as well as a smaller portion during the gradient, was obtained. Similar peak profiles were observed for reversed flow load and reversed flow elution (Fig. 4.13c), and the earlier elution of the loaded IgG is like due to the shorter transport path length compared to Fig. 4.13a and d. The recovery of both Lyo and IgG indicates the skin layer on the outer surface of the monolith has little effects on the transport of proteins, however, the existence of the smaller pores in monolith has effects related to the adsorbate molecular size.

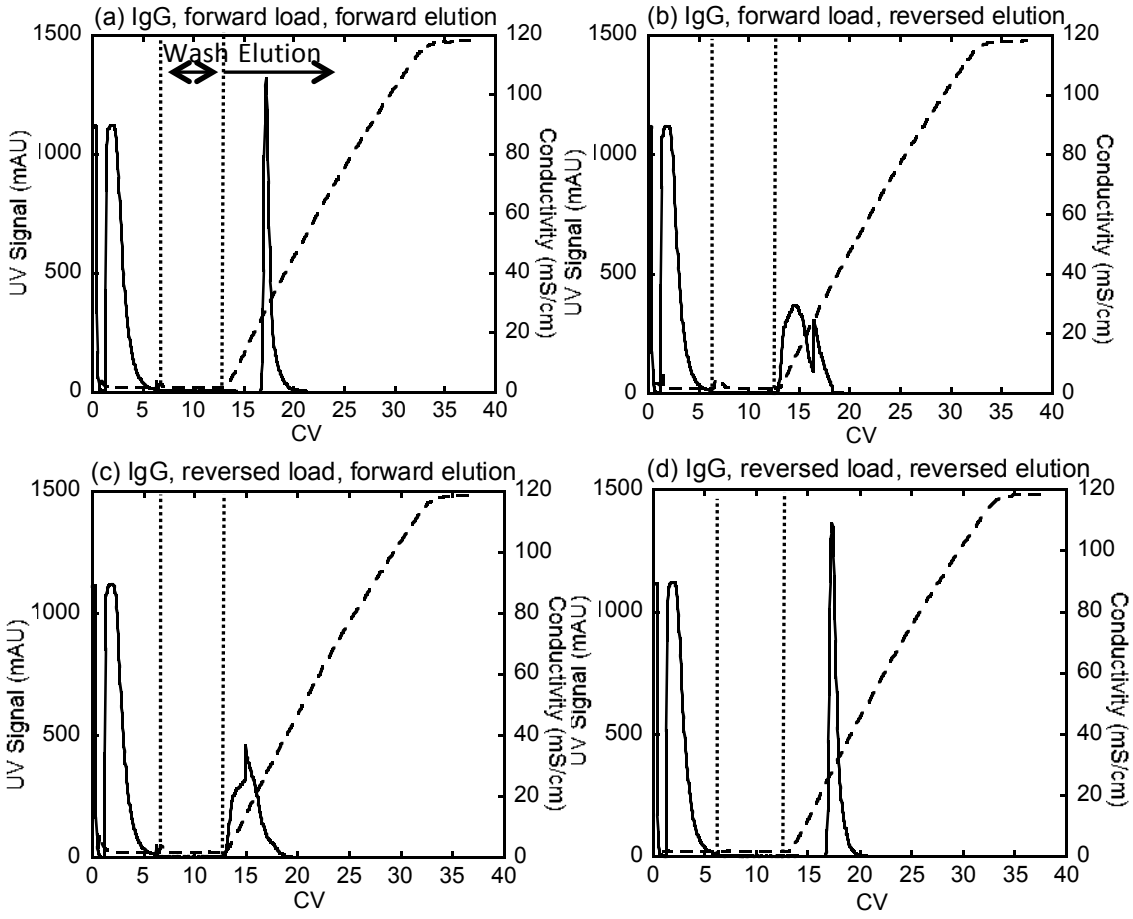

Figure 4.13. Representative load-wash-elute curves for IgG on monolith column at room temperature operated as follows: (a) forward load and forward elution, (b) forward load and reversed elution, (c) reversed load and forward elution and (d) reversed load and reversed elution.

4.3.3 VLP Adsorption and Recovery

The chromatograms of the load-wash-elute process of VLP on POROS HS packed columns at both 25 °C and 4 °C are shown in Fig. 4.14. The columns are first loaded with 5 mL of VLP samples in the binding buffer (200 mM MOPS and 250 mM sodium citrate at pH 7.0), then subsequently washed with 10 CV wash buffer (50 mM MOPS, 750 mM NaCl and 5 mM Na_3PO_4 at pH 7.0). The bound VLPs were then eluted with a linear gradient from 100% wash buffer to 100% elution buffer (50 mM MOPS, 1500 mM NaCl and 5 mM Na_3PO_4 at pH 7.0) over 7 CV and 100% elution buffer for 2 additional CVs. For the 25 °C run of POROS HS 50, the elution buffer was composed of only 1000 mM NaCl and the length of gradient is 10 CV. Fig. 4.15 shows the elution step of the corresponding load-wash-elute curves in Fig. 4.14. For 4 °C runs on POROS HS 50 (Fig. 4.15b) and POROS HS 20 (Fig. 4.15d), the elution peaks of VLPs both emerge at about the same conductivity, 75 mS/cm, during the gradient. Compared with VLPs elution conductivity of the 25 °C run on POROS HS 20 (Fig. 4.15c) that has the same final buffer composition and length of gradient, which is around 82 mS/cm, the lower temperature runs have lower elution conductivity. The even higher elution conductivity (95 mS/cm) of the 25 °C run on POROS HS 50 (Fig. 4.15a) is partially caused by the shallower elution gradient. The recovery of the bound VLP from the columns are obtained based on the ratio of the amount of eluted VLP from the columns, which is determined from the eluting peak area, and the total amount of VLP loaded onto the column. For POROS HS 50 (Fig. 4.15a), the recovery of VLP from the column is determined to be 44% under 25 °C, in other words, a substantial amount of adsorbed VLPs cannot be eluted from the

resin. This result is consistent with the CLSM observations of VLP desorption in Chapter 2, where the desorption of VLPs from POROS HS 50 particles stopped after a limited amount was desorbed. POROS HS 20 (Fig. 4.15c) shows slightly improved recovery comparing with POROS HS 50, with a recovery of 45% at 25 °C. At 4 °C, both POROS HS columns show slightly improved VLPs recovery when compared with room temperature, giving recoveries of 53% and 66% for POROS HS 50 (Fig. 4.15b) and POROS HS 20 (Fig. 4.15d), respectively.

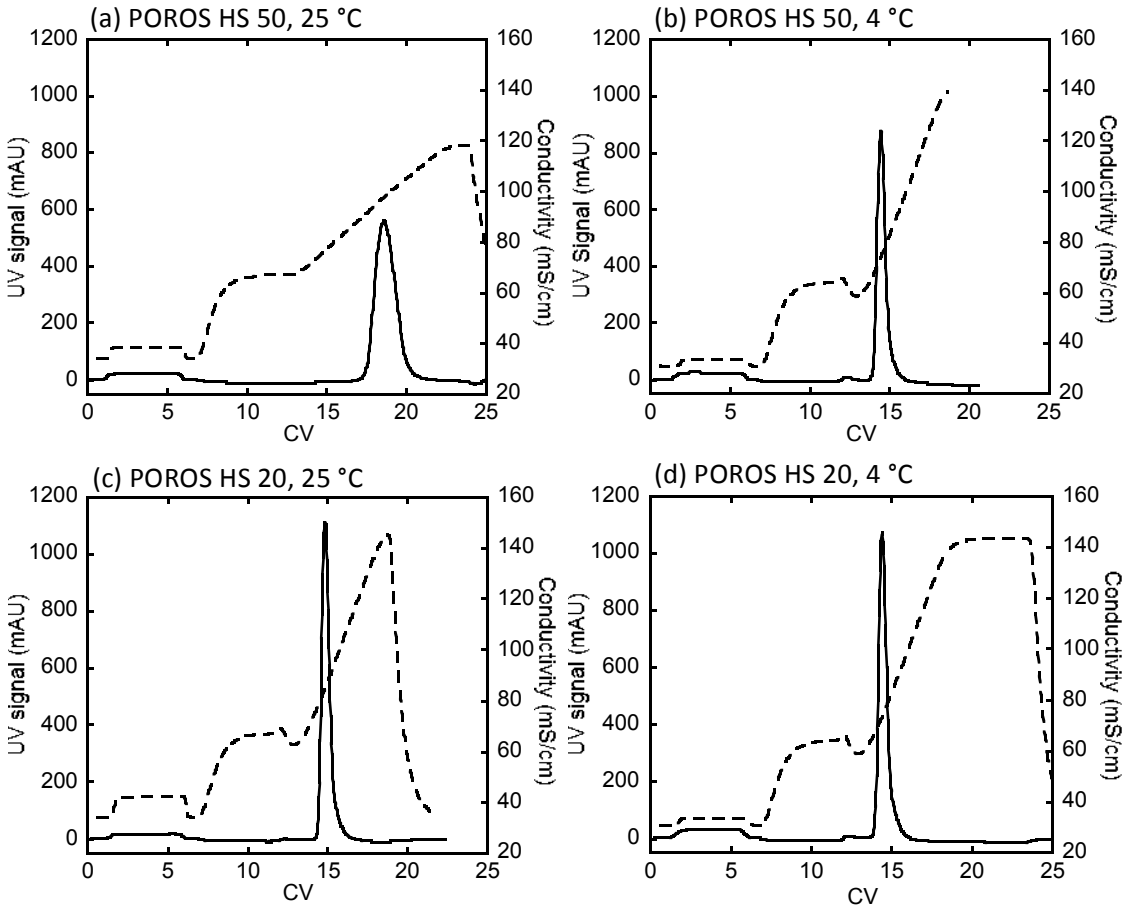

Figure 4.14. Representative load-wash-elute curves for VLP on POROS HS 50 (top row) and POROS HS 20 (bottom row) columns at 25 °C (a, c) and at 4 °C (b, d). 5 mL of 0.23 mg/mL VLPs sample was injected at 0.5 mL/min for each run. The gradient is from 0 - 1000 mM NaCl in 10 CV gradient in Fig 4.12a and 0 - 1500 mM NaCl in 7 CV in Fig. 4.12b, c and d.

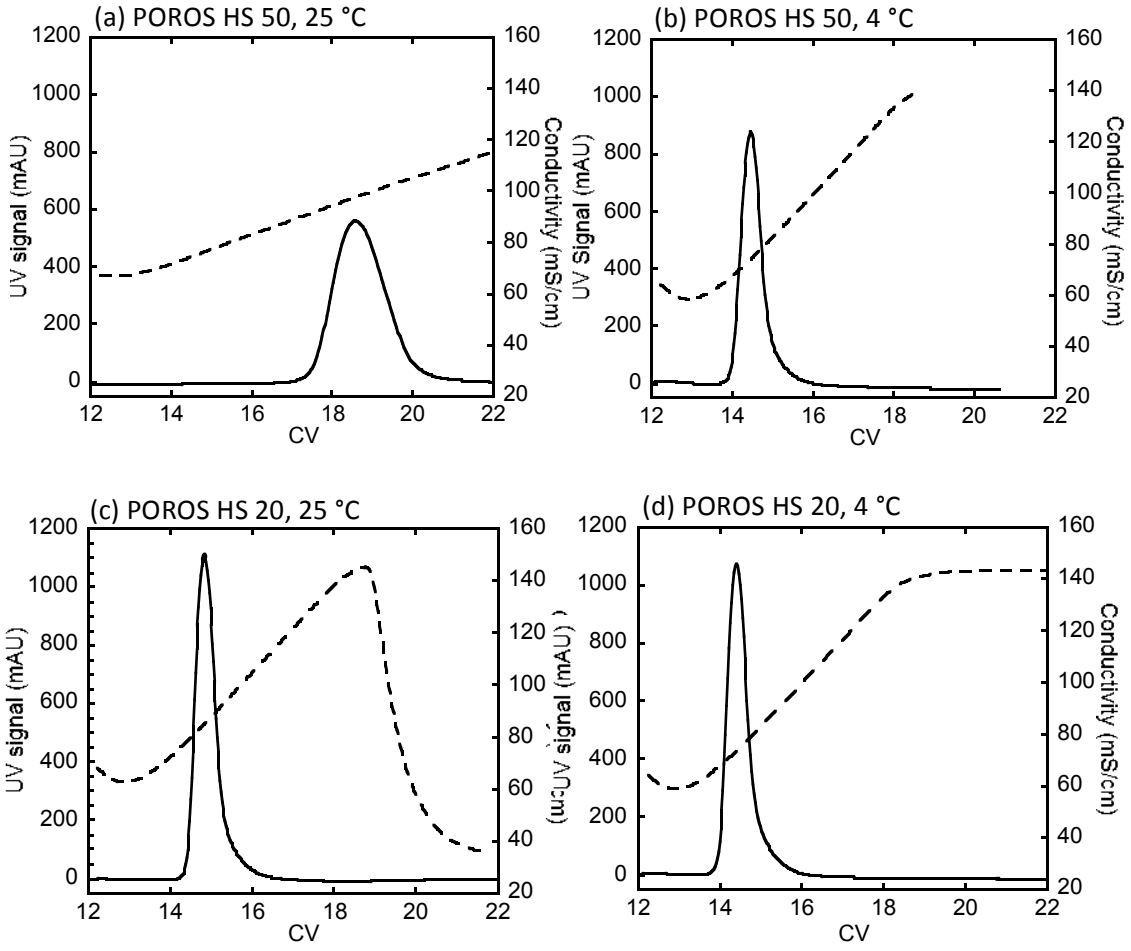

Figure 4.15. The elution step of the corresponding load-wash-elute curves in Fig. 4.12.

Figure 4.16 shows the load-wash-elute curves of VLP on the SO3-1 monolith column at 25 °C using different flow direction settings, which are described in in Table 4.2. In the initial experiment, the monolith was operated in the normal forward flow direction (from the outer side to the inner side), as recommended by the monolith manufacturer, for both load, wash, and elution steps. As seen in Fig. 4.16a, no distinct elution peak could be seen corresponding to practically no recovery. Since the dense "skin" layer structure seen in SEM images (Fig. 4.2) may have effects on VLP recovery, further experiments were done reversing the flow direction as indicated in Table 4.2. For forward flow load and reversed flow elution (Fig. 4.16b), there is again no elution peak and most of the VLPs loaded emerges as soon as elution begins indicating that all of the VLP binding occurred at the inlet end of the monolith. Using reverse flow load and forward flow elution (Fig. 4.16c) improved elution and recovery. Although a fraction of the VLP eluted right away when the flow direction is reversed, a significant portion of the VLP loaded (~26%) elutes in the gradient. Finally, using reversed flow for both load and elution (Fig. 4.16d) gave the best results with about 30% of the VLP eluting in the gradient. These results suggesting there are possibly two factors affecting the recovery of VLPs from monoliths matrix: (1) the physical trapping of VLPs in dead-end or constricted channels inside the monoliths matrix, and (2) a strong interaction between VLPs and the outer surface of the "skin" layer. The SEM images of the internal structure of the monoliths matrix show that the skeleton of the matrix is composed of polymer agglomerates with a rough surface and with a wide distribution of channel sizes. Isocratic elution experiments of glucose and salt discussed in Section 4.3.1, together with the shape of the breakthrough curves of LYO and IgG in Section 4.3.2 also suggest the existence of

small pores inside the matrix. On the other hand, the chemical properties of the 'skin' layer on the outer surface of the monoliths side wall are unknown. It is possible that the interaction between VLPs and this "skin" layer structure are too strong for the effective desorption of VLPs.

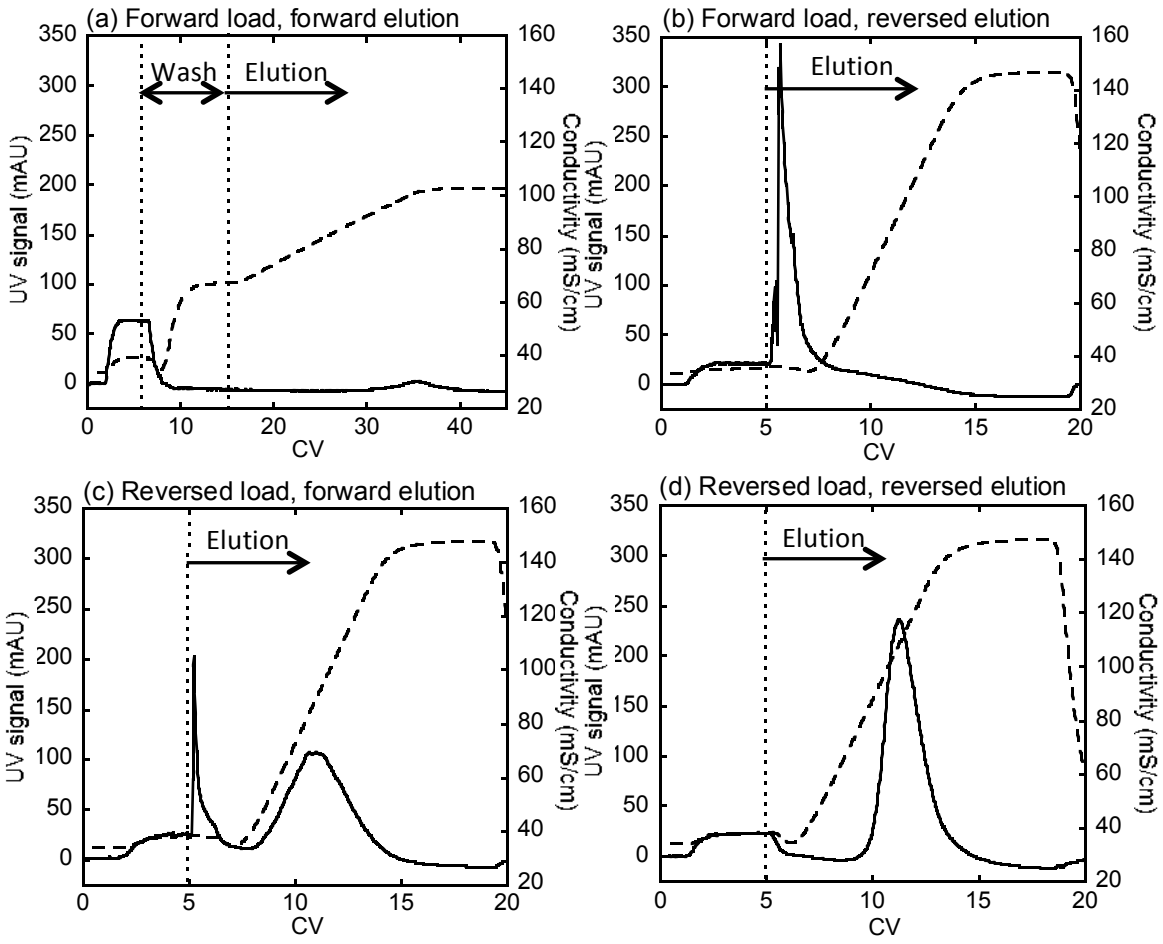

Figure 4.16. Representative load-wash-elute curves for VLP on monolith column at room temperature operated as follows: (a) forward load and forward elution, (b) forward load and reversed elution, (c) reversed load and forward elution and (d) reversed load and reversed elution. Elution gradient in Fig. 4.14a is 0 – 1 M NaCl in 20 CV and in Fig. 4.14b, c and d are 0 – 1.5 M NaCl in 20 CV. A wash step of 10 CV after load step was only used in Fig. 4.14a.

Figure 4.17 compared the chromatograms obtained for the load-wash-elute sequence for VLPs on the monolith column at 4 °C using reverse flow direction for the entire process, together with the chromatograms of both POROS columns at 4 °C. At this temperature, VLP recoveries were comparable for all three columns (56, 53 and 66% for monolith, POROS HS 50 and POROS HS 20, respectively). However, the VLP elution peak for the monolith column is much broader than that obtained with the POROS columns, which may be due to blocking of through-pores by the bound VLPs causing uneven flow distribution.

The eluted VLPs from POROS HS columns and monoliths column were collected and the hydrodynamic radius r_s of the eluted VLPs was measured by DLS. A summary of VLPs recovery and hydrodynamic radius obtained by DLS is provided in Table 4.3. The DLS results show that there is no significant size change for the eluted VLPs, except for the case of Fig. 4.16b (forward flow for load and reversed flow for elution), where the r_s of VLPs increased from 55 ± 5 nm to 72 ± 1.2 nm. This is possibly a result of aggregation caused by accumulation of VLPs on the skin layer on the inlet (outer) side of the monolith.

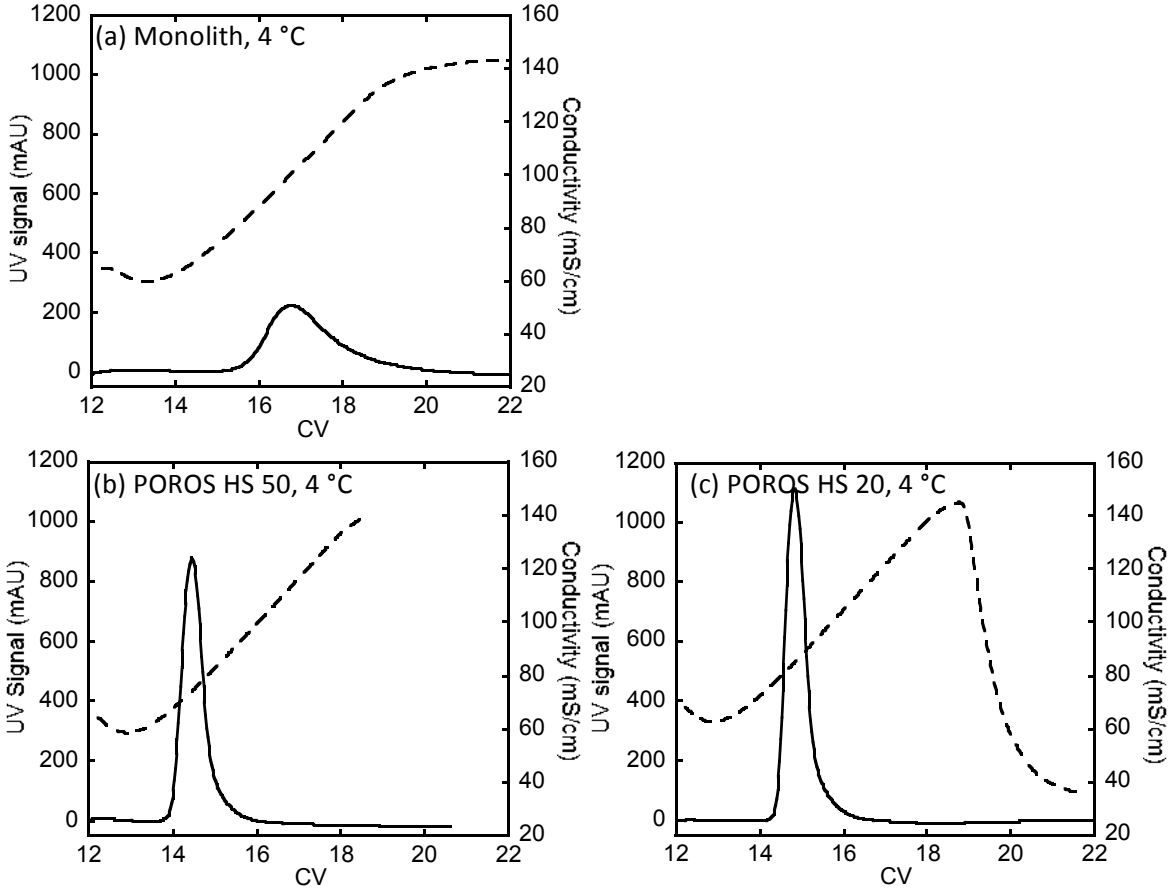

Figure 4.17. Representative load-wash-elute curves of VLP on monolith column with reversed flow direction in the entire process (a), POROS HS 50 column (b) and POROS HS 20 column (c) at 4 °C.

Table 4.3. Summary of VLP recovery and hydrodynamic radii of eluted VLPs.

	Flow Direction[(a)]	Room Temperature (25 °C)		4 °C	
		Recovery (%)	Hydrodynamic radius, r_s (nm)	Recovery (%)	Hydrodynamic radius, r_s (nm)
POROS HS 50	N/A	44	60 ± 0.7	53	58 ± 0.6
POROS HS 20	N/A	45	54 ± 0.5	66	55 ± 0.5
Monoliths	+ loading + elution	<3	N/A	N/A	N/A
	+ loading - elution	N/A	72 ± 1.2[(b)]	N/A	N/A
	- loading + elution	26	57 ± 1.0	N/A	N/A
	- loading - elution	30	56 ± 1.5	56	57 ± 1.3

[(a)] +: forward; –: reversed

[(b)] sample was collected during the wash step

To further compare the adsorption and recovery of proteins and VLPs on monolith and POROS HS columns, the pressure changes in the monolith column during the load step using different flow direction settings are shown in Fig. 4.18, for VLPs (Fig. 4.18a), Lyo (Fig 4.18b) and IgG (Fig. 4.18c). The starting pressures of VLP runs are lower due to the lower load flow rate (0.2 mL/min) compared with protein runs (4 mL/min). However, a dramatic increase of pressure appears for both runs using forward flow load while the runs using reversed flow load show relatively small pressure changes. For protein runs, the forward flow load runs show slightly higher pressure change compared to reversed flow load runs. These results indicating the hindrance effect of the skin layer on the outer surface of the monolith is more obvious on the transport of VLPs than that of proteins, which is likely due to the much larger size of VLPs.

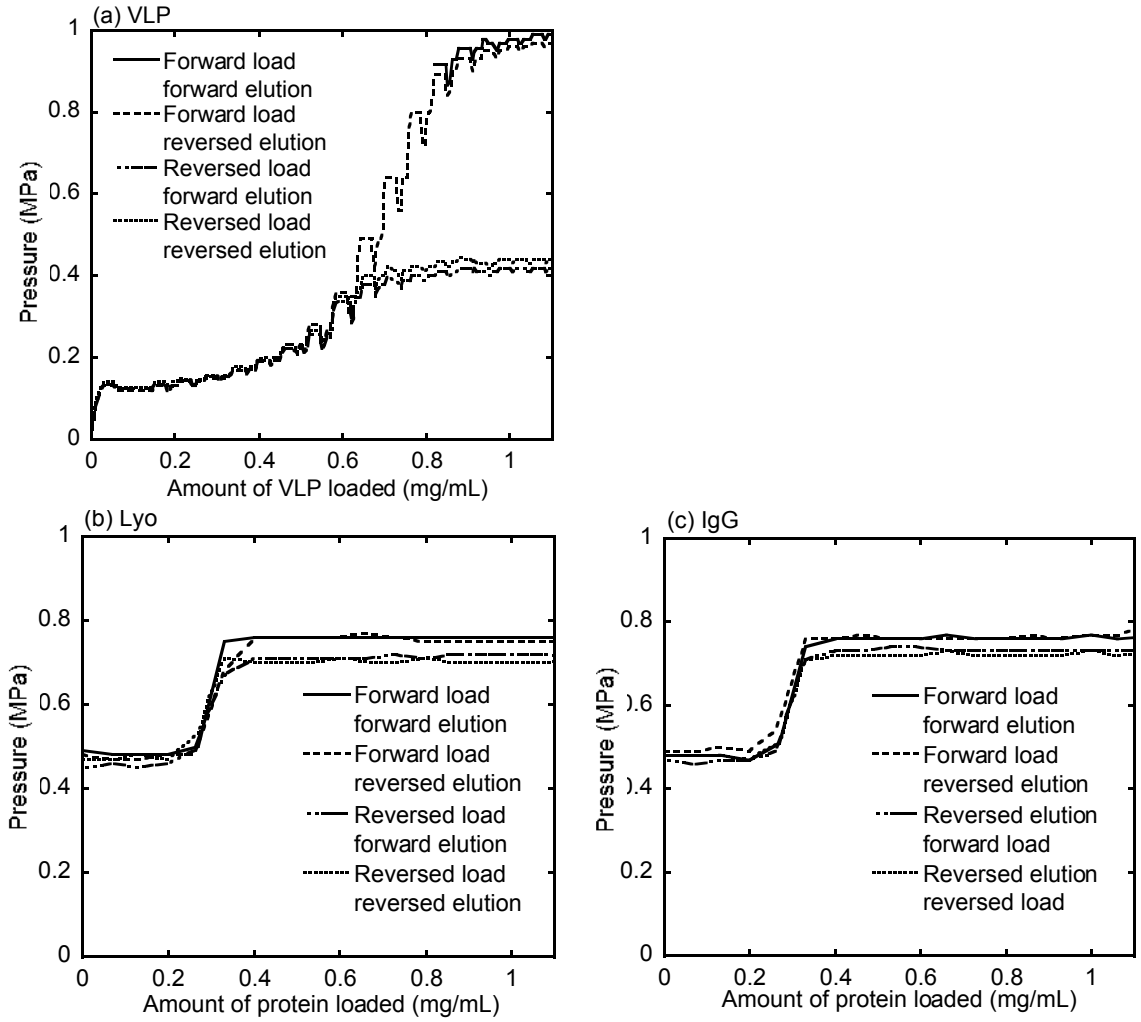

Figure 4.18. Pressure changes in the monolith column during the load step of VLPs (a), Lyo (b) and IgG (c) using different flow direction settings. The load flow rate for VLPs runs is 0.2 mg/mL and for proteins are 4 mL/min.

The elution peaks of Lyo and IgG on monolith column using forward flow load and forward load elution, and reversed flow load and reversed flow elution, are compared with the elution peaks on POROS HS 50 and POROS HS 20 in Figs. 4.19 and 4.20. For both proteins, the elution peaks on the monolith column are slightly broader than on POROS HS columns, especially when compared with POROS HS 20. These results are quantitatively consistent with that for VLPs, which is probably due to the uneven flow distribution. However, as the smaller molecular size of proteins, the blocking of pores by the bound proteins is much less significant than that caused by bound VLPs, the broadening effects on elution peaks on the monolith column is less obvious for proteins.

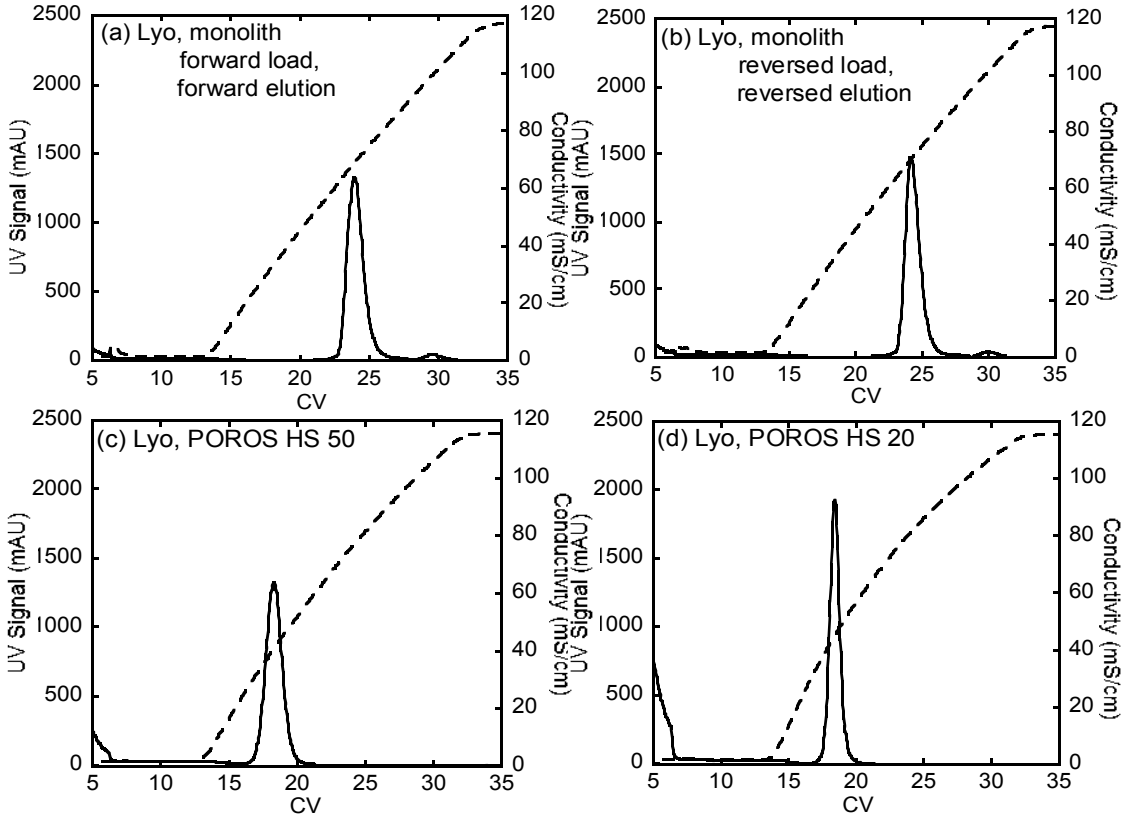

Figure 4.19. Lyo elution peaks on monolith column using forward flow load and forward load elution (a), and reversed flow load and reversed flow elution (b), compared with the elution peaks on POROS HS 50 (c) and POROS HS 20 (d).

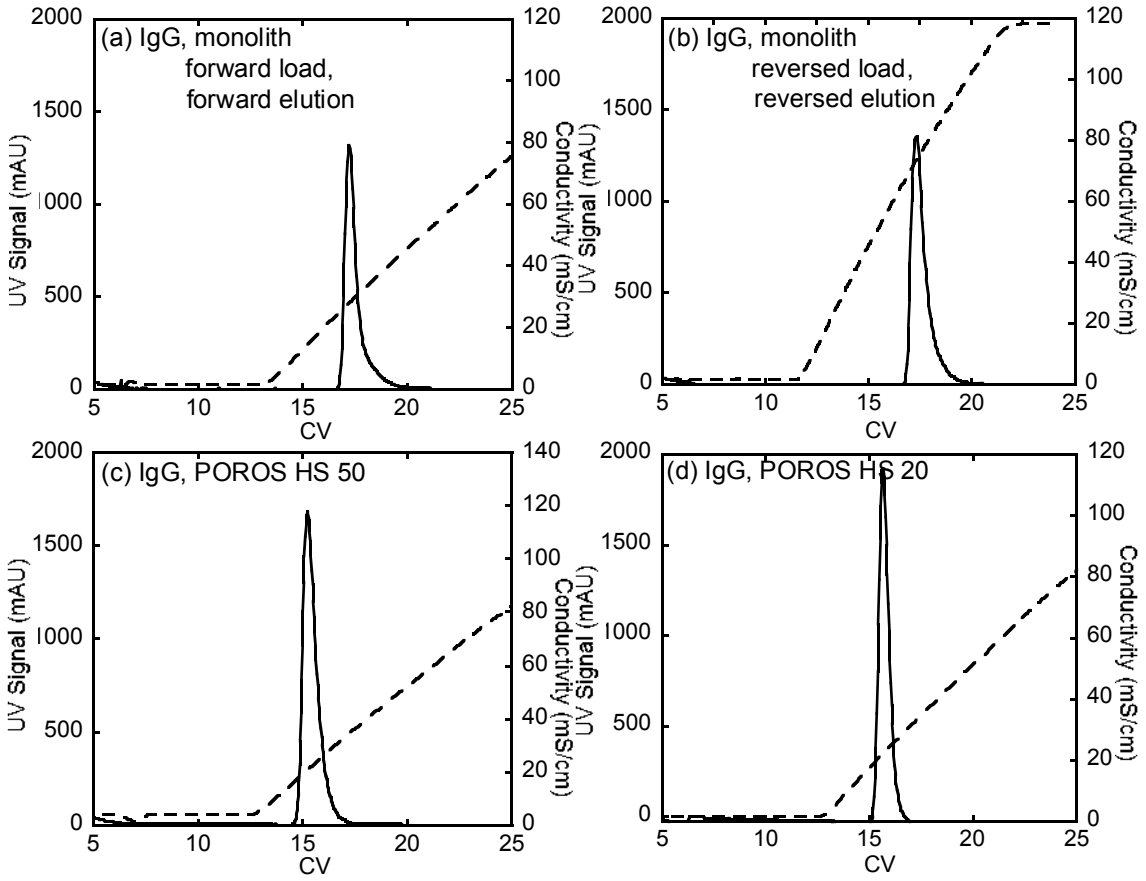

Figure 4.20. IgG elution peaks on monolith column using forward flow load and forward load elution (a), and reversed flow load and reversed flow elution (b), compared with the elution peaks on POROS HS 50 (c) and POROS HS 20 (d).

4.4 Conclusion

This work studied the adsorption and recovery properties of proteins and VLPs on a CIM SO3-1 tube monoliths column. The physical structures of the monoliths matrices and the monoliths column were first determined. SEM and TEM images of both CIM SO3-1 and QA-1 columns showed a wide size distribution of flow channels inside the monoliths matrix and the monoliths skeleton is composed of polymer agglomerates. Large flow channels with sizes of 1000-2000 μm or even higher are visible from the microscopy images, which are potentially more preferable for accommodating VLPs comparing with the macropores in POROS HS particles of about 500 nm. The side wall of the monoliths matrix, from which the mobile phase flow into the monoliths, is covered by a dense skin layer with few open pore structure. Pressure drop at different flow rate showed monoliths column has very similar pressure drop across the column with POROS HS 50 column with the same column volume, however, the permeability of monoliths column is two orders of magnitude smaller than that of POROS HS 50 column. An equivalent particle diameter of 1.2 μm and an estimated channel diameter of 0.74 μm were obtained from the permeability of monoliths column.

Inverse sized exclusion chromatography was carried out using dextran probes with different hydrodynamic radius to obtain the accessible void volume inside the monoliths matrix. A large dead volume (0.70 mL) inside the housing, larger than the actual monoliths volume (0.63 mL) was obtained based on the retention of glucose. This result is consistent with the observation of the broad, tailing elution peaks of dextran probes, which is significantly resulted from hydrodynamic dispersion. The retention volumes of dextran probes with different molecular sizes are essentially similar with each other,

indicating most of the flow channels inside the monoliths are large enough to prevent significant size exclusion effects.

Isocratic pulse response experiments of proteins and VLPs were used to study the effects of flow to the mass transfer inside the monoliths matrix under non-binding conditions. For each protein and VLP, the elution peaks under different flow rates came out at the same elution volume, suggesting the mass transfer is independent of flow rate. The smallest protein, Lyo, and salt showed later elution comparing with other proteins and VLPs, indicating the existence of very small pores that can only be accessed by small adsorbates. The first moments of dextran, proteins and NaCl under non-binding conditions show a rapid decrease at lower molecular size range of the probes followed by a slowly decline at $r_s > 10$ nm range, which is similar to the bimodal pores size distribution in POROS HS particles.

The adsorption of Lyo and IgG on monoliths column were studied by frontal analysis. The profile of the breakthrough curves of IgG showed strong independence of flow rate, indicating the absence of mass transfer resistance on proteins in monoliths column. For Lyo, a slightly dependence on flow rate can be observed, indicating the existence of mass transfer resistance in the smaller pores. By comparing the breakthrough curve for these two proteins on monoliths column, it can be noticed that despite its smaller molecular size, Lyo has shallower breakthrough curve shape than IgG, which again suggesting the existence of smaller pores that are only accessible by smaller molecules like Lyo. POROS HS columns, on the other hand, showed shallower breakthrough curves for both proteins at higher flow rate. However, both EBC and DBC of Lyo and IgG of monoliths column are relatively low compare to POROS HS columns.

The effective diffusivity of IgG in POROS HS columns were analyzed based on the $DBC_{10\%}$/EBC under different residence time. The enhancement effect of perfusion on IgG transport in frontal analysis is consistent with that obtained from CLSM experiments under flow conditions, and slightly smaller than the results of HETP measurements under non-binding conditions, which is likely caused by the hindrance of bound proteins inside the pores.

The recovery of VLP on monolith is very low and dependent on the direction of flow in the monolith suggesting that physical trapping of the VLPs inside the monoliths or strong interaction between the surface "skin" layer occurred. By comparing the recovery of VLPs from the monoliths column under different flow directions and operating temperatures, the reversed flow for the entire process at 4 °C yields the highest recovery of 56%. The effects of flow direction on protein adsorption and recovery shows the "skin" layer have less effects to the transport of proteins with much smaller size compared with VLPs.

4.5 List of Symbol

ε	monolith porosity
η	mobile phase viscosity (Pa·s)
B_0	hydraulic permeability, m^2
D_o	outer diameter of monoliths (m)
D_i	inner diameter of monoliths (m)
d_{bed}	thickness of monoliths (m)

d_{ch} apparent diameter of flow channels in monoliths (m)

d_{eq} equivalent particle diameter of monoliths (m)

L column length (cm)

ΔP Column pressure drop, Pa

Q flow rate (mL/min)

u superficial velocity (cm/s)

u_{ave} average superficial velocity (cm/s)

4.6 References

[1] Jungbauer, A., Hahn, R. (2008). Polymethacrylate monoliths for preparative and industrial separation of biomolecular assemblies. *J. Chromatogr. A, 1184*(1-2), 62-79.

[2] Wajcman, H., Ducrocq, R., Rious, J., Mathis, M., Godart, C., Prehu, C., Galacteros, F. (1996). Perfusion chromatography on reversed-phase column allows fast analysis of human globin chains. *Anal. Biochem., 237*(1), 80-87.

[3] McCarthy, E., Vella, G., Mhatre, R., Lim, Y.P. (1996). Rapid purification and monitoring of immunoglobulin M from ascites by perfusion ion-exchange chromatography. *J. Chromatogr. A, 743*(1), 163-170.

[4] Fahrner, R.L., Whitney, D.H., Vanderlaan, M., Blank, G.S. (1999). Performance comparison of Protein A affinity-chromatography sorbents for purifying recombinant monoclonal antibodies. *Biotechnol. Appl. Biochem., 30* (2), 121-128.

[5] Savary, B.J. (2001). Perfusion chromatography separation of the tomato fruit-specific pectin methylesterase from a semipurified commercial enzyme preparation. *Prep. Biochem. Biotechnol., 31* (3), 241-258.

[6] Losso, J.N., Bansode, R.R., Bawadi, H.A. (2003). Perfusion Chromatography Purification of a 15 kDa Rice Prolamin. *J. Agric. Food Chem., 51*(24), 7122-7126.

[7] Heras, J.M., Marina, M.L., García, M.C. (2007). Development of a perfusion ion-exchange chromatography method for the separation of soybean proteins and its application to cultivar characterization. *J. Chromatogr. A, 1153*(1-2), 97-103.

[8] Limonta, M., Márquez, G., Rey, I.a, Pupo, M., Ruiz, O., Amador-Cañizares, Y., Dueñas-Carrera, S. (2008). Plasmid DNA recovery using size-exclusion and perfusion chromatography. *Biopharm. Int., 21*(9), 38-48.

[9] Cook, J. C., Joyce, J. G., George, H. a, Schultz, L. D., Hurni, W. M., Jansen, K. U., Hepler, R. W., et al. (1999). Purification of virus-like particles of recombinant human papillomavirus type 11 major capsid protein L1 from Saccharomyces cerevisiae. *Protein Express. Purif.*, *17*(3), 477-84.

[10] Urthaler, J., Schlegl, R., Podgornik, A., Strancar, A., Jungbauer, A., Necina, R. (2005). Application of monoliths for plasmid DNA purificationDevelopment and transfer to production. *J. Chromatogr. A, 1065*(1), 93-106.

[11] Tennikova, T.B., Bleha, M., Švec, F., Almazova, T.V., Belenkii, B.G. (1991). High-performance membrane chromatography of proteins, a novel method of protein separation. *J. Chromatogr. A, 555*(1-2), 97-107.

[12] Nakanishi, K., Soga, N. (1991). Phase Separation in Gelling Silica–Organic Polymer Solution: Systems Containing Poly(sodium styrenesulfonate). *J. Am. Ceram. Soc., 74*(10), 2518–2530.

[13] Švec, F., Tennikova, T.B., Deyl, Z. (2003) Monolithic Materials: Preparation, Properties, and Applications. Elsevier, Amsterdam.

[14] Minakuchi, H., Nakanishi, K., Soga, N., Ishizuka, N., Tanaka, N. (1996). Octadecylsilylated porous silica rods as separation media for reversed phase liquid chromatography. *Anal. Chem., 68*, 3498-3501.

[15] Trilisky, E.I., Koku, H., Czymmek, K.J., Lenhoff, A.M. (2009). Relation of structure to performance characteristics of monolithic and perfusive stationary phases. *J. Chromatogr. A, 1216*(36), 6365-6376.

[16] Brne, P., Podgornik, A., Benčina, K., Gabor, B., Štrancar, A., Peterka, M. (2007). Fast and efficient separation of immunoglobulin M from immunoglobulin G using short monolithic columns. *J. Chromatogr. A, 1144*(1), 120-125.

[17] Benčina, M., Podgornik, A., Štrancar, A. (2004). Characterization of methacrylate monoliths for purification of DNA molecules. *J. Sep. Sci., 27*(10-11), 801-810.

[18] Zoechling, A., Hahn, R., Ahrer, K., Urthaler, J., Jungbauer, A. (2004). Mass transfer characteristics of plasmids in monoliths. *J. Sep. Sci., 27*(10-11), p. 819-827.

[19] Kramberger, P., Peterka, M., Boben, J., Ravnikar, M., Štrancar, A. (2007). Short monolithic columns-A breakthrough in purification and fast quantification of tomato mosaic virus. *J. Chromatogr. A, 1144*(1), 143-149.

[20] Williams, S.L., Eccleston, M.E., Slater, N.K.H. (2005). Affinity capture of a biotinylated retrovirus on macroporous monolithic adsorbents: Towards a rapid single-step purification process. *Biotechnol. Bioeng., 89*(7), 783-787.

[21] Wang, P.G. (2010) Monolithic Chromatography and Its Modern Applications. ILM Publications, Hertfordshire, UK.

[22] Hahn, R., Tscheliessnig, A., Bauerhansl, P., Jungbauer, A. (2007). Dispersion effects in preparative polymethacrylate monoliths operated in radial-flow columns. *J. Biochem. Biophys. Methods, 70*, 87-94.

[23] Leinweber, F.C., Tallarek, U. (2003). Chromatographic performance of monolithic and particulate stationary phases. Hydrodynamics and adsorption capacity. *J Chromatogr A., 1006*(1-2), 207-228.

[24] Rupar, M., Ravnikar, M., Tusek-Znidaric, M., Kramberger, P., Glais, L., Gutierrez-Aguirre, I. (2013). Fast purification of the filamentous Potato virus Y using monolithic chromatographic supports. *J. Chromatogr. A, 1272*, 33-40.

[25] CIM Convective Interaction Media®-Liquid Chromatography Redesigned. Rapid Chromatography for Large Biomolecules. BIA Separations.

[26] Tao, Y., Perez-Almodovar, E., Carta, G. (2011). Adsorption kinetics of deamidated antibody variants on macroporous and dextran-gradted cation exchangers. III. Microscopic studies. *J. Chromatogr. A, 1218*(44), 8027-8035.

[27] Shi, L., Sanyal, G., Ni, A., Luo, Z., Doshna, S., Wang, B., Graham, T.L., Wang, N., Volkin, D.B. (2005). Stabilization of human papillomavirus virus-like particles by non-ionic surfactants. *J. Pharm. Sci., 94*, 1538-1551.

[28] Carta, G., Jungbauer, A. (2010) Protein Chromatography: Process Development and Scale-Up, Wiley-VCH, Weinheim, Germany.

[29] CIM Tube monolithic column 1 mL instruction manual

[30] Guiochon, G., Felinger, A., Katti, A.M., Shirazi, D. (2006) Fundamentals of Preparative and Nonlinear Chromatography, Elsevier, Amsterdam, The Netherlands.

[31] Mihelic, I., Nemec, D., Podgornik, A., Koloini, T. (2005). Pressure drop in CIM disk monolithic columns. *J Chromatogr A., 1065*(1), 59-67.

[32] Tallarek, U., Leinweber, F.C., Seidel-Morgenstern, A. (2002). Fluid dynamics in monolithic adsorbents: phenomenological approach to equivalent particle dimensions. *Chem. Eng. Technol. 25*(12), 1177-1181.

[33] Jackson, G.W., James, D.F. (1977). The permeability of fibrous porous media. *Can. J. Chem. Eng., 64*(3), 364-347.

[34] Teo, W.K., Ruthven, D.M. (1986). Adsorption of water from aqueousehtanol using 3-Å molecular sieves. *Ind. Eng. Chem. Process Des. Dev. 25* (1), 17-21.

[35] Weber, T.W., Chakravorti, R.K. (1974). Pore and solid diffusion models for fixed bed adsorbers. AIChE J., 20(2), 228–238.

[36] Kataoka, T., Yoshida, H., Ueyama, K. (1972). Mass Transfer in Laminar Region Between Liquid and Packing Material Surface in The Packed Bed. *J. Chem. Eng. Japan, 5*(2), 132-136.

[37] Carta, G., Ubiera, A.R., Pabst, T.M. (2005) Protein Mass Transfer Kinetics in Ion Exchange Media: Measurements and Interpretations. *Chem. Eng. Technol., 28*(11), 1252-1264.

Chapter 5
Conclusions and Recommendations

5.1 Conclusions

This work has elucidated important characteristic of two different perfusion stationary phases, POROS HS, a perfusion porous particle, and the CIM SO3-1 monoliths column, as well as the mechanism and rate at which proteins and HPV VLPs are adsorbed by the stationary phases were studied. POROS HS 50 particles has a bimodal distribution of pores including large open pores transecting a network of smaller pores present within microparticle aggregates around 500 nm in size. The effects of perfusion on the mass transfer of model proteins and VLPs under both non-binding and strong binding conditions were demonstrated by HETP measurements and CLSM experiments, respectively. For non-conditions, the effects of perfusion is negligible for small proteins (e.g. Lyo), and only slight for larger proteins such as IgG even at 1000 cm/h flow velocity. However, for very large proteins (e.g. Tg) and VLPs, the effects of perfusion become substantial or even dominant. CLSM images of protein adsorption under flow conditions also show for large protein like Tg, intraparticle concentration profiles asymmetrically skew in the direction of flow, deviating from the symmetrical profile of classical shrinking core model obtained for smaller protein like IgG, which confirm the effects of perfusion. In the case of VLPs and fluorescently labeled latex nanoparticles of similar size with VLPs, however, the effects of perfusion seem to vanish since the binding only occurs exclusively in a thin layer at the particle surface, indicating that the bound VLPs

block access to most through-pores preventing both diffusion and convection. The effects of particle size to the mass transfer behavior of proteins and VLPs were then studied using POROS HS 20, a smaller particle of about half size of POROS HS 50, but similar internal structures. With smaller particle size, POROS HS 20 provide a intraparticle flow ratio *F*, about 3 time of that for POROS HS 50, indicating the effects of perfusion becomes substantial at lower reduced velocity.

Structural properties of CIM tube monoliths column were studied. Large flow channels of 1000-2000 μm were observed in SEM images, as well as small pores distributed between polymer skeleton agglomerates. The monoliths column has similar pressure drop with POROS HS 50 column with the same column volume, however, 2 orders of magnitude smaller column permeability. The mass transfer of proteins and VLPs are essentially independent of flow rate, while the severely tailed peaks may due to the large dead volume inside the column housing. The larger retention volumes of small molecules (eg. Lyo and salt), indicate the existence of very small pores inside the monoliths. Despite the absence of mass transfer resistance in monoliths column, both EBC and DBC are not favorable for proteins when compare to POROS HS columns, due to the small binding surface area. Low recovery of VLPs were obtained for monoliths column, comparing with POROS HS columns, which is probably caused by the dense skin layer on the side wall of the monoliths, which is observed in SEM images. Thus, flow directions in loading and elution process have great effects on the recovery of VLPs on monoliths column, while operating temperature also contributes to the results.

Overall, this work provides as insight of the performance of perfusion chromatography stationary phases on the separation of proteins and VLPs. For example,

HETP measurements under non-binding conditions, together with the internal structure of the resin particles, can be used to predict the enhancement on mass transfer provided by perfusion, using eq. 1.3 and 1.4. The results of VLPs adsorption in Chapter 2 explained the significant lot-to-lot variation of separation performance of POROS HS 50, that even the size of the through-pores inside the particles are not large enough to allow VLPs transport throughout the entire particle as previously postulated. As a result, the particle size has great effects to the separation performance as only the surface of the particles can be utilized by VLPs. The study on POROS HS 20 in Chapter 3 further demonstrated the correlation of perfusion effects with resin particles size and internal structure, providing a relationship between perfusion theories and experimental data. The extension to monoliths study in Chapter 4 evaluated the advantages and disadvantages of monoliths in separation of proteins and VLPs comparing with perfusion particles packed bed. These results provide the necessary tools and knowledge for both the effective design and further development of new perfusion chromatographic materials for different bio-products.

5.2 Recommendations for Future Work

With the evidences provided in this work on VLPs adsorption behaviors on perfusion chromatography particles and monoliths, the following recommendations can be made for future work.

Since the adsorption of VLPs on POROS HS particles is restricted to a thin layer on the surface of the particle, the particle size distribution and surface roughness of the particles have great effects to the adsorption of VLPs. As a result, these two parameters

become critical for the assuring the lot-to-lot consistency of POROS HS resin or other similar chromatography media to achieve VLPs separation.

The ratio of pore size and particles size can be used as a critical parameter in design and selection of perfusion media for the separation of proteins and larger bio-molecules like VLPs. Chapter 2 showed that the size of the macropores in POROS HS resin is not large enough to accommodate VLPs under binding conditions; therefore the potential high binding capacity inside the resin particles is not usable. Designing proper perfusion media with larger pore size can increase the penetration of VLPs into the resin particles and, hence, achieve higher binding capacities. On the other hand, Chapter 3 showed the effects of particle size on perfusion inside the resin particles when the internal pore structures are kept relatively consistent. Smaller particles with larger macropore size will be more beneficial for the adsorption of large biomolecules like VLPs, however, this structure may decrease the mechanical strength of the particles.

The interaction between VLPs and the resin particle backbone can be further modified by controlling the mobile phase composition. Although the penetration of bound VLPs into the particles are highly restricted, the desorption process was shown to be incomplete, meaning that a large fraction of bound VLPs couldn't be recovered from the particles. By modulating the interaction between VLPs and the resin particles, it may be possible to achieve higher recoveries. The use of additives, such as arginine, that reduce hydrogen bonding should be considered.

In the case of monolith columns, more information of the distribution of bound VLPs on monolith columns is needed. Chapter 4 showed that, although the flow channel size is much larger than the through-pore size in POROS HS particles, and much larger

than the size of the VLPs, it appears that a significant fraction of the loaded VLPs are trapped inside the monoliths. Meanwhile, the extent of VLP binding inside the monoliths matrix is still not clear. EBC and DBC of VLPs on monoliths column need to be determined and the specific binding location should be visualized by immunostaining the bound VLPs using HPV-antibody conjugated gold nanoparticles or fluorescent dyes. This study can also be helpful to understand the effects of the smaller pores to the physical trapping of VLPs inside monoliths and provide important knowledge for the improvement of the preparation process of polymer monoliths and the control of critical parameters.

VLP load-wash-elute experiments showed that the skin layer on the side surface of the monolith has great impact to the transport of VLPs into the monolith matrices, thus, further study on the nature of the skin layer is needed. The experimental data has shown that the recovery of VLPs is lower when loaded onto the skin layer; however, the reasons for the existence of this skin layer are not known. The chemistry of the skin layer and its interaction with VLPs needs also to be determined. Immunostaining of bound VLPs on the skin layer using HPV-antibody conjugated with gold nanoparticles or fluorescent dye can be carried out to determine the specific binding locations of VLPs on the skin layer.

Another approach to improve the adsorption and recovery of VLPs on monoliths is to select or design matrices with different structure. The CIM tube monolith columns studied in this work have a bimodal pore size distribution and the smaller pores inside the matrix may be responsible for the physical trapping of VLPs, which results in the low recovery. The typical manufacturing of polymer monoliths employs radically initiated cross-linking polymerization processes, during which the polymerization step occurs in a homogeneous liquid polymerization precursor mixture containing monomers and a

porogenic solvent. The choice of monomer mixture composition, porogenic solvent composition and the temperature during polymerization are critical experimental parameters that have great effects to the flow channel size and pore volume. Therefore, a monoliths matrix containing only large flow channels and no small pores is desirable for the separation of large biomolecules like VLPs.

Besides the optimization of the stationary phase and operating conditions, the large molecular radius of VLPs is the most significant obstacle in the downstream purification processes. As a result, further study should be carried out on the adsorption and recovery behavior of HPV L1 protein monomers and HPV capsids, both of which are much smaller in size than VLPs. L1 protein monomers and capsids can be obtained from disassembled VLPs. After purification, the L1 protein monomers and capsids can be reassembled to form VLPs with uniform particle size.

Last but not least, it is necessary to develop a cost model to enable a proper economic comparison between POROS particles and monolith columns. The scaling-up of monoliths to the column volumes needed at the manufacturing scale without producing high pressure drops is needed. Furthermore, the reusability of the column is also important and should be assessed. Previous studies showed that residual VLPs can be removed efficiently from both POROS and monolith columns by cleaning-in-place with 0.5 M NaOH; however, more experimental data is needed at higher number of cycles and with more practical VLP loads.